LARGE RADIAL VELOCITY SEARCHES AND CHEMICAL ABUNDANCE STUDIES OF EXOPLANET-HOSTING STARS

By

Claude E. Mack III

Dissertation

Submitted to the Faculty of the

Graduate School of Vanderbilt University

in partial fulfillment of the requirements

for the degree of

DOCTOR OF PHILOSOPHY

in

Physics

May, 2015
Nashville, Tennessee

Approved:

Dr. Keivan G. Stassun, Ph.D.

Dr. Simon C. Schuler, Ph.D.

Dr. Kelly Holley-Bockelmann, Ph.D.

Dr. Andreas Berlind, Ph.D.

Dr. David A. Weintraub, Ph.D.

Dr. David Ernst, Ph.D.

To my parents,

Stella and Claude,

and

to their parents,

Narcelia and James, Edith and Claude,

for the heritage of education and a thirst for knowledge that they have passed down to me.

TABLE OF CONTENTS

Page

LIST OF TABLES vi

LIST OF FIGURES vii

Chapter

I. Introduction 1

II. How an SB2 can appear to be a star+BD system 4

- 2.1. Abstract 4
- 2.2. Introduction 5
- 2.3. Observations and Data Processing 10
  - 2.3.1. SDSS-III MARVELS Discovery RV Data 10
  - 2.3.2. APO-3.5m/ARCES RV Data 12
  - 2.3.3. HET/HRS RV Data 16
    - 2.3.3.1. CCF Mask 16
    - 2.3.3.2. TODCOR 18
  - 2.3.4. FastCam Lucky Imaging 19
  - 2.3.5. Keck AO Imaging 20
- 2.4. Results 21
  - 2.4.1. Initial spurious solution: a BD companion to a solar-type star 21
  - 2.4.2. Final solution: A highly eccentric, double-lined spectroscopic binary 27
    - 2.4.2.1. RV fitting 28
    - 2.4.2.2. Determining the stellar parameters for TYC 3010 . 30
  - 2.4.3. Inferred evolutionary status of TYC 3010 36
- 2.5. Discussion 37
  - 2.5.1. Why we initially derived a spurious solution 37
  - 2.5.2. How RV surveys can identify astrophysical false positives like TYC 3010 40
- 2.6. Summary 43

III. Detailed Abundances of Planet-Hosting Wide Binaries. I. HD 20782+HD 20781 51

- 3.1. Abstract 51
- 3.2. Introduction 52
- 3.3. Data and Analysis 56
- 3.4. Results 62
- 3.5. Discussion 64
  - 3.5.1. How well correlated are abundance and T_{C} expected to be? 64
  - 3.5.2. Interpretation of the positive slopes 69
  - 3.5.3. Comparison to previous work 73
- 3.6. Conclusion 75

IV. Detailed Abundances of Planet-Hosting Wide Binaries. II. HD 80606+HD 80607 77

- 4.1. Abstract 77
- 4.2. Introduction 78
- 4.3. Data and Analysis 80
- 4.4. Results 81
- 4.5. Discussion 82
  - 4.5.1. A model for the accretion of rocky planetary material by HD 80607 82
  - 4.5.2. Interpretation of the similar trends found in the abundances of HD 80606/07 85
- 4.6. Conclusion 86

V. Future Work 96

Appendix

A. Table II.1: complete and unabridged 99

B. Table III.2: complete and unabridged 102

C. Table IV.2: complete and unabridged 110

References 117

List of Tables

Table Page

II.1. Observed heliocentric single-lined radial velocities for TYC 3010 . . . 11

II.2. Observed heliocentric double-lined radial velocities for TYC 3010 . . . 11

II.3. Observed heliocentric radial velocities for HD102158 . . . 17

II.4. TYC 3010 orbital parameters: Spurious and True RV solutions . . . 25

II.5. Catalog Properties of TYC 3010-1494-1 . . . 26

II.6. TYC 3010 properties derived by this work . . . 31

III.1. HD 20782/81: Stellar Parameters & Abundances . . . 60

III.2. HD 20782/81: Lines Measured, Equivalent Widths, and Abundances . . . 61

IV.1. HD 80606/07: Stellar Parameters & Abundances . . . 88

IV.2. HD 80606/07: Lines Measured, Equivalent Widths, and Abundances . . . 89

IV.3. Giant Planet Orbital Characteristics & Host Star [X/H] vs T_{C} Slopes . . . 89

A.1. Observed heliocentric single-lined radial velocities for TYC 3010 . . . 100

B.1. HD 20782/81: Lines Measured, Equivalent Widths, and Abundances . . . 103

C.1. HD 80606/07: Lines Measured, Equivalent Widths, and Abundances . . . 111

List of Figures

Figure Page

2.1. The Spurious vs the True RV Curve for TYC 3010 6

2.2. Sample spectra of TYC 3010 14

2.3. Sample cross-correlation functions from spectra of TYC 3010 15

2.4. Sample lucky imaging frames for TYC 3010 22

2.5. Detectability curve for the lucky imaging and Keck AO images obtained for TYC 3010 24

2.6. SED fits for TYC 3010 45

2.7. The corrected RV curve for TYC 3010 46

2.8. An orbital schematic for the TYC 3010 binary star system 47

2.9. The derived mass and radius distributions for the TYC 3010 primary stellar component 48

2.10. H–R diagram for the TYC 3010 primary 49

2.11. Variations in the width of the peak in the cross-correlation function of TYC 3010 plotted with respect to time 50

3.1. Sample Magellan/MIKE spectra for HD 20782/81 57

3.2. Plots of Fe I abundance vs excitation potential and Fe I abundance vs reduced equivalent width 58

3.3. Differential abundances for HD 20782/81 as a function of atomic number (Z) 65

3.4. *Unweighted* linear fits to abundance vs. condensation temperature (T_{C}) for HD 20782/81. 66

3.5. *Weighted* linear fits to abundances vs. condensation temperature (T_{C}) for HD 20782/81. 70

3.6. *Unweighted* linear fits to simulated abundances vs. condensation temperature ($T_{\rm C}$) from our modeled accretion of X amount of $M_\oplus$ by a solar-composition star 71

4.1. Sample Keck/HIRES spectra for HD 80606/07 90

4.2. Differential abundances (HD 80607 − HD 80606) as a function of atomic number (Z) 91

4.3. *Unweighted* linear fits to abundance vs. condensation temperature ($T_{\rm C}$) for HD 80606/07. 92

4.4. *Weighted* linear fits to abundances vs. condensation temperature ($T_{\rm C}$) for HD 80606/07. 93

4.5. *Unweighted* linear fits to simulated abundances vs. condensation temperature ($T_{\rm C}$) from our modeled accretion of $5M_\oplus$ of material with Earth-like composition by a star like HD 80607. 94

4.6. *Unweighted* linear fits to simulated abundances vs. condensation temperature ($T_{\rm C}$) from our modeled accretion of $20M_\oplus$ of material with Earth-like composition by a star like HD 80607. 95

Chapter I

INTRODUCTION

In 1992, the first confirmed detection of planets that existed outside the Solar System (extrasolar planets or exoplanets) was announced (Wolszczan & Frail, 1992). Surprisingly, these planets were found orbiting a pulsar. This instantly raised a number of questions, such as can planetary systems survive the post main-sequence evolution of the host star, or is it somehow possible to have a second epoch of planet formation within the material that is ejected from the star during the giant phase of its evolution?

Three years later, in 1995, the world witnessed the first confirmed detection of an exoplanet around a solar-type star, 51 Peg (Mayor & Queloz, 1995). Once again, astronomers were in for a shock. The giant planet orbiting 51 Peg was only 0.05 AU from the star, and it only took 4 days to complete its orbit. Based on the standard model of planet formation at that time, one would never expect to find a gas giant planet orbiting so close to a star. For one, it could not form at that location because the temperature is so high that close to a star, all the gas would dissipate before the planet could fully form. On the other hand, if it migrated to that location, then it must have migrated at least 5–6 AU, which is considerably more migration than any planet in the Solar System was believed to have experienced. Within a few more years, scores of other close-in giant planets (so-called “hot Jupiters”) were found orbiting other stars. Nature could create very different types of stable planetary systems.

In order to better understand the frequency (or occurrence rate) of different kinds of planets, e.g., gaseous vs rocky, in the early 2000s there begin to be a great push to perform large-scale searches for exoplanets within a large, statistical sample of stars with well-known biases. Instead of the more piece-meal, "catch what you can" planet hunting that had occurred up to that point, these new large-scale surveys promised to provide robust statistics about which kinds of planets formed around particular types of stars. The MARVELS project, which was one of the four major components of phase three of the Sloan Digital Sky Survey (SDSS-III), was one example of a large-scale exoplanet survey. Its goal was to determine the frequency of Jupiter-mass planets on orbits of $\lesssim$1 year around FGK stars.

MARVELS was designed to achieve this goal by using a multi-object spectrograph to monitor the radial velocities (RVs) of around 10,000 stars over a total period of six years. The multi-object spectrograph would be able to simultaneously observe 60 stars. Each field of 60 stars would be observed 20-30 times over a two-year baseline.

The well-defined, statistical MARVELS sample would be particularly well-suited for certain kinds of ancillary projects, such as determining the frequency of planets in binary systems. In particular, determining the frequency of planets in *wide* binary systems could be especially useful, because wide binary systems consist of two stars that most likely formed from the same material at the same time, yet these two stars might possess planetary systems with starkly different architectures. Thus, planet-hosting wide binaries serve as a kind of laboratory where one can probe the connection between the chemical composition of the host star and the architecture of the planetary system in exquisite detail.

Unfortunately, the MARVELS spectrograph did not possess the precision to accomplish its worthy goal. However, it did detect a dozen or so brown dwarf candidate companions to solar-type stars. These brown dwarf candidates were orbiting their host stars much closer than brown dwarf companions typically do with solar-type stars. Chapter 2 of this dissertation discusses the unfortunate demise of one particular brown dwarf candidate from the MARVELS survey, as well as provides an important word of caution for large RV surveys that necessarily must use automated software to extract candidate substellar companions from their data.

Given that MARVELS did not find any exoplanets, it was not possible to use the MARVELS sample to study the relationship between host star composition and planetary system architecture. Instead, in Chapters 3 and 4, we discuss two special planet-hosting wide binaries already known to exist in the literature. These two special cases are the first in an ongoing study of the detailed chemical composition of planet-hosting wide binaries. In the final chapter, we discuss how the study of planet-hosting wide binaries will be continued in the near future, as well as briefly mention a few other interesting projects that involve the detailed chemical abundance analysis of exoplanet-hosting stars.

Chapter II

HOW A LONG PERIOD, VERY ECCENTRIC SPECTROSCOPIC STELLAR BINARY CAN MASQUERADE AS A BROWN DWARF COMPANION TO A SOLAR-TYPE STAR

This chapter is based on work published in the Astronomical Journal, 2014, Vol. 145, Article ID 139.

2.1 Abstract

We report the discovery of a highly eccentric, double-lined spectroscopic binary star system (TYC 3010-1494-1), comprising two solar-type stars that we had initially identified as a single star with a brown dwarf companion. At the moderate resolving power of the MARVELS spectrograph and the spectrographs used for subsequent radial-velocity (RV) measurements ($R \lesssim 30,000$), this particular stellar binary mimics a single-lined binary with an RV signal that would be induced by a brown dwarf companion ($M \sin i \sim 50\,M_{\rm Jup}$) to a solar-type primary. At least three properties of this system allow it to masquerade as a single star with a very low-mass companion: its large eccentricity ($e \sim 0.8$), its relatively long period ($P \sim 238$ days), and the approximately perpendicular orientation of the semi-major axis with respect to the line of sight ($\omega \sim 189°$). As a result of these properties, for ~95% of the orbit the two sets of stellar spectral lines are completely blended, and the RV measurements based on centroiding on the apparently single-lined spectrum is very well

fit by an orbit solution indicative of a brown dwarf companion on a more circular orbit ($e \sim 0.3$). Only during the ∼5% of the orbit near periastron passage does the true, double-lined nature and large RV amplitude of ∼15 km s^{-1} reveal itself. The discovery of this binary system is an important lesson for RV surveys searching for substellar companions; at a given resolution and observing cadence, a survey will be susceptible to these kinds of astrophysical false positives for a range of orbital parameters. Finally, for surveys like MARVELS that lack the resolution for a useful line bisector analysis, it is imperative to monitor the peak of the cross-correlation function for suspicious changes in width or shape, so that such false positives can be flagged during the candidate vetting process.

2.2 Introduction

As a part of the third phase of the Sloan Digital Sky Survey (SDSS-III; Eisenstein et al., 2011), the MARVELS (*M*ulti-object *A*PO *R*adial *V*elocity *E*xoplanet *L*arge-area *S*urvey) project is searching for substellar companions by monitoring the radial velocities (RVs) of 3330 FGK stars (Ge et al., 2008, 2009; Ge & Eisenstein, 2009). This sample size is large enough for the project to find relatively rare objects, such as brown dwarf (BD) companions to solar-type stars. The paucity of observed BD companions to solar-type stars with separations of $\lesssim$5 AU is typically referred to as the BD desert (Marcy & Butler, 2000). Since the size of the MARVELS sample allows us to begin to quantify how arid the BD desert may be, any MARVELS discovery of a BD in the desert (or lack thereof) is a step toward increasing our understanding of BD formation.

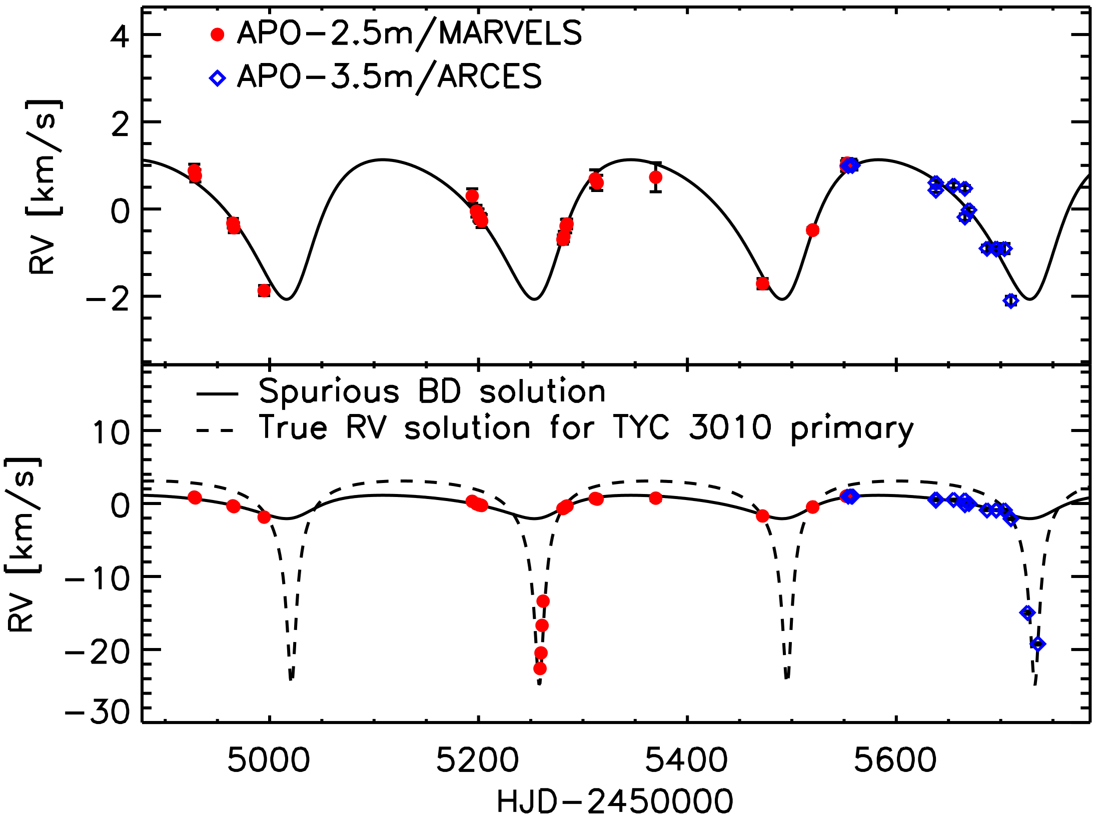

Figure 2.1: The radial velocity data obtained with the MARVELS (red) and ARCES (blue) spectrographs at the time that we began to suspect that TYC 3010 was a double-lined spectroscopic binary (SB2) instead of a brown dwarf (BD) companion to a solar-type star. In the top panel, we show the EXOFAST fit (solid line; Eastman et al., 2013) to the low-amplitude RV variations that are observed when the binary is away from periastron. This solution corresponds to a substellar companion in the BD regime ($M \sin i \sim 50\, M_{\rm Jup}$) orbiting a solar-type primary with a period of ~238 days. In the bottom panel, we include the high-amplitude MARVELS (red points near HJD 2455250) and ARCES (blue points near HJD 2455730) outliers that were initially thought to be spurious, as well as the final, true RV curve (dashed line) for the primary component of the SB2. For both spectrographs, the majority of the data agrees well with the BD solution, and it is tempting to suspect the outliers as spurious. However, upon investigating the cross-correlation function (CCF) for these outliers, the CCFs show strong evidence for a secondary stellar component (see Figure 2.3). With the HET/HRS spectrograph we were able to completely cover periastron and confirm that the system is indeed a double-lined spectroscopic binary. Most of the data points are offset from the dashed curve because these points actually correspond to the flux-weighted average of the true primary and secondary RVs. To perform the double-lined fit for these (apparently) single-lined epochs, we first disentangled the primary and secondary components as described in Section 2.4.2.1.

In addition to its large homogeneous target sample, MARVELS differs from other surveys for substellar companions in two key ways. First, the project employs a dispersed fixed-delay interferometer (DFDI; Ge, 2002; Ge et al., 2002; Erskine, 2003; Ge et al., 2006; van Eyken et al., 2010; Wang et al., 2011). Second, it uses a multi-object spectrograph to observe 60 stars simultaneously (Ge et al., 2009). The DFDI prototype instrument was used to discover the first extrasolar planet around HD 102195 in 2006 with this new RV method (Ge et al., 2006). The MARVELS DFDI technique combines an interferometer with a medium resolution spectrograph ($R\sim$12,000) in order to obtain a precision of ~100 m s^{-1}. Given its RV precision and survey design to monitor each target with at least 24 RV measurements over at least 1 yr, MARVELS is sensitive to BD and low-mass stellar companions with periods ranging from a few days to hundreds of days. Nonetheless, certain specific types of astrophysical false positives can mimic substellar companions unless additional vetting is performed. This paper describes just such a case, TYC-3010-1494-1 (hereafter TYC 3010), a stellar binary that initially appeared as a single star with a substellar companion and that, through a confluence of orbital parameters, continued to masquerade as such despite a disconcertingly extensive amount of observation and analysis.

When we began analysis of TYC 3010, MARVELS and its pilot project had already detected two BD candidates (Fleming et al., 2010; Lee et al., 2011) orbiting late F stars in the BD desert[1]. The MARVELS discovery data indicated that TYC 3010 possessed a substellar companion with a minimum mass of $\sim 50\,M_{\mathrm{Jup}}$ and that it was on a ~238-day moderately

---

[1] Subsequently, MARVELS has discovered three more candidates in the desert: Ma et al. (2013); Jiang et al. (2013); De Lee et al. (2013)

eccentric orbit with an RV amplitude of $\sim$1.5 km s^{-1} (see the top panel of Figure 2.1). However, given the cadence of MARVELS and the period of the orbit, there were significant gaps in the phase coverage and additional observations with a different spectrograph were required to constrain the RV solution. Initially, the follow-up data remained fully consistent with the BD companion scenario. However, during the course of the program, we found two RV points that were shifted by $\sim$20 km s^{-1} with respect to most of our data; while investigating the source of these anomalous points, we realized that a few similar points had been rejected from our MARVELS discovery data by the team's outlier rejection procedures (see bottom panel of Figure 2.1). Examining the cross-correlation function (CCF) of the anomalous RV points (in both the discovery and subsequent data) revealed evidence that there were two components in the CCF, which suggested that the companion to the primary was most likely a stellar-mass secondary. Finally, including the initially flagged outlier measurements and disentangling the RV measurements of the two components, the system was found to be a nearly equal-mass stellar binary ($q \sim 0.88$) on a highly eccentric orbit ($e \sim 0.8$). Evidently, for a system like TYC 3010, it is possible to clip just a few measurements and obtain an apparently reasonable solution that is convincing but completely incorrect.

As large scale RV and transit surveys for exoplanets become more common, it is increasingly inevitable that any and all forms of astrophysical false positives, despite their rarity, will be found. Indeed, the first BD candidate discovered by the MARVELS project, MARVELS-1 (Lee et al., 2011), appeared to exhibit evidence for an additional planet-mass companion, but turned out instead to likely be a quadruple system, comprising four stars with no detected BD or planetary-mass companion (Wright et al., 2013). Akin to TYC 3010, MARVELS-1 is a double-lined spectroscopic binary; the stars have relative RVs which are sufficiently low that they are always blended, even at the resolution of the Hobby-Eberly Telescope (HET; $R \sim 60,000$ mode). Thus, with both MARVELS-1 and TYC 3010, we actually measure a flux-weighted mean of two sets of stellar spectral lines. This flux-weighted mean exhibits a suppressed velocity shift that mimics a single-lined binary with a BD secondary. Both systems possess geometries that allow them to masquerade as less massive systems: MARVELS-1 is nearly face-on, which leads to low projected velocities, while TYC 3010 is on a highly elliptical orbit with a semi-major axis oriented nearly perpendicular to our line of sight.

Similarly, Mandushev et al. (2005) describe what at first appeared to be a transiting BD companion to an F star from the TRES transit survey, but turned out instead to be an F star blended with a G+M stellar eclipsing binary. The system that we describe here follows these unfortunate examples, and is similarly pernicious.

In the following sections, we present our analysis as a kind of cautionary tale for other RV surveys to avoid similar false positives. In Section 2.3, we describe the spectroscopic and photometric data obtained for TYC 3010. In Section 2.4, we discuss in detail the nature of the evidence that led us to conclude that TYC 3010 was an eccentric stellar binary instead of a BD companion to a solar-type star. We also present the properties we derived for both components of the spectroscopic binary. In Section 2.5, we discuss the circumstances that allowed this false positive to masquerade for so long and through several vetting steps as a compelling detection of a substellar companion, and we describe methods that the MARVELS team and other RV surveys can use to recognize this kind of astrophysical false positive in the future. Finally, in Section 2.6, we conclude with a summary of the main results.

2.3 Observations and Data Processing

We obtained a total of 65 RV measurements from the Sloan 2.5m, the APO 3.5m, and the HET 9.2m telescopes. We will briefly summarize the characteristics of the data from all three telescopes. For more details of the analysis, please see Fleming et al. (2010), Lee et al. (2011), and Wisniewski et al. (2012).

2.3.1 SDSS-III MARVELS Discovery RV Data

A total of 28 spectra (see Table II.1) of TYC 3010 were obtained with the Sloan 2.5m telescope (Gunn et al., 2006) at Apache Point Observatory (APO). The multi-fiber MARVELS spectrograph (Ge et al., 2009) can simultaneously measure the RVs of 60 stars during each telescope pointing. Both beams of the interferometer are imaged onto the detector, so each 50-minute observation results in two fringed spectra in the wavelength range of ∼500–570 nm with a resolving power of $R \sim 12,000$. The MARVELS interferometer delay calibrations are described in Wang et al. (2012a,b). For more details on how the data were reduced and analyzed to yield RVs, see Lee et al. (2011).

As described below, it proved essential to examine the CCFs of the individual spectra.

Table II.1. Observed heliocentric single-lined radial velocities for TYC 3010

HJD	Instrument[a]	RV (km s^{-1})	σ_{RV} (km s^{-1})
2454927.82470	M	62.681	0.148
2454928.85061	M	62.564	0.139
2454964.76792	M	61.479	0.108
2454965.77714	M	61.374	0.113
2454994.69536	M	59.933	0.115
2455471.98302	A	60.138	0.116
2455519.95995	A	61.359	0.052
2455519.98157	A	61.371	0.051
2455903.90846	H	62.448	0.051
2455917.87269	H	62.237	0.060
2455928.84083	H	61.759	0.046
2455940.80855	H	61.122	0.058
2455946.80490	H	60.285	0.055
2455950.80134	H	59.539	0.045
2455953.82447	A	58.385	0.049
2455954.00566	H	58.467	0.050

[a] Instruments: MARVELS (M), ARCES (A), and HRS (H) spectrographs.

Note. — The ARCES and HRS RV values were measured as absolute heliocentric RVs, while the MARVELS discovery data were measured on a relative instrumental scale; the MARVELS RVs have been offset to the same (heliocentric) scale as the ARCES and HRS measurements. *This table is provided in its entirety in the appendix. A portion is shown here for guidance regarding its form and content.*

Table II.2. Observed heliocentric double-lined radial velocities for TYC 3010

HJD	Instrument[a]	$RV_{primary}$ (km s^{-1})	$\sigma_{RV_{primary}}$ (km s^{-1})	$RV_{secondary}$ (km s^{-1})	$\sigma_{RV_{secondary}}$ (km s^{-1})
2455725.68377	A	46.012	0.167	75.222	0.257
2455735.62781	A	43.197	0.251	81.056	0.175
2455956.76037	H	53.788	0.030	69.104	0.063
2455959.78075	H	51.409	0.025	71.807	0.055
2455964.75592	H	44.163	0.026	80.066	0.055
2455964.83117	A	44.884	0.071	79.700	0.372
2455967.75334	H	36.755	0.030	88.389	0.062
2455967.82824	A	37.684	0.076	88.651	0.471
2455968.74640	H	34.456	0.025	90.966	0.054
2455971.73989	H	36.359	0.029	88.685	0.060
2455972.97350	H	40.368	0.025	84.354	0.054
2455976.73787	H	50.072	0.024	73.253	0.051
2455977.71541	H	51.788	0.028	71.580	0.058
2455978.71767	H	52.990	0.026	69.840	0.056
2455979.71599	H	54.160	0.029	68.450	0.062

[a] Instruments: ARCES (A) and HRS (H) spectrographs.

However, performing a cross-correlation on a DFDI spectrum requires a few steps beyond what one performs for a typical slit or cross-dispersed echelle spectrograph. In both cases the images are reduced using standard techniques (bias subtraction, trace correction, flat fielding etc.) Once a fully processed two-dimensional spectrum has been extracted, there is a divergence in the techniques. In the case of a normal spectrum, one merely sums the flux in the slit (channel) direction to produce a one-dimensional spectrum. This approach is not possible in the DFDI technique because the fringing pattern will introduce false fluctuations in total flux if one just sums in the slit direction. These fluctuations will be a function of the phase of the fringe pattern in each pixel channel. To correct for this effect, a sinusoidal function of the form $A \sin(wx + b) + c$ is fit to each pixel column. For the purposes of cross-correlation the only term of interest is c, or the mean flux in each channel. A one dimensional spectrum is then constructed using the c term in each channel. From this point forward the CCF is determined using standard techniques.

2.3.2 APO-3.5m/ARCES RV Data

A total of 19 RV observations were taken with the APO 3.5m telescope using the ARC Echelle Spectrograph (ARCES; Wang et al., 2003). This spectrograph operates in the optical regime from ∼3,600–10,000Å with a resolving power of $R \sim 31,500$. The first set of observations were taken from 2010 October to 2011 June. The second set of observations, which were undertaken with the goal of increasing phase coverage of periastron, were obtained during 2012 January–February. As shown in Tables II.1 and II.2, there were 15 ARCES points observed outside of periastron, and 4 points during periastron (The first two of these periastron points are where we initially resolved both the primary and secondary spectral lines—see bottom panel of Figures 2.1, 2.2, and 2.3—and began to suspect that the system might be a double-lined spectroscopic binary).

To achieve high-accuracy RV measurements with the echelle spectrograph, we obtained a Thorium-Argon (ThAr) exposure after every science exposure. In order to place TYC 3010 on an absolute RV scale, we also frequently bracketed our observations of TYC 3010 with observations of the RV standard HD 102158, which has an absolute RV of 28.122 km s^{-1} (Crifo et al., 2010; Nidever et al., 2002). From the standard deviation of the 13 RV measurements we obtained for HD 102158 (see Table II.3), we were able to determine that the ARCES spectrograph possesses an RV stability of ∼0.5 km s^{-1}.

Two of the ARCES spectra were taken with longer exposure times in order to achieve a high signal-to-noise ratio (S/N) for deriving the fundamental stellar parameters (see Section 2.4.2.2). These two spectra were taken with an exposure time of 200 s and with the default slit setting described in Wisniewski et al. (2012). The data were reduced with IRAF, and after barycentric corrections and continuum normalization, the two spectra were combined to produce a final spectrum with an S/N of ∼170 per resolution element at ∼6500 Å. However, once we realized that TYC 3010 was a double-lined spectroscopic binary, we re-derived the spectroscopic parameters with a double-lined spectrum obtained near periastron, as described in Section 2.4.2.2.

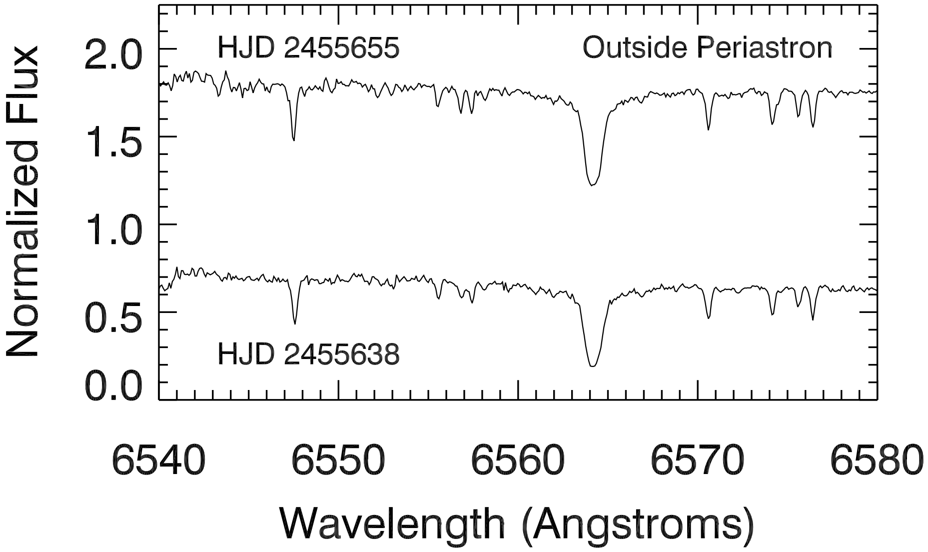

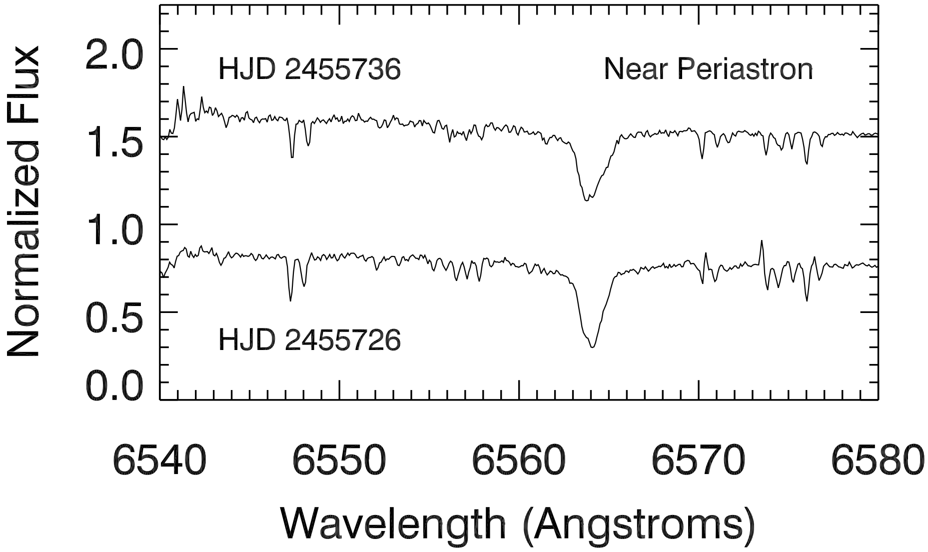

Figure 2.2: (Top) Outside periastron the combined spectrum appears convincingly single-lined. (Bottom) Near periastron the spectrum is resolved into its double-lined components (with the ARCES and HRS spectrographs, but not MARVELS). We used the double-lined spectrum with highest S/N when we were deriving the properties of the two stars via spectral characterization.

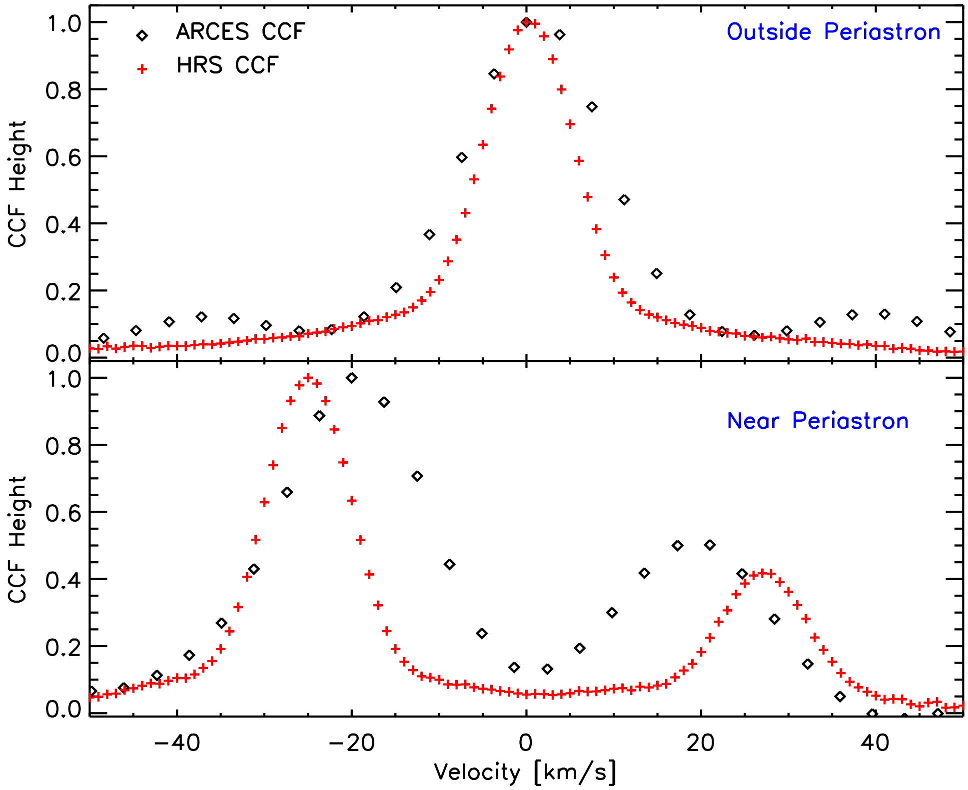

Figure 2.3: Example CCFs obtained with the ARCES and HRS spectrographs from similar (but different) phases outside of periastron (*top panel*) and during periastron (*bottom panel*). Since most of the data were obtained outside of periastron, most of the RV points correspond to single-peak CCFs. However, for data from near periastron, the ARCES and HRS spectrographs are able to resolve two peaks. The secondary peak is comparable in height to the primary peak, which led us to suspect that TYC 3010 is an eccentric spectroscopic binary with the semi-major axis aligned perpendicular to the line of sight (see Figure 2.8). With this configuration, we would only resolve two peaks in the CCF if we happen to catch the pair of stars as they briefly pass through periastron. To confirm this interpretation, we fully observed periastron with HET/HRS, which allowed us to completely constrain the orbit (see Figure 2.7).

2.3.3 HET/HRS RV Data

Upon realizing the eccentric binary-star nature of the object from the APO 3.5m data, observations where initiated with the 9.2m HET (Ramsey et al., 1998) and the Higharcsec Resolution Spectrograph (HRS; Tull, 1998) at a resolving power of $R \sim 30,000$ using a 2 arcsec optical fiber. A total of 18 observations were obtained to completely cover periastron, and thereby fully constrain the orbit. The queue-scheduled observing mode of the HET (Shetrone et al., 2007) is extremely well suited for investigating objects that require monitoring over a long timespan, as well as targeted observations near periastron passage. For wavelength calibration, ThAr images were obtained immediately before and after the science exposure to aid in calibrating any possible instrument drift. The data were reduced and wavelength calibrated using custom optimal extraction scripts written in IDL. RVs were measured using two different techniques, which we describe below. The HET observations clearly resolve the orbit for TYC 3010, and constrain the eccentricity to a value of $e \sim 0.8$ (see Section 2.4.2).

2.3.3.1 CCF Mask

RVs were measured using a cross-correlation mask derived from National Solar Observatory Fourier transform spectroscopic solar data (Lytle, 1993), and a technique similar to that described by Baranne et al. (1996). The resultant CCF encodes information from the ∼400–600 nm region, and we elected not to use redder wavelengths due to issues with telluric contamination. Figure 2.3 shows the resulting CCF for an epoch during periastron and one

Table II.3. Observed heliocentric radial velocities for HD102158

HJD	RV (km s^{-1})	$\sigma_{\rm RV}$ (km s^{-1})
2455654.81577	28.734	0.052
2455665.67180	28.050	0.034
2455665.71479	28.169	0.043
2455669.58461	27.736	0.045
2455686.80825	27.470	0.054
2455695.68591	28.030	0.038
2455695.72570	28.090	0.034
2455703.60341	28.244	0.039
2455709.76151	27.476	0.030
2455725.66705	26.692	0.123
2455735.61237	28.126	0.109
2455964.81467	28.093	0.058
2455967.81369	27.728	0.050

outside of periastron; as is the case for the ARCES data, during periastron the primary and secondary peaks are clearly visible in the HET CCFs, but outside of periastron only a single peak is resolved. The centroid of the CCF peak is determined by fitting a Gaussian.

This technique has been used successfully for isolated stars to derive precise RVs by the teams using fiber-fed high resolution spectrographs (e.g., HARPS, SOPHIE, ELODIE, CORALIE; Pepe et al., 2000; Bouchy, 2006; Baranne et al., 1996; Queloz et al., 2000), since PSF stability is an important component of deriving precise RVs with this technique. Any mismatch between the CCF and the simple Gaussian model is absorbed as a zero-point offset in the derived RVs as long as the PSF is stable (resulting in a stable CCF shape). The HET/HRS spectrograph is also fiber-fed, enabling this technique to also be applied to binary stars. This method is computationally efficient, and also does not require that the spectra be normalized, resulting in a quick turn around in determining RVs once the data are in hand. The RVs derived enabled us to plan and obtain observations as soon as the peaks began to separate on the approach to peri-passage. Table II.1 shows the HET RVs obtained with this technique for those epochs where the CCF appears as a single peak.

2.3.3.2 TODCOR

While the CCF Mask technique described above works quite well, it does not yield the best RVs possible for spectra with two CCF peaks since only one mask (G2 spectral type) was used in determining peak positions. Once all the data were in hand, we were able to apply the two-dimensional cross-correlation algorithm, TODCOR (Zucker & Mazeh, 1994). TODCOR can simultaneously cross-correlate two stellar templates against a blended target stellar spectrum to disentangle the stellar RVs of the components as well as derive a flux ratio. We used TODCOR along with HRS observations of HD161237 (G5V) and HD 198596 (K0V) as templates to measure the RVs of TYC 3010. The HRS spectrum was divided into different bandpasses, and each bandpass was solved independently following Zucker (2003) and the resulting cross-correlation surface combined with a maximum likelihood analysis. Further details on our implementation of the TODCOR algorithm, as well as details of our custom HRS spectral extraction pipeline, can be found in Bender et al. (2012).

Table II.2 shows the RVs of the primary and secondary determined using this algorithm at those epochs where the CCF is double peaked. We add 0.05 km s^{-1} in quadrature to the

TODCOR formal errors to account for additional noise effects like wavelength calibration, small tracking induced PSF changes, etc. While the HET observed the target on 18 epochs, the secondary RVs are only reliably measured for 11 epochs. These are the epochs where the primary and secondary peaks are sufficiently separated to determine an independent RV for each. While RVs can be determined for the other 7 epochs, they are RVs of blended spectra, and the associated systematic error is not only larger, but also more difficult to quantify.

Since both peaks are unambiguously detected in TODCOR at these epochs, we are also able to measure the secondary to primary flux ratio, α, which we determine to be $\alpha = 0.335 \pm 0.035$ by averaging the flux ratio of the templates (G5V and K0V) over four bandpasses spanning 4663-5863 Å. Finally, the mass ratio derived from these 11 epochs is $q \sim 0.88$.

2.3.4 FastCam Lucky Imaging

The MARVELS team obtained lucky imaging[2] for TYC 3010 in order to detect any spatially resolvable companions. In 2011 April, using the FastCam (Oscoz et al., 2008) instrument on the 1.5m TCS telescope at Observatorio del Teide in Spain, we obtained 47,000 frames in the I-band with a 70 ms exposure time for each frame. Data processing was accomplished with a custom-made IDL pipeline.

As described in Fleming et al. (2012), the best frames are selected via the brightest pixel (BP) method. The frames with the brightest $X\%$ of BPs are combined to generate a final

---

[2] Lucky imaging is an imaging technique that consists of taking a set of very high cadence observations in order to obtain a precision very close to the diffraction limit for a particular subset of the observations.

image, where $X = \{1, 5, 15, 30, 50, 80\}$ for TYC 3010. Figure 2.4 shows the resulting final images for each particular percentage of the best frames.

No companions are detected, but we can place constraints on the upper limit of the masses of resolvable companions. Using the spectroscopic $T_{\rm eff}$ for TYC 3010 (see Section 2.4.2.2), and the relations from Mamajek et al. (2011), we determine the bolometric magnitude. Combining the bolometric magnitude with mass–luminosity relations (Henry et al., 1999; Henry, 2004; Delfosse et al., 2000; Xia et al., 2008; Xia & Fu, 2010), we convert the detection limit for the I-band magnitude into a lower limit for the masses of detectable companions at different separations. At the 5σ level, where σ is defined in Femenía et al. (2011) as the rms of the counts within concentric annuli centered on TYC 3010, and using 8 pixel boxes, we can rule out the presence of detectable companions above a mass of $\sim 0.35\,M_{\odot}$ outside of 50 AU (see Figure 2.5).

2.3.5 Keck AO Imaging

In addition to the lucky imaging, we were also able to obtain adaptive optics (AO) images of TYC 3010 on 2012 October 21 UT using the NIRC2 imager at Keck (instrument PI: Keith Matthews; Matthews & Soifer, 1994). Observations consist of a sequence of nine dithered frames in the K' filter (central $\lambda = 2.12\mu$m) using the narrow camera (plate scale = 10 mas pix^{-1}) setting. Each frame consisted of 20 coadds with 0.1814 s of integration time per coadd, totaling 32.65 s of on-source exposure time. Images were processed using standard techniques to remove hot pixels, subtract the sky-background, and align and coadd the cleaned frames.

No candidate companions were identified in either raw or processed images. Figure 2.5 shows our sensitivity to off-axis sources as a function of angular separation. Our diffraction-limited observations rule out the presence of companions 6.5 magnitudes fainter than the primary star for separations beyond $0.5''(5\sigma)$. Using theoretical isochrones from (Girardi et al., 2002), we convert this magnitude limit to a mass upper limit, as shown in Figure 2.5; we can exclude companions with a mass above 0.13 $M_{\odot}$ outside of 100 AU.

2.4 Results

In this section we present the orbit solution of the TYC 3010 system. First we show how the data initially suggested a spurious solution in which TYC 3010 is a single star with a BD companion. Next we present the correct solution, in which TYC 3010 is shown to be a double-lined spectroscopic stellar binary (SB2) with two solar-type stars, and we provide a full characterization of the system properties.

2.4.1 Initial spurious solution: a BD companion to a solar-type star

Of the 28 RV measurements collected with the MARVELS instrument, 24 passed the data quality checks and were therefore included in the automated orbit solution fitting procedures. For the ARCES data, the first 14 consecutive RV points obtained during the initial set of observations were fully consistent with our working solution, that TYC 3010 was a candidate BD (see Figure 2.1 and Table II.4). These RV points are well fit by a solution consistent with a substellar object ($M \sin i \sim 50\, M_{\mathrm{Jup}}$) orbiting in the BD desert around a solar-type star.

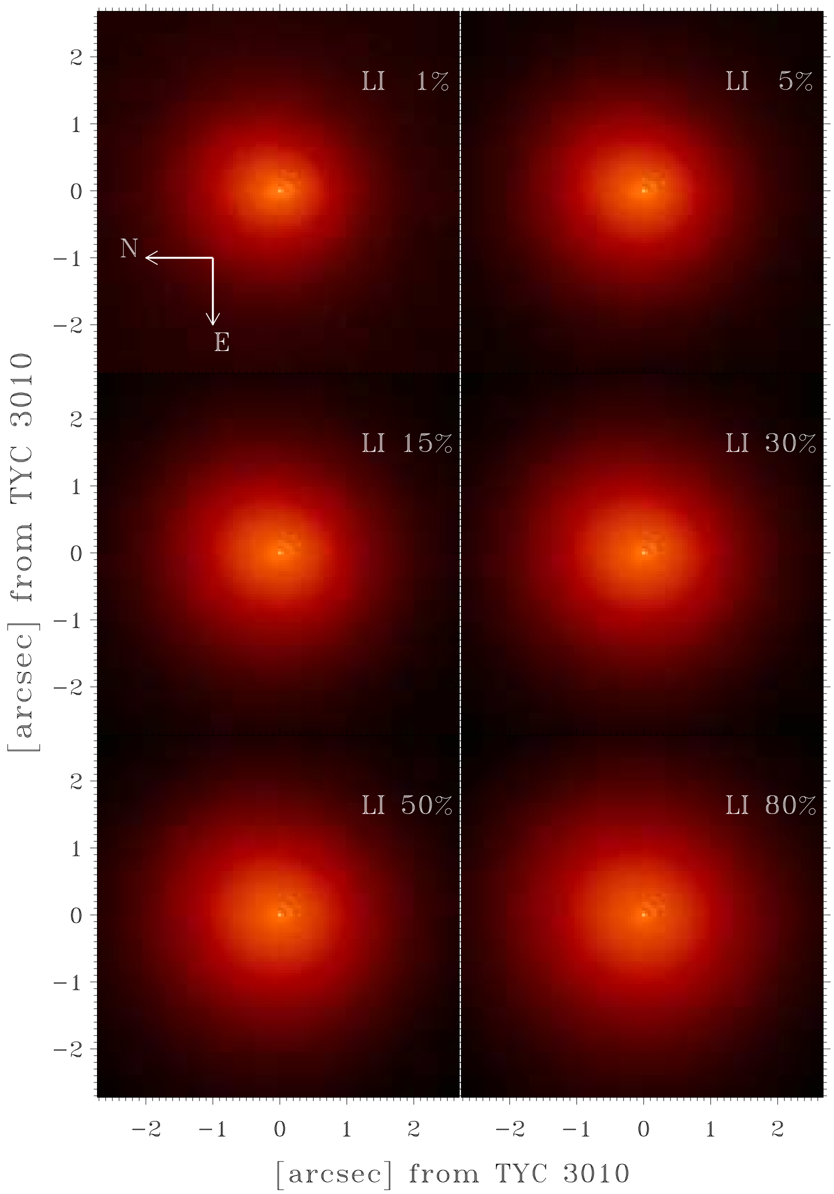

Figure 2.4: The best lucky imaging frames for TYC 3010. The best frames are selected according to the brightest pixel (BP) method as described in Section 2.3.4.

A robust fit to the low amplitude (∼1–2 km s^{-1}) variations was found with the EXOFAST program (Eastman et al., 2013), which uses a set of Markov Chain Monte Carlo trials to find the best fit. This solution, shown in Figure 2.1 (top panel), is a very convincing fit to the 38 originally included MARVELS (red points) and APO (blue points) measurements. This fit yielded a χ^2 of 34.63 after scaling the error bars to force χ^2/dof∼1. These scalings were not unreasonable compared to other MARVELS candidates.

As noted previously, four of the original MARVELS RV measurements were initially rejected as outliers. The outlier rejection procedure included a 40σ statistical clipping to avoid phase wrapping, and rejection of consecutive points deviating by a large systematic offset from the bulk of the measurements. The latter rejection step was specifically implemented in an attempt to account for cases of fiber mis-pluggings, which are known to happen on occasion, in which the wrong star is observed for a few observations in a row and those few measurements appear at a very different systemic velocity relative to the majority of the measurements. The four rejected MARVELS measurements are also shown in Figure 2.1 (bottom panel, red points) near HJD 2455250. The final (correct) orbit solution is also shown (see details below), but it must be noted that this final orbit solution is only a good fit after properly disentangling the RVs from epochs where just a single set of spectral lines is resolved; it is not a good fit to the *directly observed* single-lined RV measurements, since these are in fact a flux-weighted average of the true primary and secondary RVs. The six "outlier" measurements from this first set of observations (four MARVELS points and two ARCES points) appear systematically displaced by 15–20 km s^{-1} relative to the other 38 measurements, which are well fit by the spurious orbit (solid curve) but not by the correct orbit (dashed curve).

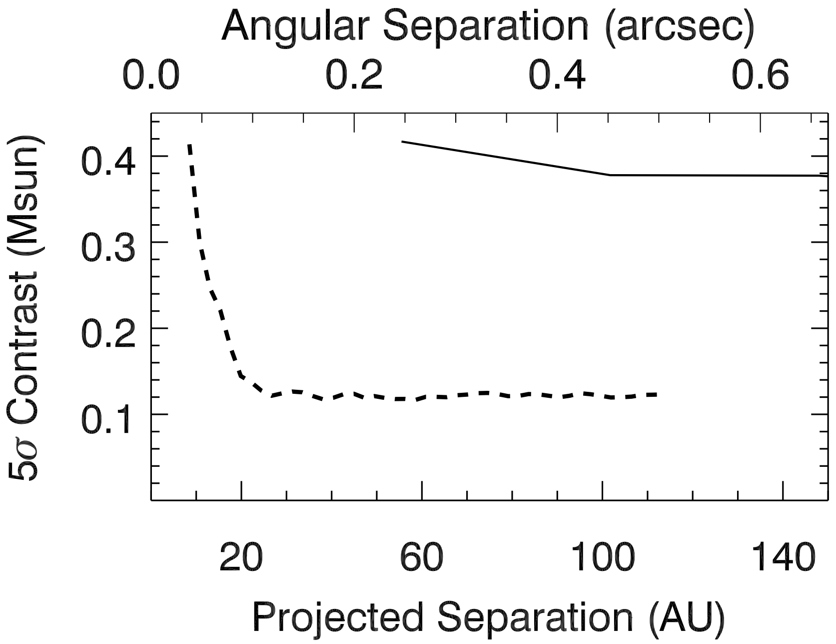

Figure 2.5: Detectability (contrast curve) for the lucky imaging (solid) and Keck AO (dashed) images obtained for TYC 3010. Given the lucky imaging and AO detection limits, we can derive an upper limit (5σ) on the mass of companions as a function of angular separation. With this upper limit, we can rule out the presence of companions above a mass of $\sim 0.35\,M_\odot$ outside of ∼50 AU, and above a mass of $\sim 0.13\,M_\odot$ outside of ∼100 AU.

In addition, as we have done with all MARVELS candidates, we performed a fit to the spectral energy distribution (SED) of the system to verify that it is consistent with a single stellar source and to provide a consistency check on the spectroscopically determined stellar properties (see below). We constructed the SED using fluxes (see Table II.5) from the Tycho catalogue (Høg et al., 2000), APASS (*A*AVSO *P*hotometric *A*ll-*S*ky *S*urvey; Data Release 6,

Table II.4. TYC 3010 orbital parameters: Spurious and True RV solutions

	Spurious solution	True solution
T_P (BJD$_{\rm TDB}$ − 2450000)	$5496.8^{+1.8}_{-2.0}$	5970.04 ± 5.1
P (days)	$238.49^{+0.73}_{-0.70}$	237.96 ± 0.04
e	$0.384^{+0.067}_{-0.048}$	0.785 ± 0.003
ω (deg)	$200.88^{+2.35}_{-2.58}$	188.86 ± 0.67
K_1 (km s^{-1})	$1.970^{+0.240}_{-0.130}$	15.38 ± 0.25
K_2 (km s^{-1})	...	17.50 ± 0.16
γ (km s^{-1})	$61.759^{+0.077}_{-0.087}$	61.28 ± 0.09
$q = M_{\rm B}/M_{\rm A}$	...	0.88 ± 0.02

Note. — The spurious solution consists of the EXOFAST (Eastman et al., 2013) fit to the MARVELS and ARCES RV data, excluding the points initially thought to be invalid outliers. The true solution was determined with the BINARY software (Gudehus, 2001) and the MARVELS, ARCES, and HRS observations. For the true (SB2) solution, the single-lined RV measurements were disentangled into their primary and secondary components (see Section 2.4.2.1).

Table II.5. Catalog Properties of TYC 3010-1494-1

Parameter	Value	Uncertainty	Reference
α (2000)	11 00 11.45		(1)
δ (2000)	+39 43 24.74		(1)
pmRA [mas yr^{-1}]	−43.4	1.7	(1)
pmDE [mas yr^{-1}]	3.3	1.6	(1)
$\mathrm{B_T}$	13.102	0.297	(1)
$\mathrm{V_T}$	11.758	0.143	(1)
B	12.007	0.153	(2)
V	11.367	0.145	(2)
I_C	10.531	0.074	(2)
g	11.579	0.177	(2)
r	11.093	0.089	(2)
i	10.870	0.127	(2)
J	9.977	0.021	(3)
H	9.554	0.016	(3)
K_s	9.488	0.019	(3)
WISE1 (3.4 μm)	9.407	0.006	(4)
WISE2 (4.6 μm)	9.482	0.006	(4)
WISE3 (12 μm)	9.470	0.038	(4)

References. — (1) Høg et al. (2000), (2) Henden et al. (2012), (3) Cutri et al. (2003), (4) Wright et al. (2010)

see Henden et al., 2012), Two Micron All Sky Survey (Cutri et al., 2003), and *WISE* (Wright et al., 2010). NextGen models (Hauschildt et al. 1999) are used to generate theoretical SEDs by holding T_eff, $\log g$, and [Fe/H] at the spectroscopically determined values (see below), and the maximum extinction A_V was limited to 0.05 mag based on the dust maps of Schlegel et al. (1998). The best fit model can be seen in the top panel of Figure 2.6; it corresponds to an A_V of 0.035 ± 0.015, and a distance of 162 ± 35 pc. This single-star SED fit to the available photometry spanning 0.2–12μm is quite good, with the only hint of a discrepancy being a mild excess that appears in the *Galaxy Evolution Explore (GALEX)* near-UV (NUV) passband, despite the lack of any strong emission in the observed Ca HK lines. However, this by itself was not sufficient to suspect the high quality orbit solution.

Thus, at this point in our analysis, fully 38 RV measurements from two separate instruments were well fit by the same orbit solution of a single, solar-type star with a $\sim 50\,M_{\rm Jup}$ companion on a modestly eccentric orbit. The SED of TYC 3010 was furthermore consistent with being a single solar-type star, and the lack of any companions in the high-resolution imaging ruled out a blend scenario in which the RV variations might be caused by a binary beyond $0.5''$ of the line of sight. Only four of the discovery RV measurements appeared to be discrepant, and these were rejected for what appeared to be good reasons, behaving not unlike fiber mis-pluggings that the MARVELS team had observed in other stars before. However, the last two RV measurements from the first set of ARCES observations appeared as strong outliers (see Figure 2.1, blue points near HJD 2455730). As they were observed with a standard echelle spectrograph, these could not be attributed to fiber mis-pluggings, and inspection of the CCFs revealed double lines (see bottom panel of Figure 2.3), immediately nullifying the BD companion hypothesis.

2.4.2 Final solution: A highly eccentric, double-lined spectroscopic binary

To further confirm that TYC 3010 was indeed a stellar binary, we closely observed the next peripassage with the HRS spectrograph on HET. With HET, we obtained complete coverage of periastron, permitting a complete double-lined orbit solution. In this section we present the correct orbit solution for TYC 3010, including all the points from the discovery and subsequent data, which shows that TYC 3010 is an SB2 with a period of $P \sim 238$ days, an eccentricity of $e \sim 0.79$, and a mass ratio of $q \sim 0.88$. With this eccentricity and orbital period, TYC 3010 lies near the upper bound of (but within) the distribution of orbital eccentricities of solar-type binaries with orbital periods of 100–300 days (see, e.g., Duquennoy & Mayor, 1991; Raghavan et al., 2010). The orbital parameters for the binary are summarized in Table II.4, the RV solution is shown in Figure 2.7, and a schematic of the orbit is shown in Figure 2.8. In this section we also describe our determination of the stellar parameters for the primary in TYC 3010, and we estimate its mass and radius using the relations described in Torres et al. (2010). Since the secondary is comparable in mass to the primary, we had to take special care in accounting for the flux contamination from the secondary, both in our determination of the stellar parameters and with the RV values that we measured for the system outside of periastron.

2.4.2.1 RV fitting

For the orbital solution of the binary, we used the RV fitting software described in Gudehus (2001). Since we do not resolve two sets of spectral lines for the phases outside of periastron, most of the RV points correspond to a flux-weighted average of the primary and secondary RVs. In order to de-blend the flux-weighted RVs that we measured, and derive the corresponding primary RVs, we used the following prescription.

We treat the blended velocities as a flux-weighted average of the primary and secondary velocities:

$$v_{\rm blend} = \frac{v_A F_A + v_B F_B}{F_A + F_B}, \tag{2.1}$$

where v_A and v_B are the primary and secondary velocities respectively, and F_A and F_B are the primary and secondary fluxes. We normalize the flux weights by setting the sum of the fluxes, $F_A + F_B$, to unity. Using the flux ratio, $\alpha = F_B/F_A$, from the TODCOR analysis (which was only performed for the HET/HRS epochs where it was possible to resolve two sets of spectral lines), we can solve for F_A and F_B in terms of α:

$$F_A = \frac{1}{1+\alpha}; \quad F_B = \alpha F_A. \tag{2.2}$$

In addition, we can use the mass ratio, $q = M_B/M_A$, from the RV solution to write v_B in terms of v_A, since $M_B/M_A = v_A/v_B$.

$$v_B = -v_A\left(\frac{M_A}{M_B}\right) = \frac{-v_A}{q} \tag{2.3}$$

Returning to (2.1), we can now write

$$v_A = \frac{v_{\mathrm{blend}}}{F_A - F_B/q} = \left(\frac{1+\alpha}{1-\alpha/q}\right) v_{\mathrm{blend}} \tag{2.4}$$

With Equation (2.4), we can iteratively solve for a final set of de-blended RVs for the primary. For the first iteration, we provide an initial guess for q by performing a joint fit to the primary RVs (blended+unblended) combined with the secondary RVs (unblended; only measured during periastron). Inserting this initial guess for q into Equation (2.4), we derive an initial set of de-blended primary RVs. Then we perform another joint fit to the primary (de-blended+unblended) and secondary (unblended) RVs to refine our value for q. We repeat the process until q converges. The value we find for q (0.878 ± 0.016) from this de-blending analysis is in excellent agreement with the value for q ($\sim$0.88) that we found from the ratio of the primary and secondary RVs that were measured for the 11 HET/HRS epochs where two peaks were resolved in the CCFs. Thus, q has been determined very precisely by the orbital solution (better than 3%), and is more precise than the individual quoted errors on the masses.

As a further consistency check on α and q, we also note that according to the relationship between mass and bolometric luminosity from Torres et al. (2010), there should be a relationship between α and q. Since α is derived from a set of finite wavelength bands, it is not bolometric. However, since the stars have temperatures that are not too dissimilar, α is likely to be approximately equal to the ratio of the bolometric luminosities. For stars with $M = 0.6 - 1.2\,M_{\odot}$, a fit to the Torres et al. (2010) data yields $L \propto M^{5.1}$. Thus, $\alpha = q^{5.1}$, so $q \sim (0.335)^{1/5.1} \sim 0.81$, which is within 3σ of the value obtained from the RV analysis.

2.4.2.2 Determining the stellar parameters for TYC 3010

The stellar parameters for the primary were determined with a double-lined spectrum obtained near periastron (see Section 2.3.2). The spectroscopic analysis used to determine the atmospheric parameters is similar to the one described in Wisniewski et al. (2012), where we use two independent methods that require the conditions of excitation and ionization equilibria for Fe I and Fe II lines. These methods are referred to as the "BPG" (Brazilian Participation Group) method and the "IAC" (Instituto de Astrofísica de Canarias) method.

Table II.6. TYC 3010 properties derived by this work

System Properties		
Parameter	Value	Uncertainty
$\alpha = F_{\rm B}/F_{\rm A}$	0.335	0.035
$q = M_{\rm B}/M_{\rm A}$	0.878	0.016
A_V	0.03	0.02
d (pc)	225	40
	TYC 3010 A	TYC 3010 B
$T_{\rm eff}$ (K)	5589 ± 148	4600 ± 850
$\log g$ (cgs)	4.68 ± 0.44	4.60 ± 0.20
[Fe/H]	0.09 ± 0.20	...
M ($M_\odot$)	$1.04^{+0.15}_{-0.12}$	$0.73^{+0.24}_{-0.23}$
R ($R_\odot$)	$0.75^{+0.54}_{-0.27}$	$0.68^{+0.23}_{-0.18}$

Note. — The properties for the primary were determined by the spectroscopic stellar parameters and the Torres et al. (2010) relations. The properties for the secondary were determined from the stellar parameters found by the two-component fit to the SED and the Torres relations.

The "BPG" analysis was done in local thermodynamic equilibrium (LTE) using the 2002 version of MOOG[3] (Sneden, 1973) and one-dimensional plane-parallel model atmospheres interpolated from the ODFNEW grid of ATLAS9 models (Kurucz, 1993; Castelli & Kurucz, 2004). In previous MARVELS papers (e.g., Wisniewski et al., 2012, and references therein), the equivalent widths (EWs) of the Fe lines were determined in an automated fashion. However, in this case, the EWs were manually measured to carefully account for visible blends on the Fe lines from the secondary's spectrum. We note that contaminations from very weak lines could have affected the EW measurements. In order to correct the EWs measured for the primary for the veiling from the continuum flux of the secondary star, we followed a procedure similar to the one described in Section 5.2.1 of González Hernández et al. (2008). According to their prescription, we can relate the value of the true equivalent width ($\mathrm{EW}_{\mathrm{true}}$) of a given line to the observed equivalent width ($\mathrm{EW}_{\mathrm{obs}}$) through the following relationship,

$$\mathrm{EW}_{\mathrm{true,A}} = f_{\mathrm{A}} \left(\mathrm{EW}_{\mathrm{obs,A}} \right) \tag{2.5}$$

where f_{A} is the so-called veiling factor for the primary. The veiling factors for the two components are related by

$$\frac{f_{\mathrm{B}}(\lambda)}{f_{\mathrm{A}}(\lambda)} = \frac{F_{\mathrm{A}}(\lambda)}{F_{\mathrm{B}}(\lambda)} = \frac{1}{\alpha}, \tag{2.6}$$

where F_{A} and F_{B} are the fluxes for the primary and secondary. Furthermore, the veiling

---

[3] http://www.as.utexas.edu/~chris/moog.html

factors satisfy the equation

$$\frac{1}{f_{\rm A}(\lambda)} + \frac{1}{f_{\rm B}(\lambda)} = 1 \tag{2.7}$$

To simplify our analysis, we treated the veiling factors and flux ratio as if they were wavelength independent. Using the average flux ratio derived by TODCOR ($\alpha = F_B/F_A = 0.335 \pm 0.035$; see Section 2.3.3.2), and the added constraint from Equation 2.7, we find the veiling factor for the primary to be $f_{\rm A} \sim 1.34$. Thus, after correcting the EWs, we find the stellar parameters to be $T_{\rm eff} = 5589 \pm 148$ K, $\log g = 4.68 \pm 0.44$, and [Fe/H]$= 0.09 \pm 0.20$ (see Table II.6). The uncertainties for these parameters are larger than the typical errors that we achieve with our spectroscopic analysis because of the flux contamination from the secondary star.

The "IAC" analysis extracted the stellar parameters of the primary and secondary stars by considering veiling factors that were wavelength-dependent. These veiling factors are estimated using low-resolution Kurucz fluxes (Allende Prieto & Lambert, 2000, and references therein) and the following equation:

$$\frac{f_{\rm B}(\lambda)}{f_{\rm A}(\lambda)} = \frac{\Gamma_{\rm A}(\lambda)}{\Gamma_{\rm B}(\lambda)}\left(\frac{R_{\rm A}}{R_{\rm B}}\right)^2, \tag{2.8}$$

where $\Gamma_{\rm A}$ and $\Gamma_{\rm B}$ correspond to the surface brightness of the primary and the secondary respectively. To determine the ratio of the radii, we derived an empirical mass–radius relationship from a sample of 55 stars from Torres et al. (2010), with the masses restricted to

$0.7\ \mathrm{M}_\odot < M < 1.4\ \mathrm{M}_\odot$. We fit a function to the data of the form

$$\log R/R_\odot = a \log(M/M_\odot) + b, \tag{2.9}$$

where $a = 1.052 \pm 0.097$ and $b = 0.036 \pm 0.008$. Thus, the ratio of the radii for the components of TYC 3010 can be written as

$$R_\mathrm{A}/R_\mathrm{B} = \Big(M_\mathrm{A}/M_\mathrm{B}\Big)^{1.052} \tag{2.10}$$

The mass ratio was determined from the TODCOR analysis to be $q = M_B/M_A \sim 0.88$, so we find that $R_A/R_B = 1.142$.

As a first guess, we adopt the above values to estimate the stellar mass and radius of the primary (Allende Prieto et al., 2004; Reddy et al., 2006; Ramírez et al., 2007), from solar-scaled theoretical isochrones (Bertelli et al., 1994). The mass ratio allows us to derive a first guess of the $T_\mathrm{eff,B}$ value for the secondary to be roughly 5100 K, assuming $\log g \sim 4.70$ and the same metallicity as the primary. The stellar radii we get from the comparison with isochrones are 0.89 $R_\odot$ and 0.77 $R_\odot$, and thus the ratio is $R_A/R_B = 1.145$, which is very similar to the value previously estimated ($R_A/R_B = 1.142$). Thus, the derived veiling factors lie in the range $f_{\lambda,A} \sim 1.45 - 1.55$ and $f_{\lambda,B} \sim 3.20 - 2.85$ in the spectral region 4500–7000 Å.

We then measure automatically, using the code ARES (Sousa et al., 2007), the EWs of the Fe I and Fe II lines (Sousa et al., 2008) for both stellar components and correct them using the wavelength-dependent veiling factors. We then use the code StePar (Tabernero et al., 2012) to automatically derive the stellar parameters of each component and we get $T_{\text{eff},A} = 5410 \pm 124$ K, $\log g_A = 4.57 \pm 0.56$, $[\text{Fe/H}]_A = 0.02 \pm 0.20$ and $\xi_A = 0.90 \pm 0.22$ from 162 Fe I and 18 Fe II lines. The uncertainties are unexpectedly large and may be due to the contamination of neighboring lines of other elements of the companion star. Thus the results for the secondary are fairly tentative and the errors are even larger. We were only able to measure 64 Fe I and 3 Fe II lines to get $T_{\text{eff},B} = 5136 \pm 323$ K, $\log g_B = 4.71 \pm 0.88$, $[\text{Fe/H}]_B = -0.15 \pm 0.26$ and $\xi_B = 0.75 \pm 0.40$. Compared to the "BPG" analysis, the lower $T_{\text{eff},A}$ of the primary may be related to the different methods used to derive the veiling factors. Nevertheless, the "IAC" stellar parameters for the primary star are very similar to those previously derived and are actually consistent within the large uncertainties so we decide to adopt the "BPG" values.

With the "BPG" stellar parameters for the TYC 3010 primary, we again performed a fit to the observed SED of the system as in Section 2.4.1, but now also including the contribution of the secondary star. Once again, NextGen models (Hauschildt et al., 1999) are used to generate theoretical SEDs by holding T_{eff}, $\log g$, and [Fe/H] at the spectroscopically determined values for the primary, while the T_{eff} for the secondary is found by the value that minimizes χ^2 ($\chi^2/\text{dof}= 0.75$). The best fit model can be seen in the bottom panel of Figure 2.6; it corresponds to an A_{V} of 0.03 ± 0.02, and a distance of 225 ± 40 pc. Compared to the SED fit performed in Section 2.4.1, which assumed a single stellar contribution, this two-component SED fit no longer exhibits an excess in the *GALEX* NUV passband, and more generally is an excellent fit to all of the available photometry. Finally, from this two-component fit to the SED, we also obtain a set of values for the stellar parameters of the secondary of TYC 3010. We find that $T_{\rm eff} = 4600 \pm 850$ K, $\log g = 4.6 \pm 0.2$, and [Fe/H]$= 0.05 \pm 0.19$.

2.4.3 Inferred evolutionary status of TYC 3010

Given the spectroscopic stellar parameters, we can derive the mass and radius of the TYC 3010 primary star using the empirical relationships described in Torres et al. (2010). Figure 2.9 shows the result of a set of MCMC trials for the best estimate of the mass and radius. For the precise parameters of the primary ($T_{\rm eff} = 5589$ K, $\log g = 4.68$, [Fe/H]=0.09), the Torres relations give 0.98 $M_\odot$ and 0.75 $R_\odot$. Once one includes the fairly large uncertainties in the stellar parameters, the median values for the mass and radius become $1.04^{+0.15}_{-0.12}\,M_\odot$ and $0.75^{+0.54}_{-0.27}\,R_\odot$, respectively. The means are $1.05 \pm 0.15\,M_\odot$ and $0.90 \pm 0.54\,R_\odot$, so the distributions are quite skewed as shown in Figure 2.9. Compared to a Yonsei-Yale evolutionary track (see Figure 2.10), we do not have a strong constraint on the age, but TYC 3010 is unlikely to have evolved off the main sequence.

We can also derive the mass and radius for the secondary given the stellar parameters determined from the two-component SED fit and the Torres et al. (2010) relations. We find that $M_B = 0.74^{+0.26}_{-0.23}\,M_\odot$ and $R_B = 0.76^{+0.27}_{-0.19}\,R_\odot$. This value for the mass of the secondary agrees within 1σ of the value that can be derived using the primary mass we determined above and the mass ratio from the RV solution, i.e., $M_B \sim 0.89\,M_\odot$.

2.5 Discussion

2.5.1 Why we initially derived a spurious solution

The RV signal from TYC 3010 initially seemed to indicate that it was a BD orbiting a solar-type star in the BD desert. Over 80% of the MARVELS discovery data agreed with this interpretation, and there seemed to be plausible reasons for excluding the outliers. However, once similar outliers were found in the subsequent observations, we began to suspect the validity of the BD interpretation. In this section, we discuss in detail why we initially favored the BD interpretation, as well as how this conclusion was abruptly overturned by a few surprising data points.

In the discovery data, there were four outliers in total, each offset by $\sim$20 km s^{-1} from the rest of the data. The most anomalous of the outliers was extracted from a spectrum with a low S/N, so its RV value did not seem trustworthy. The remaining outliers (considering that they corresponded to a $\sim$20 km s^{-1} offset in RV that was only captured once during the three orbits contained in the discovery data), also seemed likely to be spurious. The MARVELS spectrograph is a fiber-fed spectrograph that can observe 60 objects simultaneously. Each fiber is plugged by hand to observe the correct target, and occasionally a mistake may occur. Indeed, the MARVELS data vetting procedures were evolved to specifically include an outlier rejection step that sought to mitigate such errors, by searching for consecutive strings of measurements that were offset from the bulk of the data in a similar fashion to how these four measurements behave.

Remarkably, excluding these few apparent “outliers”—and in fact *only* by excluding them—permits a convincing orbit solution. It is not intuitive that this should be the case, in particular because only ∼15% of the measurements are excluded (including both the discovery data and the initial follow-up data which appeared to corroborate the spurious solution) and because the resulting solution is so dramatically different from the true solution. Evidently, a system such as TYC 3010 (with its extreme eccentricity, leading to punctuated large RV excursions, and its orbital orientation being nearly perpendicular to the line of sight, leading to very small RV variations for ∼95% of the orbit) is able to mimic a more circular orbit of a low-mass companion about a single star. Moreover, the similarity of the two stars in TYC 3010 leads to a combined light SED that is only slightly different from that of a single star at a nearer distance.

Thus many lines of evidence supported the initial solution, considering that the BD interpretation appeared to be supported by two years of discovery RV data, six months of additional RV observations, lucky imaging, and a well-constrained SED. Indeed, when the two follow-up RV measurements observed near periastron appeared, indicating a possible problem with the original orbit solution, we began to search for reasons to suspect the validity of these two anomalous points. At first, we thought the situation might be similar to the fiber mis-pluggings believed to have occurred with the discovery data, and we considered that the ARCES outliers were the result of pointing at the wrong star. But after investigating the data from those two nights, we confirmed that we had observed the correct target. Next we learned of a recent change that had been made to the ARCES instrument: the ThAr lamp had recently been replaced. The ThAr lamp is used to perform the wavelength calibration, and it was plausible that the new lamp might have caused problems with the wavelength solution. Therefore, the ARCES outliers may have merely been the result of an artificial Doppler shift generated by an incorrect wavelength solution. In the end, we were only able to accept that the BD interpretation was incorrect after we inspected the CCF for each of the outliers. The CCFs for the outliers both showed two peaks instead of one, indicating the presence of a second stellar component. Furthermore, the secondary peak was comparable in height to the primary peak (see bottom panel of Figure 2.3), which led us to suspect that TYC 3010 was in fact a spectroscopic stellar binary.

But how did most of the data that we had for TYC 3010 conspire to imply that it was a much less massive system? The period, shape, and orientation of the orbit with respect to the line of sight (see Figure 2.8) made it such that for most of the orbit the two stars possess relatively low RVs with respect to each other. In particular, the difference between the magnitude of their RVs is smaller than the typical CCF width for our instruments, resulting in their CCF peaks being blended into one. Since the flux ratio is not too different from unity, and the mass ratio is also close to unity, for epochs where the spectral lines are blended, there is a near-cancellation (or strong suppression) of the true orbital velocities for the primary and secondary, which are nearly equal in magnitude but oppositely signed (see Equation 2.4, and recall that $v_{\rm blend}$ is what we actually measure). Thus, for ∼95% of the orbit, the amplitude of the variations (∼1–2 km s^{-1}) suggest a BD companion to a solar-type star; furthermore, the eccentricity and the orbital period ensure that the stars spend a long time (∼7 months) away from periastron, which is precisely the moment when the RVs of the components are disparate enough for it to be fairly easy to resolve the two sets of spectral lines, and the large RV amplitude ($\sim$15–20 km s^{-1}) is indicative of a stellar binary with two solar-type stars. Moreover, the orientation makes it so that only a relatively small component of the orbital velocities is directed along our line of sight. Finally, the cadence of the MARVELS survey made it unlikely to observe multiple epochs of periastron.

2.5.2 How RV surveys can identify astrophysical false positives like TYC 3010

For any given RV survey, the lower the resolution of the spectrograph, the more vigilant one must be for these kinds of false positives. For TYC 3010 in particular, a spectrograph with a resolution of $R \gtrsim 50,000$ is required to resolve the spectral lines throughout most of the orbit. But in general, as the resolution (and cadence of observations) decreases, the wider the range of eccentricities, arguments of periastron, and orbital periods by which stellar binaries could masquerade as substellar companions for significant fractions of their orbits.

Furthermore, longer period orbits ($P \gtrsim 1$yr) should be handled with special care, for in these cases the phase coverage is more likely to be incomplete. In order to survey $\sim$3,000 stars over four years, MARVELS required a cadence that made it less likely to observe multiple epochs of periastron for a binary with the period of TYC 3010. For MARVELS and similar RV surveys for substellar companions, it can be costly to use precious resources to examine false positives. Therefore, in this section, we describe a method that the MARVELS team currently employs to identify binaries like TYC 3010 during the candidate-vetting process.

For typical RV surveys today, a standard line bisector analysis can usually be performed to assess the presence of blended double-lined binaries. However, this was not possible for the MARVELS discovery data due to its limited spectral resolution. Thus, following our experience with TYC 3010, MARVELS has developed an internal pipeline for inspecting the widths of the CCF peaks for all of our candidates. This way, we can readily monitor the CCFs for signs that indicate that there may be more than one stellar component present (e.g., the large excursions in the width of the CCF peak that occur near periastron for TYC 3010; see Figure 2.11). There are two properties of the CCFs that we now monitor: (1) the average width of the CCF peak compared to other stars in the survey, and (2) any other significant changes in the shape of the CCF over time.

For a typical solar-type star that is not rotating too rapidly (i.e., the kinds of stars that MARVELS targets), one would expect the width of the CCF peak to be $\sim$10 km s^{-1}, which is largely the result of thermal broadening and micro-turbulence. However, when binary systems like TYC 3010 are unresolved, the widths of the CCF peak are broader ($\sim$20 km s^{-1}), indicating that there may be multiple stellar components contributing to the flux from the system (see Figure 2.11). In fact, an atypically broad CCF peak could also be the result of a single star rotating atypically fast, so a broad peak is not in itself sufficient to identify the system as a binary. Nevertheless, a broad peak should be taken as a sign to proceed with caution. Furthermore, changes in the skewness of the CCF peak might provide an even more sensitive diagnostic for these kinds of systems. Thus, by monitoring changes in the CCF peak, even if one misses the small fraction of the orbit where, depending on the resolution, the CCF peak either broadens dramatically or separates into distinct peaks (or if one is suspicious of the relatively few epochs where the system happened to be caught near periastron), it is possible to flag systems like TYC 3010, which may contain much more mass than most of the RV data suggests.

The case of TYC 3010 is also a pertinent lesson on how important it is to handle outliers carefully, especially in this era of large surveys where thousands of objects must be screened for the most favorable candidates. We possessed plausible reasons for suspecting that the outliers in the discovery data might be spurious (known issues with fiber mis-pluggings; low S/N; and the outliers were only detected during one of the three orbits observed). Moreover, and perhaps ironically, the spurious orbit solution is actually a better fit to the discovery data (excluding the outliers) than the true orbit solution, because of the need to disentangle the primary and secondary RV components from the (apparently) single-lined RV measurements. However, even when faced with such a compelling initial solution and sensible reasons for considering the outliers to be invalid, it is imperative to investigate further and provide evidence that the reasons for rejecting the outliers are not only plausible but justified.

Furthermore, when the analysis is distributed among multiple team members like it is within MARVELS, it is necessary to make sure each step of the analysis is documented as clearly as possible. For MARVELS, the members who perform the candidate-vetting are usually different from those who perform the subsequent analysis for each candidate, so it is important for each team member to be able to readily discover if any outliers were rejected and why. MARVELS has now modified its internal analysis tracking system in order to make the entire analysis process more transparent.

Finally, if we had been monitoring the widths of the CCF peaks, we could have considered the evidence of the broad peak, as well as the changing peak width around periastron, though in truth neither the changing width nor the broad peak by themselves would have likely been sufficiently compelling to reject the initial orbit solution. In the end, the most important part of our analysis was to strategically focus our HET/HRS observations on periastron, the phase where the outliers occurred and where it was easiest to resolve the spectral lines. This strategy would have been more difficult with a conventionally scheduled telescope, but was readily achieved with the queue-scheduled nature of the HET.

2.6 Summary

We have demonstrated, using high resolution spectroscopy, that TYC 3010 is an SB2. We have shown how, with a spectrograph below a given resolution ($R \lesssim 50,000$), the eccentricity and the orientation of the system with respect to our line-of-sight allowed a large fraction of the RV curve to appear remarkably similar to the kind of signal one would expect from a BD secondary as opposed to a stellar-mass secondary. Furthermore, as a result of the cadence of the MARVELS survey and the orbital period of the system, we were more likely to miss periastron during a given orbit. Thus, we were more susceptible to rejecting the periastron points we did obtain as outliers, even though these points are where the spectral lines are most widely separated, and thereby where it is easiest to determine that the system is an SB2.

Finally, we concluded with a word of warning to RV surveys, since for a given resolution and cadence, there are a range of orbital parameters that can make a stellar-mass binary companion appear to be substellar. The lower the resolution or cadence, the greater the number of stellar binaries that can masquerade in a fashion similar to TYC 3010. Therefore, if other surveys can carefully monitor the widths of the CCF peaks for their targets (or monitor their line bisectors if they have high enough resolution), and when possible, focus their resources on observations of peripassage, then we hope that they will be able to avoid similar astrophysical false positives.

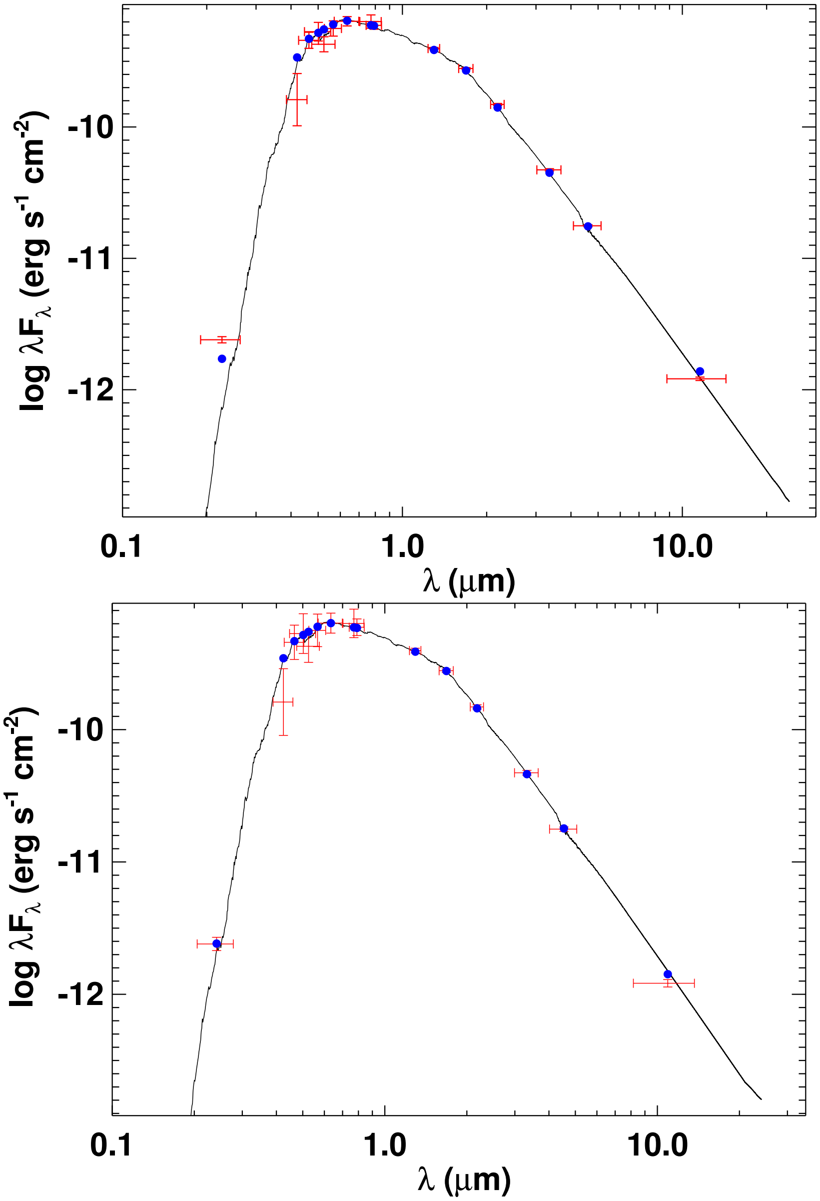

Figure 2.6: *Top:* A NextGen model atmosphere (solid line) fit to the observed broadband fluxes for TYC 3010 (assuming a single stellar component). The blue points are the flux values predicted by the model for the different bandpasses. The vertical red bars correspond to the uncertainties in the measured fluxes, while the horizontal red bars are the approximate widths of the bandpasses. This fit assumed that TYC 3010 was a single star, and found that $T_{\rm eff} = 5400 \pm 100$ K, $\log g = 4.5 \pm 0.5$, [Fe/H]$= 0.0 \pm 0.1$, and $A_V = 0.035 \pm 0.015$, yielding a distance of 162 ± 35 pc. *Bottom:* A second NextGen fit that uses two stellar components (corresponding to the primary and secondary stars of TYC 3010) with one of the components constrained to the spectroscopically determined stellar parameters for the primary ($T_{\rm eff} = 5589 \pm 148$ K, $\log g = 4.68 \pm 0.44$, [Fe/H]$= 0.09 \pm 0.20$). This fit estimates the secondary stellar parameters to be $T_{\rm eff} = 4600 \pm 850$ K, $R = 0.75 \pm 0.4\,R_\odot$, $\log g = 4.6 \pm 0.2$, and the distance to TYC 3010 to be 225 ± 40 pc, with an $A_V = 0.03 \pm 0.02$ (χ^2/dof$= 0.75$).

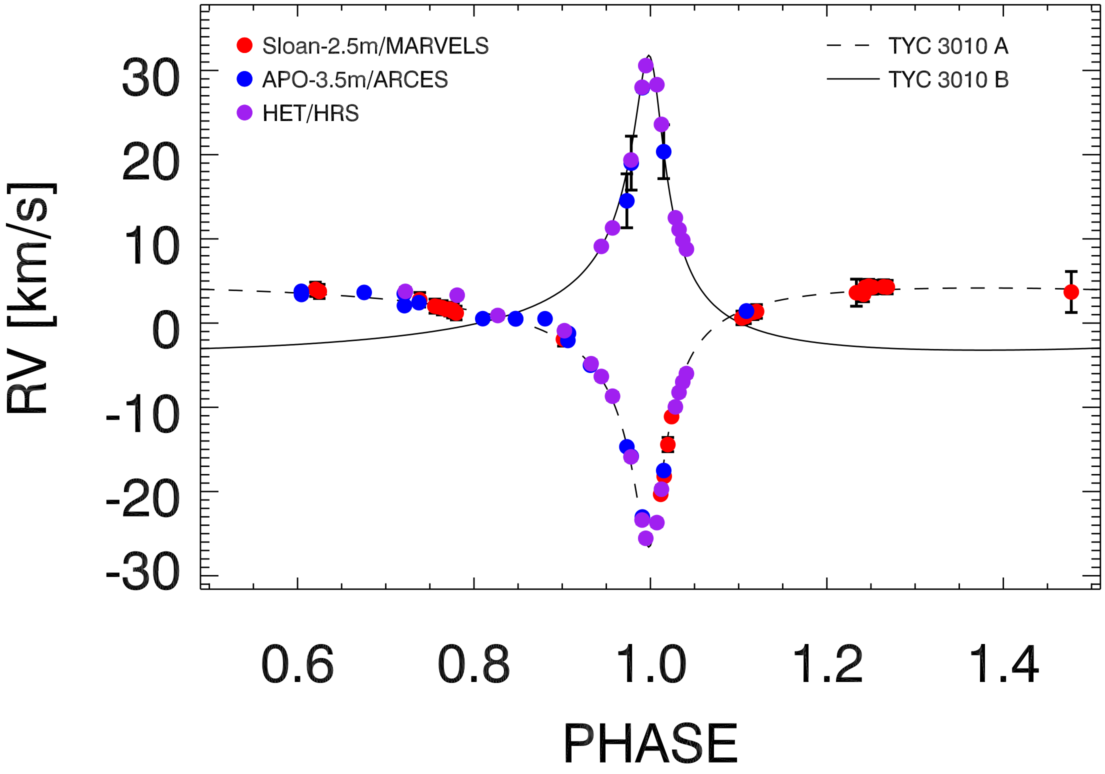

Figure 2.7: The correct phase-folded radial velocity curve for TYC 3010. The best-fit BINARY (Gudehus, 2001) orbital solution for the primary (dashed line) and secondary (solid line) are shown with the RVs obtained from the MARVELS (red), ARCES (blue), and HRS (purple) spectrographs. This solution corresponds to a period of ∼238 days, an eccentricity of ∼0.79, with K_1 ∼15.38 km s^{-1} and K_2 ∼17.50 km s^{-1}. Finally, for the RV points outside of periastron, it was necessary to de-blend the observed RVs with the method described in Section 2.4.2.1.

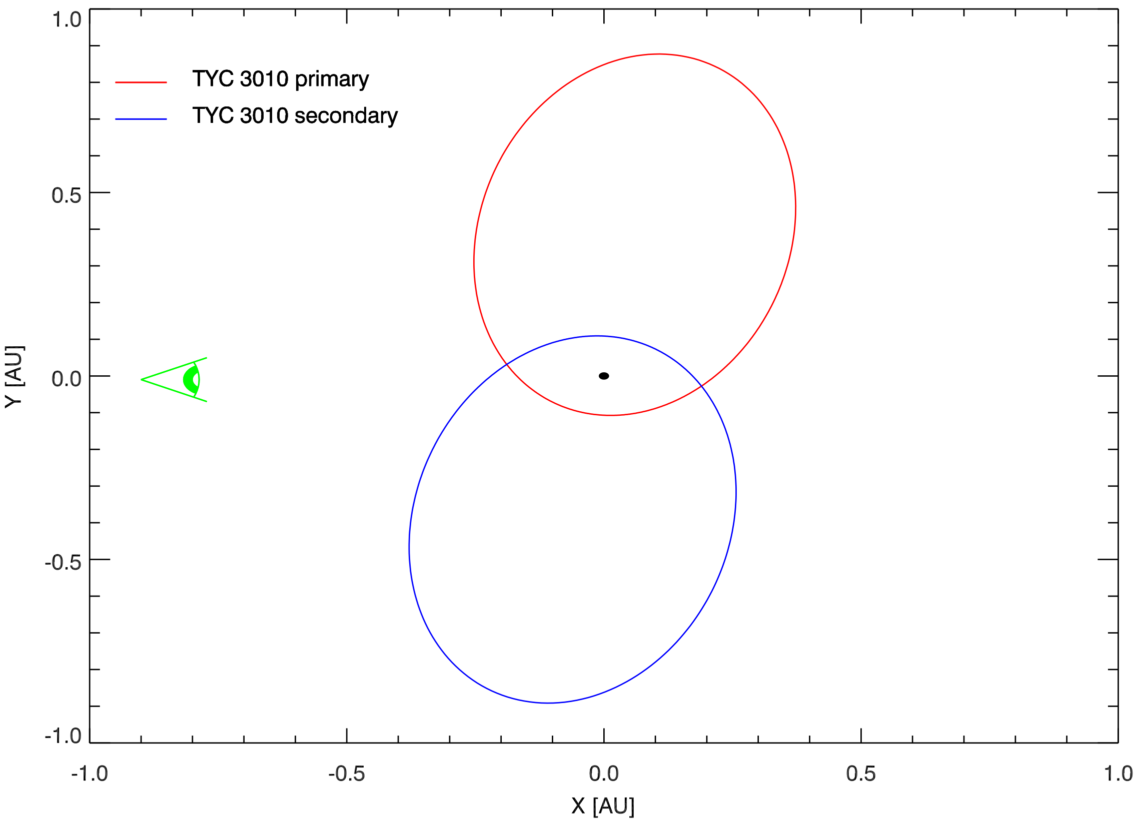

Figure 2.8: A schematic of the TYC 3010 system drawn to scale, showing the primary (red) and secondary (blue) orbits in the orbital plane. The position of the center of mass of the system is marked by the black point. Given the eccentricity ($e \sim 0.79$) and the fact that the semi-major axis is aligned nearly perpendicular to the line of sight ($\omega \sim 189°$), for a substantial fraction of the orbit the system can mimic the RV signal that would normally be induced by a secondary object with a minimum mass in the brown dwarf regime. Coupled with the relatively long period (∼238 days), depending on the frequency of the observations, it can be fairly easy to miss peripassage during a given orbit.

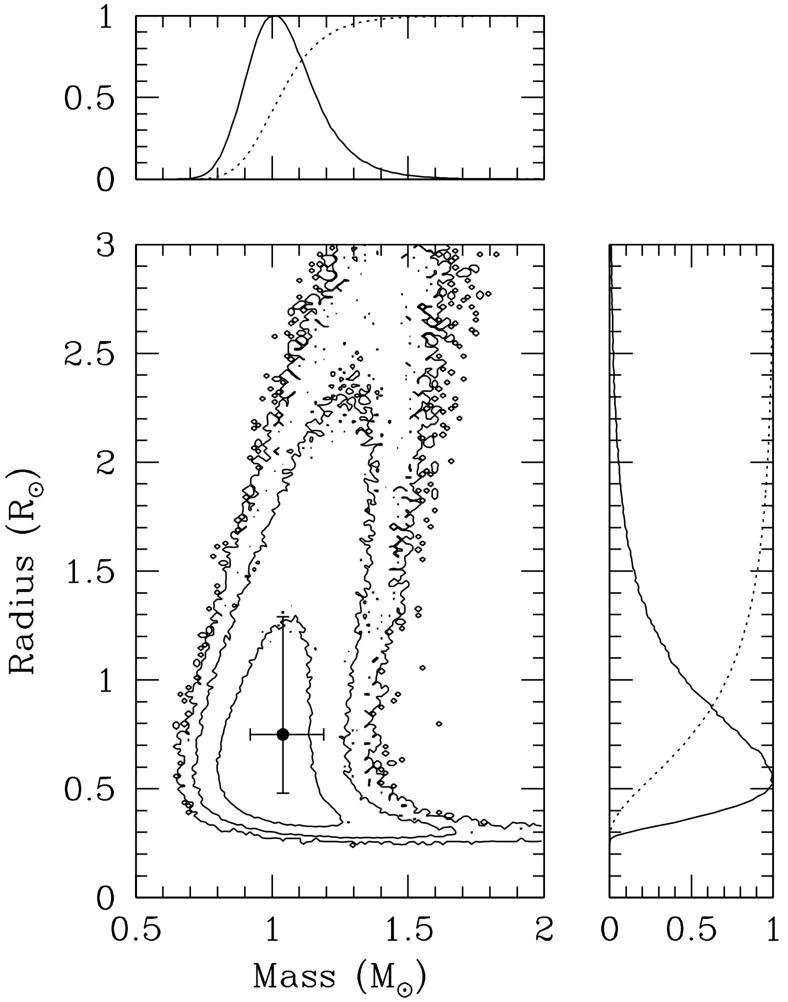

Figure 2.9: Mass and radius distributions for the primary component of TYC 3010. These distributions were determined by a set of MCMC trials with the spectroscopic stellar parameters and the empirical relations from Torres et al. (2010). The black point represents the median ($M_\star = 1.04^{+0.15}_{-0.12}\,M_\odot$, $R_\star = 0.75^{+0.54}_{-0.27}\,R_\odot$), and the error bars correspond to the 68.27% confidence intervals. The contours are lines of equal probability density which enclose 68%, 90%, and 95% of the cumulative probability relative to the maximum of the probability density. In the top and right panels, the probability distribution (solid line) and cumulative probability (dashed line) are shown for the mass and radius respectively.

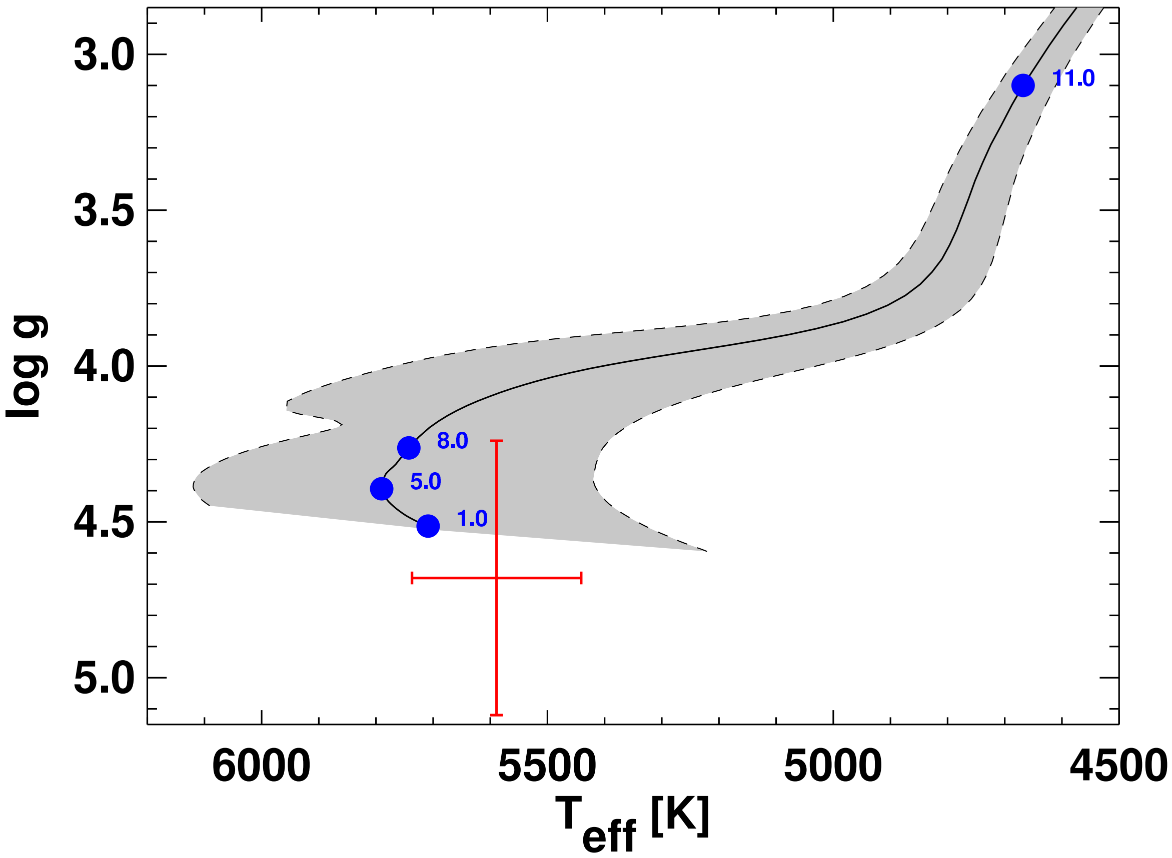

Figure 2.10: H–R diagram that compares the derived stellar parameters for the primary of TYC 3010 (red error bars) to a Yonsei-Yale stellar evolutionary track (solid curve; Demarque et al., 2004) for a star with a mass of 1.04 $M_\odot$ and [Fe/H]= 0.09. Ages (in Gyr) of 1.0, 5.0, 8.0, and 11.0 are represented by blue dots, and the 1σ deviations from the evolutionary track are shown in the shaded region.

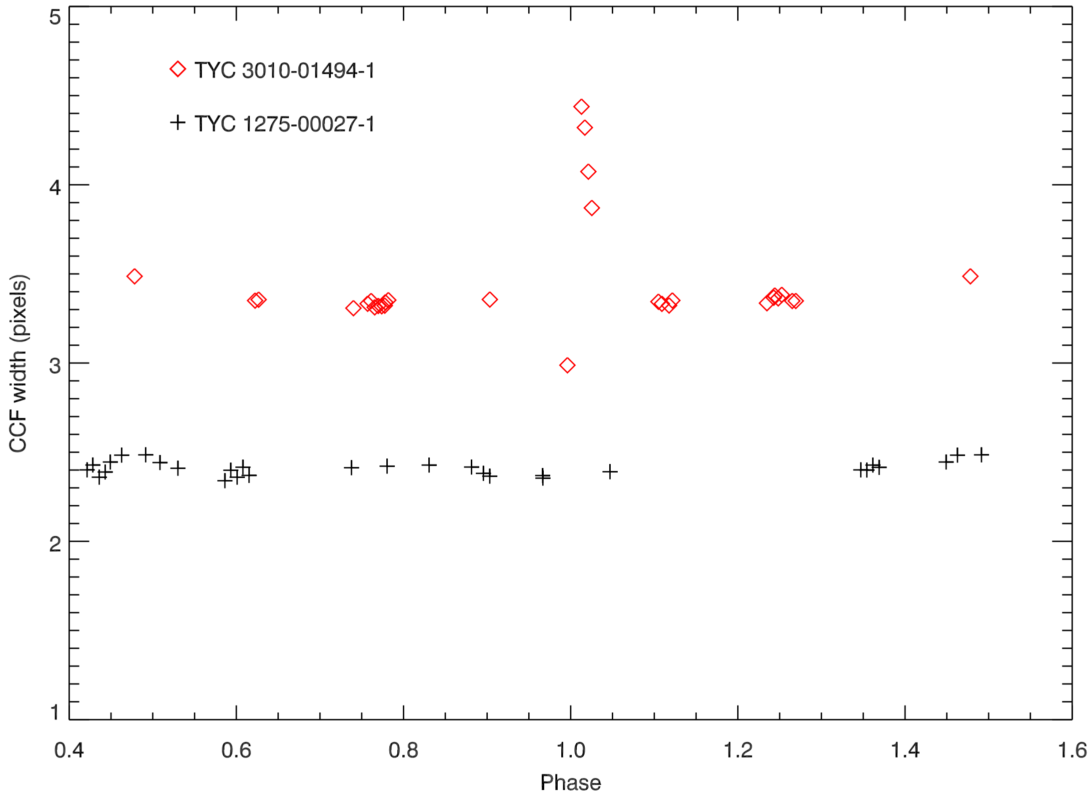

Figure 2.11: A comparison of how the width of the MARVELS CCF peak varies with phase for TYC 3010 (red) and another MARVELS candidate, TYC 1275-00027-1 (black). The MARVELS spectrograph does not possess the resolution to resolve two separate peaks in the CCF for TYC 3010, even at periastron. Instead the width of the CCF broadens dramatically, and upon inspection the peak appears asymmetric with a slight "shoulder" that suggests the presence of an unresolved secondary peak. This large variation in the peak width is not observed in TYC 1275-00027-1, which is known to be a single star. Therefore, by monitoring how the CCF peak changes with phase, and through visual inspection of the peaks, surveys can identify systems that are likely to be false positives like TYC 3010 during the candidate-vetting process. Finally, the median value of the CCF peak width is larger for TYC 3010 than the comparison star, but this may be due to either TYC 3010 rotating faster or the presence of the secondary peak. When confronted with a system whose peak is consistently broader than one might expect for a typical solar-type star, further investigation is necessary to determine if it is merely a fast rotator or if it has a stellar companion.

Chapter III

DETAILED ABUNDANCES OF PLANET-HOSTING WIDE BINARIES. I.
HD 20782+HD 20781

This chapter is based on work published in the Astrophysical Journal, 2014, Vol. 787, Article ID 98.

3.1 Abstract

Using high-resolution, high signal-to-noise echelle spectra obtained with Magellan/MIKE, we present a detailed chemical abundance analysis of both stars in the planet-hosting wide binary system HD 20782 + HD 20781. Both stars are G dwarfs, and presumably coeval, forming in the same molecular cloud. Therefore we expect that they should possess the same bulk metallicities. Furthermore, both stars also host giant planets on eccentric orbits with pericenters $\lesssim$0.2 AU. Here, we investigate if planets with such orbits could lead to the host stars ingesting material, which in turn may leave similar chemical imprints in their atmospheric abundances. We derived abundances of 15 elements spanning a range of condensation temperatures ($T_{\rm C} \approx$ 40–1660 K). The two stars are found to have a mean element-to-element abundance difference of 0.04 ± 0.07 dex, which is consistent with both stars having identical bulk metallicities. In addition, for both stars, the refractory elements ($T_{\rm C} >$ 900 K) exhibit a positive correlation between abundance (relative to solar) and $T_{\rm C}$, with similar slopes of $\approx 1\times10^{-4}$ dex K^{-1}. The measured positive correlations are not perfect;

both stars exhibit a scatter of $\approx 5\times10^{-5}$ dex K^{-1} about the mean trend, and certain elements (Na, Al, Sc) are similarly deviant in both stars. These findings are discussed in the context of models for giant planet migration that predict the accretion of H-depleted rocky material by the host star. We show that a simple simulation of a solar-type star accreting material with Earth-like composition predicts a positive—but imperfect—correlation between refractory elemental abundances and $T_{\rm C}$. Our measured slopes are consistent with what is predicted for the ingestion of 10–20 Earths by each star in the system. In addition, the specific element-by-element scatter might be used to distinguish between planetary accretion and Galactic chemical evolution scenarios.

3.2 Introduction

Exoplanet surveys like NASA's *Kepler* mission are discovering planets in a variety of environments, e.g., systems with multiple stellar components, which suggests that planet formation mechanisms are remarkably robust. An important result in attempts to understand these planet formation mechanisms is that giant planets are found to be more prevalent around solar-type stars that are typically enriched in metals by ~0.15 dex relative to similar stars that have no detected giant planets (e.g., Fischer & Valenti, 2005; Ghezzi et al., 2010). This evidence indicates that giant planet formation is most successful in metal-rich environments.

Beyond overall metallicity, investigations of abundance patterns in elements besides Fe in planet-hosting stars have uncovered evidence that planet hosts may be enriched or depleted (relative to the Sun) with elements of high condensation temperatures ($T_{\rm C} \gtrsim 900$ K, i.e., the refractory elements that are the major components of rocky planets) depending on the architecture and evolution of the their planetary systems. There are at least two planet formation processes that may alter stellar surface abundances: (1) the accretion of hydrogen-depleted rocky material (Gonzalez, 1997), which would result in the *enrichment* of the stellar atmosphere, and (2) H-depleted rocky material in terrestrial planets may be withheld from the star during their formation, which would result in the *depletion* of heavy elements relative to H in the stellar atmosphere (Meléndez et al., 2009). For the enrichment scenario, Schuler et al. (2011a) suggest that stars with close-in giant planets (∼0.05 AU) may be more enriched with elements of high condensation temperature ($T_{\rm C}$). This is thought to be a result of giant planets which form in the outer planetary system migrating inward to their present close-in positions. As they migrate, they can push rocky material into the host star (e.g., Ida & Lin, 2008; Raymond et al., 2011). For the depletion scenario, Meléndez et al. (2009) and Ramírez et al. (2009) propose that the depletion of refractory elements in Sun-like stars may correlate with the presence of terrestrial planets. Certainly there are processes other than planet formation that may alter stellar atmospheric abundances, but these effects can be mitigated by simultaneously considering a pair of stars that have experienced essentially the same evolution and environments over the course of their lives, such as stars in wide binaries.

Indeed, wide stellar binaries known to harbor planets are valuable laboratories for studying the connection between how planets form and the chemical compositions of their host stars. Since most binary stars are believed to have formed coevally from a common molecular cloud (Kratter, 2011, and references therein), planet-hosting wide binaries are particularly valuable, because both stars can be presumed to have the same age and initial composition. In fact, Desidera et al. (2004, 2006) studied the differential Fe abundances for a set of 50 wide binaries. They found that only one binary pair possessed a Δ[Fe/H] > 0.09 dex, while for the majority of the systems they found Δ[Fe/H] < 0.03 dex. Thus, for components of wide binaries where at least one star possesses a planet, it is reasonable to expect that any significant difference in their present-day chemical abundances is most likely due to some aspect of the planet formation process.

For example, the investigation by Schuler et al. (2011b) of 16 Cyg (a triple system that includes a wide binary pair of two nearly identical stars, plus the secondary hosts a giant planet at $\sim$1.7 AU while the primary does not) found that 16 Cyg A and 16 Cyg B were chemically identical (However, we should note that Ramírez et al. (2011) found that 16 Cyg A is more metal rich than 16 Cyg B by 0.041 ± 0.007 dex, but Metcalfe et al. (2012) found that the two stars are chemically identical). The authors speculated that one possible reason 16 Cyg B formed a giant planet, while 16 Cyg A may not have, is because 16 Cyg A itself has a resolved M dwarf companion (the tertiary in the system). This third star may have truncated the primary's circumstellar disk and inhibited planet formation (e.g., Jensen et al., 1996; Mayer et al., 2005). Since the two stars must be the same age, and in addition they were found to be chemically identical, the authors were forced to consider the properties of the system described above, which could have led to these two stellar twins failing to form planetary systems with similar architectures. The 16 Cyg wide binary was an ideal first system for this kind of comparison study, because the component stars have almost identical physical properties, i.e., their masses are nearly equal. This minimizes systematic errors that may arise from analyzing two stars with drastically different basic stellar properties (Schuler et al., 2011b).

Ascertaining how planet formation may influence the composition of host star atmospheres could revolutionize target selection for future exoplanet surveys. If chemical abundance patterns can identify a star as a planet host, then a single high-resolution spectrum—instead of solely relying on large, time-intensive monitoring surveys—will permit selection of probable planet hosts among nearby stars in our Galaxy. Furthermore, if particular chemical signatures indicate the existence of specific kinds of planets, such as terrestrial planets, considerably more targeted searches for Solar System analogs would be possible.

The goal of this series of papers is to study the interplay between planet formation and the chemical composition of the host star by directly comparing the chemical abundances of each stellar pair in planet-hosting wide binaries. This paper presents the analysis of detailed abundance trends in the two stars comprising the HD 20782/81 system. HD 20782 and HD 20781 are a common proper motion wide binary with an angular separation of 252″ and a projected physical separation of $\sim 9,000$ AU (Desidera & Barbieri, 2007; Mugrauer & Neuhäuser, 2009). They are both solar-type stars with spectral types of G1.5V and G9.5V, and apparent V magnitudes of 7.36 and 8.48, respectively (Gray et al., 2006).

For HD 20782/81 we present the investigation of the only known binary system where both stars have detected planets. HD 20782 has a Jupiter-mass planet on a very eccentric ($e \sim 0.97$) orbit at ∼1.4 AU (Jones et al., 2006), and HD 20781 hosts two moderately eccentric ($e \sim 0.1 - 0.3$) Neptune-mass planets within ∼0.3 AU (M. Mayor 2013, private communication). Therefore, *if* the formation and evolution of planetary systems with different architectures affect the host star composition in distinct ways, studying systems like HD 20782/81 allows us to discern which aspects of their architectures play the most important roles.

In Section 3.3, we describe our observations, reductions, and spectral analysis. In Section 3.4, we summarize the main results, including the finding that both stars in HD 20782/81 exhibit similar positive trends between refractory elemental abundance and T_{C}. In Section 3.5, we discuss the results in the context of previous studies and a simple calculation that predicts how the accretion of Earth-like rocky planets would affect refractory elemental abundances as a function of T_{C}. We find that the observed trends between refractory elemental abundance and T_{C}, and the element-by-element scatter relative to the mean trends, are consistent with the ingestion by both stars of 10–20 Earths. Finally, in Section 3.6 we highlight our main conclusions.

3.3 Data and Analysis

For both HD 20782/81, on UT 2012 Feb 08 we obtained high-resolution, high-signal-to-noise ratio (SNR) spectra with the 6.5-m Magellan II (Clay) telescope (Shectman & Johns, 2003) and MIKE echelle spectrograph (Bernstein et al., 2003). The spectra covered a wavelength range from $\sim 3500 - 9500$Å. Three exposures were taken of both HD 20782

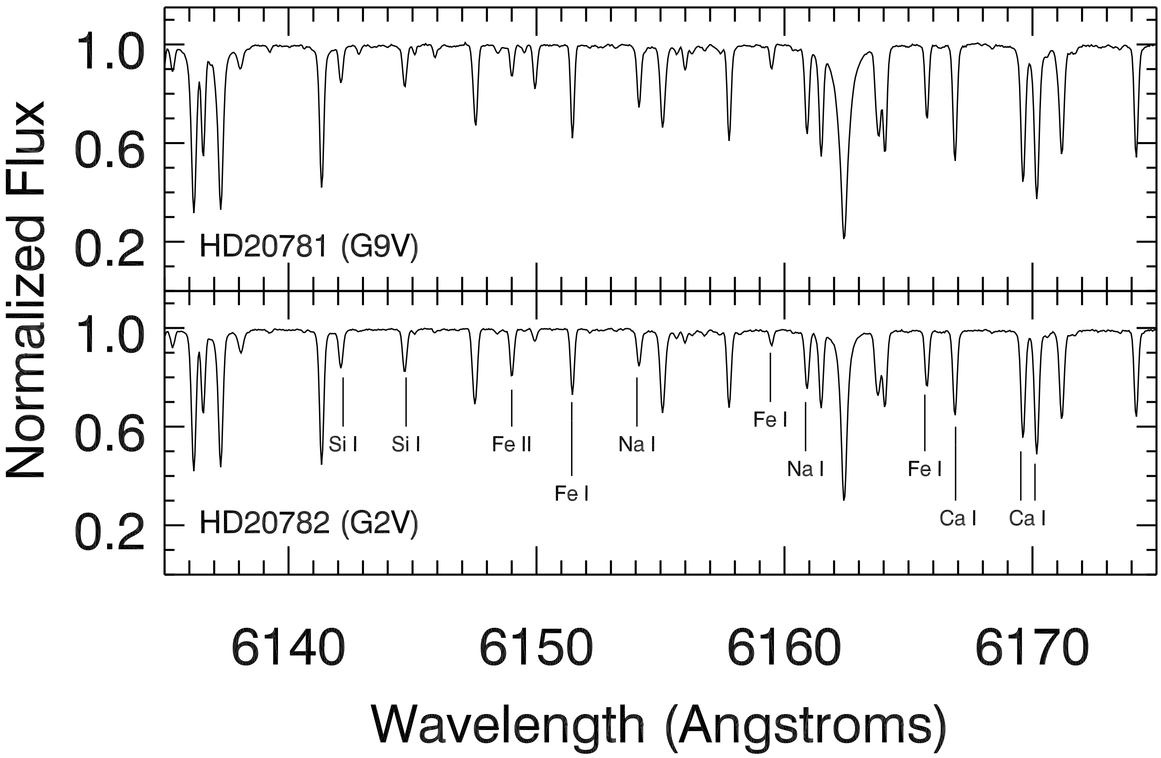

Figure 3.1: Sample Magellan/MIKE spectra for HD 20782/81, spanning the wavelength range from $\lambda 6135 - \lambda 6175$.

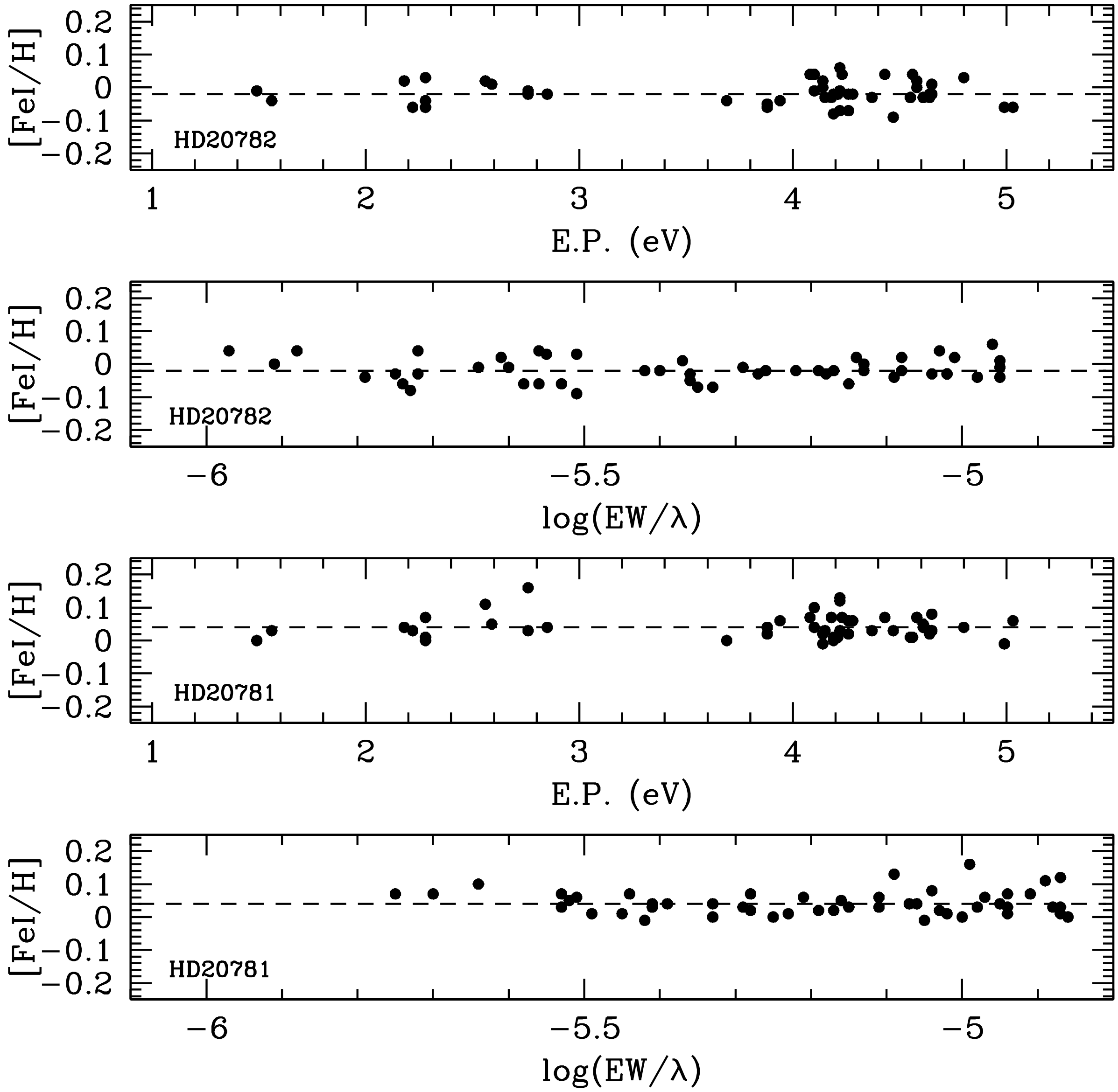

Figure 3.2: Plots of [FeI/H] vs excitation potential and reduced equivalent width for both HD 20782/81. The dashed lines indicate the mean values of [FeI/H], which are −0.02 dex and +0.04 dex for HD 20782 and HD 20781, respectively.

and HD 20781, with a total integration time of 540s for HD 20782 and 1200s for HD 20781. Multiple bias frames and flat field exposures were taken at the beginning of the night. A Thorium-Argon lamp exposure was taken at the beginning and end of the night for wavelength calibration. The data were reduced using standard IRAF routines.

The final reduced spectra possess a resolution of $R = \lambda/\Delta\lambda \sim 40,000$ and SNR in the continuum region near λ6700 of ~600 for HD 20781 and ~620 for HD 20782. Sample spectra spanning the wavelength region λ6135-λ6175 are shown in Figure 3.1. A solar spectrum (sky) was also obtained for derivation of relative abundances, and has an SNR of ~610 near λ6700.

In each star, abundances of 15 elements have been derived from the observed spectra. The 2010 version of the LTE spectral analysis package MOOG (Sneden, 1973) was used to perform the spectral analysis. The abundances were derived from measurements of the equivalent widths (EWs) of atomic lines using the SPECTRE analysis package (Fitzpatrick & Sneden, 1987). We adopted our line list from Schuler et al. (2011a). Stellar parameters were obtained by requiring excitation and ionization balance of the Fe I and Fe II lines in the standard way. Plots of [FeI/H] vs. excitation potential and reduced equivalent width are provided in Figure 3.2, which shows that the correlations are zero as required. The atomic excitation energies (χ) and transition probabilities ($\log \mathrm{gf}$) were taken from the Vienna Atomic Line Database (VALD; Piskunov et al., 1995; Kupka et al., 1999). For each element, the abundances were determined relative to solar via a line-by-line differential analysis.

Carbon abundances are also derived with the *synth* driver in MOOG to synthetically fit

Table III.1. HD 20782/81: Stellar Parameters & Abundances

	HD 20782	HD 20781
T_{eff} (K)	5789 ± 38	5324 ± 52
$\log g$ (cgs)	4.41 ± 0.12	4.51 ± 0.10
ξ (km s^{-1})	1.32 ± 0.10	1.02 ± 0.11
[C/H][a]	-0.07 ± 0.03[b] ± 0.04[c]	$-0.09 \pm 0.03 \pm 0.04$
[O/H]	$+0.04 \pm 0.01 \pm 0.05$	$-0.08 \pm 0.04 \pm 0.07$
[Na/H] . . .	$-0.08 \pm 0.02 \pm 0.03$	$-0.06 \pm 0.03 \pm 0.05$
[Mg/H] . .	$+0.04 \pm 0.01 \pm 0.06$	$+0.10 \pm 0.00 \pm 0.05$
[Al/H] . . .	$-0.01 \pm 0.00 \pm 0.02$	$+0.04 \pm 0.00 \pm 0.03$
[Si/H]	$-0.02 \pm 0.01 \pm 0.02$	$-0.01 \pm 0.01 \pm 0.02$
[Ca/H] . . .	$+0.04 \pm 0.01 \pm 0.05$	$+0.06 \pm 0.03 \pm 0.06$
[Sc/H] . . .	$-0.03 \pm 0.02 \pm 0.06$	$+0.04 \pm 0.02 \pm 0.05$
[Ti/H] . . .	$+0.06 \pm 0.01 \pm 0.05$	$+0.12 \pm 0.02 \pm 0.06$
[V/H]	$-0.01 \pm 0.01 \pm 0.04$	$+0.10 \pm 0.02 \pm 0.07$
[Cr/H] . . .	$-0.05 \pm 0.01 \pm 0.03$	$+0.03 \pm 0.02 \pm 0.05$
[Mn/H] . .	$-0.01 \pm 0.06 \pm 0.07$	$+0.04 \pm 0.05 \pm 0.07$
[Fe/H] . . .	$-0.02 \pm 0.01 \pm 0.02$	$+0.04 \pm 0.01 \pm 0.03$
[Co/H] . . .	$-0.05 \pm 0.01 \pm 0.03$	$+0.03 \pm 0.01 \pm 0.04$
[Ni/H] . . .	$-0.02 \pm 0.01 \pm 0.03$	$+0.01 \pm 0.01 \pm 0.03$

[a] Adopted solar parameters: $T_{\mathrm{eff}} = 5777$ K, $\log g = 4.44$, and $\xi = 1.38$ km s^{-1}.

[b] $\sigma_{\mu} = \sigma/\sqrt{N-1}$, where σ is the standard deviation and N is the number of lines measured for a given element.

[c] $\sigma_{Total}-$ quadratic sum of σ_{μ} and uncertainties in the elemental abundance resulting from uncertainties in T_{eff}, $\log g$, and ξ.

Table III.2. HD 20782/81: Lines Measured, Equivalent Widths, and Abundances

	λ	χ					HD 20782			HD 20781		
Element	(Å)	(eV)	log gf	EW$_\odot$	$\log N_\odot$	$\log N_{\odot,\mathrm{synth}}$[a]	EW	$\log N$	$\log N_{\mathrm{synth}}$	EW	$\log N$	$\log N_{\mathrm{synth}}$
C I	5052.17	7.68	-1.304	36.2	8.51	···	36.1	8.50	···	17.2	8.35	···
C2	5086	···	···	···	···	8.43	···	···	8.32	···	···	8.35
C2	5135	···	···	···	···	8.44	···	···	8.36	···	···	8.43
C I	5380.34	7.68	-1.615	22.8	8.54	···	20.8	8.47	···	10.9	8.44	···
O I	6300.30	0.00	-9.717	5.5	8.69	···	6.3	8.72	···	6.5	8.52	···
O I	7771.94	9.15	0.369	65.6	8.77	···	71.2	8.84	···	34.7	8.71	···
O I	7774.17	9.15	0.223	57.8	8.79	···	60.5	8.82	···	30.4	8.74	···
O I	7775.39	9.15	0.001	46.5	8.80	···	47.5	8.81	···	23.1	8.75	···
Na I	5682.63	2.10	-0.700	119.9	6.52	···	107.9	6.41	···	135.1	6.41	···
Na I	6154.23	2.10	-1.560	38.2	6.31	···	33.2	6.23	···	49.2	6.23	···
Na I	6160.75	2.10	-1.260	58.1	6.31	···	53.9	6.26	···	76.4	6.31	···
Mg I	5711.09	4.35	-1.833	100.8	7.56	···	102.0	7.59	···	128.3	7.66	···
Mg I	6841.19	5.75	-1.610	64.1	7.85	···	66.0	7.89	···	74.6	8.14[b]	···
Al I	6696.02	3.14	-1.347	36.7	6.24	···	34.9	6.23	···	52.7	6.28	···
Al I	6698.67	3.14	-1.647	20.7	6.21	···	19.8	6.20	···	32.6	6.25	···

[a] Indicates the $\log N$ abundance determined from the synthetic fit to a given line.

[b] The $\log N$ abundance for this line was rejected as spurious, as described in paragraph 4 of Section 3.3.

Note. — This table is published in the appendix. A portion is shown here for guidance regarding its form and content.

the C_2 features at $\lambda5086$ and $\lambda5135$. Oxygen abundances were determined with the MOOG *blends* driver for the forbidden line at $\lambda6300$, and EW measurements of the near-infrared triplet at $\lambda7771$, $\lambda7774$, and $\lambda7775$. Also, we suspect that the Mg I line at $\lambda6841.19$ is blended with a line that becomes stronger in stars with $T_{\rm eff} \lesssim 5400$ K, and thus we rejected the Mg abundance it yielded for HD 20781 as spurious.

For the odd-Z elements V, Mn, and Co, the abundances of which can be overestimated due to hyper-fine structure (hfs) effects (Prochaska & McWilliam, 2000), spectral synthesis incorporating hfs components has been used to verify the EW-based results. The hfs components for these elements were obtained from Johnson et al. (2006), and the line lists for wavelength regions encompassing each feature were taken from VALD. The adopted V, Mn, and Co abundances are derived from the hfs analysis and those lines with EWs that were not significantly altered by hfs.

The abundance and error analyses for all elements are described in detail in Schuler et al. (2011a). The stellar abundances (relative to the solar abundances derived from the solar spectrum), parameters, and uncertainties for HD 20782/81 are summarized in Table III.1. The adopted line list, EWs, and line-by-line abundances of each element for HD 20782/81 and the Sun are given in Table III.2.

3.4 Results

As shown in Table III.1, the stellar parameters we determined for HD 20782/81 are consistent with the primary being a ~G2V and the secondary being a ~G9.5V. The differences in parameters (in the sense of primary minus secondary) are : $\Delta T_{\mathrm{eff}} = +465 \pm 64$ K, $\Delta \log g = -0.10 \pm 0.16$ dex, and $\Delta\xi = +0.30 \pm 0.15$ km s^{-1}. Furthermore, according to the PASTEL catalogue of stellar parameters (Soubiran et al., 2010), the mean literature values for the stellar parameters of HD 20782 ($T_{\mathrm{eff}} \sim$ 5800 K, $\log g \sim 4.4$ dex, and [Fe/H] ~ -0.06 dex) are in good agreement with ours. For HD 20781, our values agree with the mean literature values for T_{eff} ($\sim$5300 K) and $\log g$ ($\sim$4.4 dex), but there is a considerable spread of $\sim$0.2 dex (-0.18—$+0.01$ dex) in the published [Fe/H] values for this star. The upper end of this range is consistent with the value of [Fe/H] that we derive for HD 20781. The abundances of the 15 individual elements are shown graphically in Figure 3.3. The abundance differences shown in Figure 3.3 are the means of the line-by-line differences for each element. The mean abundance difference is 0.04 ± 0.07 dex, as expected for coeval stars in a binary system.

The abundances of HD 20782/81 are shown versus T_{C} in Figures 3.4 and 3.5. The condensation temperatures were taken from the 50% T_{C} values derived by Lodders (2003). Only the refractory elements ($T_{\mathrm{C}} \gtrsim$ 900 K) are displayed, because it is among these elements that the chemical signature of planet formation has been shown to be strongest (Meléndez et al., 2009). We performed both unweighted and weighted linear fits to the [X/H] versus T_{C} abundance relations to investigate possible correlations. For our analysis and discussion, we adopt the *weighted* fits. However, in Figure 3.4, we provide the unweighted fits for comparisons to previous studies that only reported unweighted fits.

As can be seen in Figures 3.4-3.5, the slopes of the unweighted linear least-squares fits are: $m_{82} = (10.59 \pm 5.17) \times 10^{-5}$ dex K^{-1} and $m_{81} = (14.55 \pm 5.94) \times 10^{-5}$ dex K^{-1} for HD 20782 and HD 20781 respectively. The slopes of the weighted linear least-squares fits are: $m_{82} = (9.71 \pm 4.57) \times 10^{-5}$ dex K^{-1} and $m_{81} = (13.60 \pm 6.57) \times 10^{-5}$ dex K^{-1} for HD 20782 and HD 20781 respectively. Thus the correlation between refractory elemental abundance and T_{C} is not perfect, with individual elements exhibiting scatter relative to the mean trend. Nonetheless, the slopes of the weighted linear fits to refractory abundances vs T_{C} are modestly statistically significant ($\sim 2\sigma$). In addition, both a Pearson's r and a Kendall's τ correlation test indicate that the abundances and T_{C} are correlated at $> 90\%$ confidence for both stars (Pearson r confidence of 97% for HD 20781 and 92% for HD 20782).

In the discussion that follows, we consider this result in the context of a model to predict the degree to which we might expect a modest correlation between abundance and T_{C} from host stars that have ingested a small amount of rocky planetary material.

3.5 Discussion

3.5.1 How well correlated are abundance and T_{C} expected to be?

To estimate the impact that the accretion of a rocky planet would have on the atmospheric composition of a solar-type star, we simulated the accretion of a massive body with Earth-like composition onto the Sun. Since Jupiter and Saturn are predominantly composed of H and He with approximately solar H/He ratios (Young, 2003; Lissauer & Stevenson, 2007), the chemical composition of a gas giant planet is likely to be fairly similar to the protoplanetary

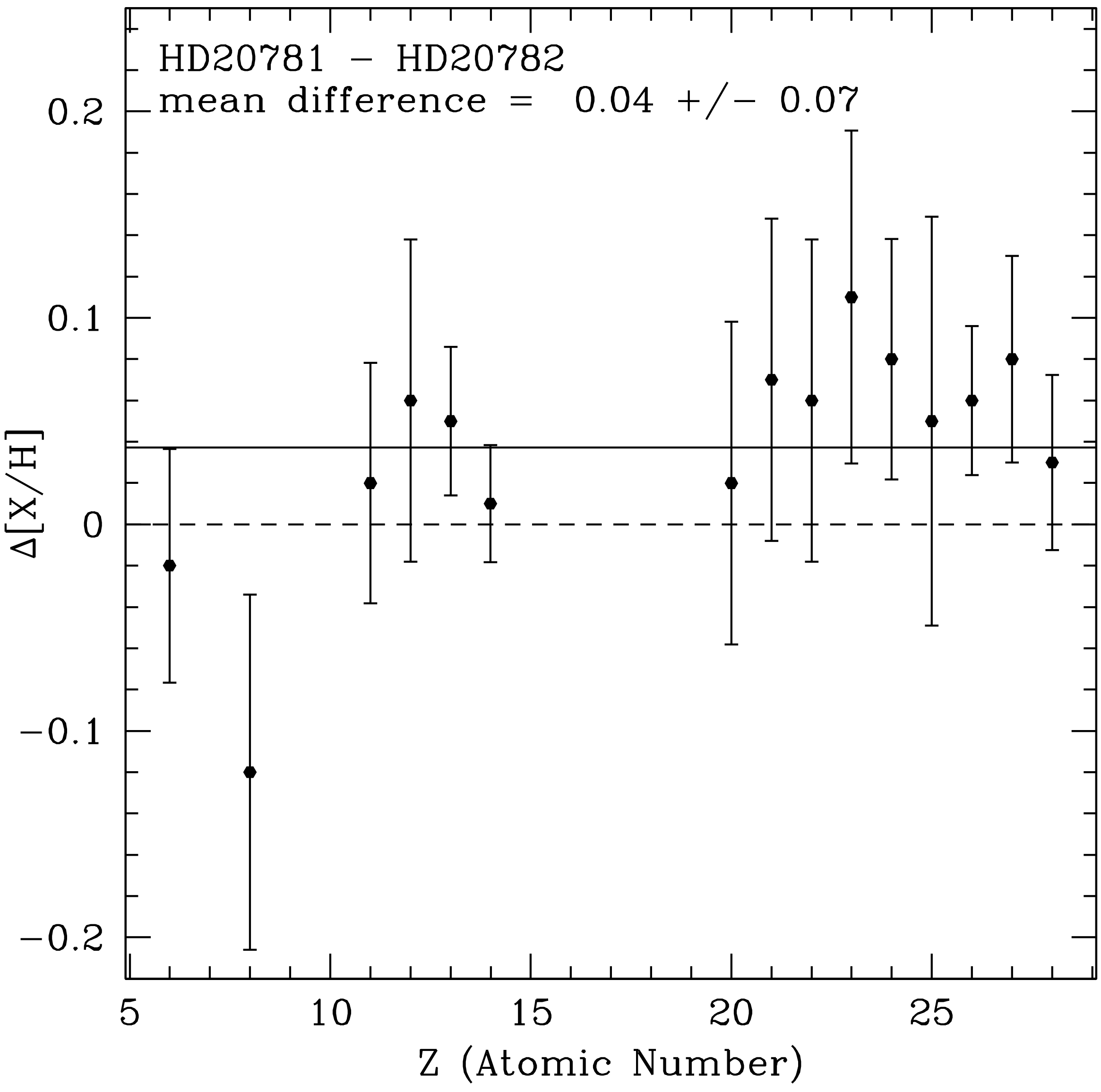

Figure 3.3: Differential abundances for HD 20782/81 as a function of atomic number (Z). The solid line represents the mean difference of 0.04 ± 0.07 dex, and the dashed line is meant to guide the eye at 0.0 dex.

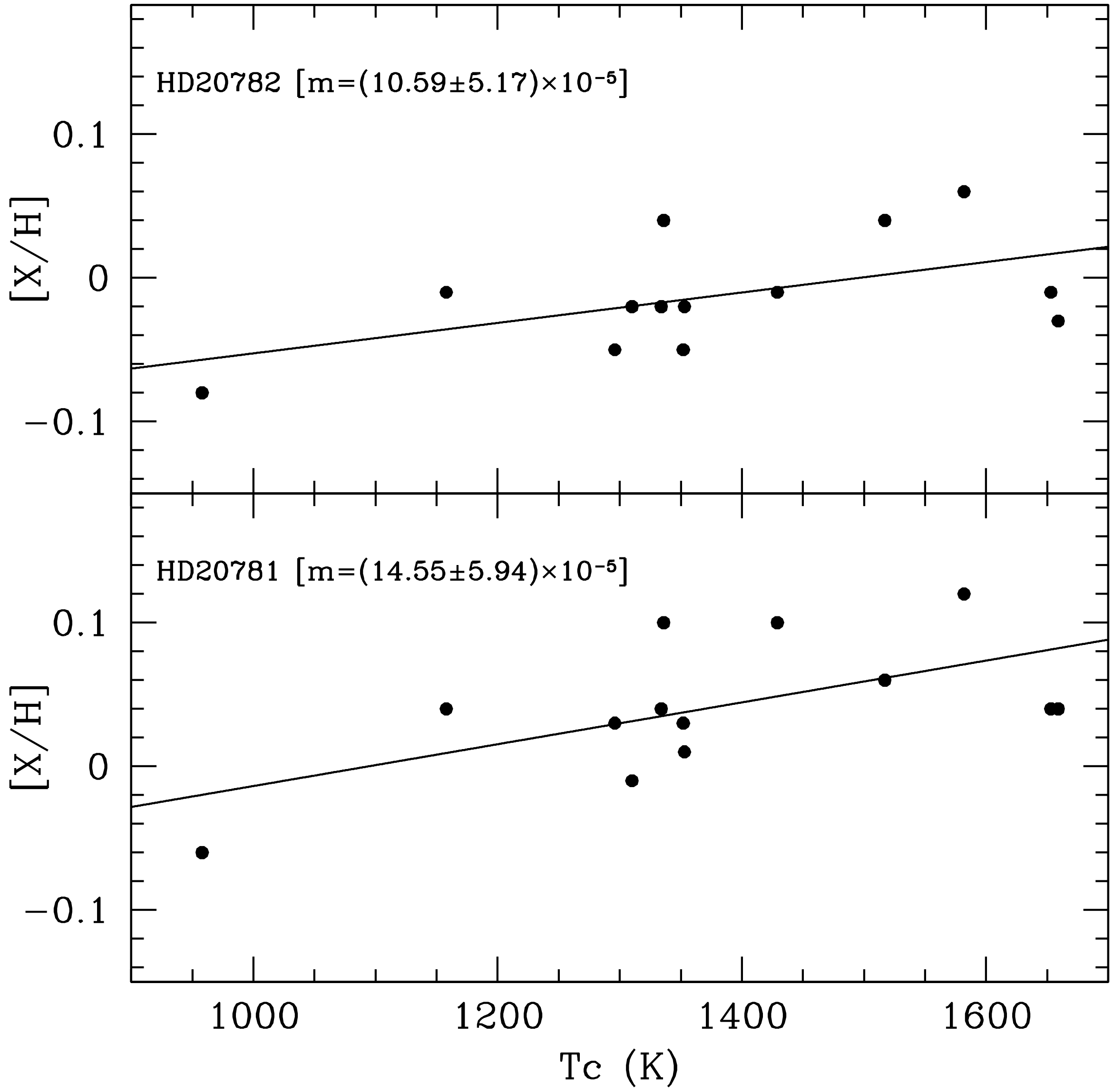

Figure 3.4: *Unweighted* linear fits to abundance vs. condensation temperature (T_C) for HD 20782/81.

disk, and thereby to the host star. The accretion of gas giant planets, therefore, would be unlikely to produce the refractory element versus T_{C} correlation observed in some planet hosts. Such trends would be expected to arise only from the accretion of H-depleted rocky material.

To perform our calculation of the expected trend between refractory elemental abundance and T_{C}, we begin by considering what would happen to the refractory abundances of the Sun if it accreted a certain multiple of $M_{\oplus}$ of refractory material with a composition similar to the Earth. Since the metallicities of HD 20782/81 are consistent with solar (all elemental abundances are within ~0.1 dex of their solar values) it is reasonable to assume that the primordial abundances of both stars were similar to the present-day solar abundances. We use the values of McDonough (2001) to obtain the mass fraction for each element in the Earth. With the mass of the Earth, and the molar mass for each element, we can determine an absolute number of atoms for each element. Then we add this amount of each element into the solar convection zone and see how the abundances change. Given the mass of the Sun, the mass fraction of hydrogen, and the fact that at 30 Myr (by which time gas should have dissipated from the protoplanetary disk, and only fully formed planets and a debris disk remain) the convection zone was 3% of the Sun's mass (Sackmann et al., 1993), we can determine the amount of hydrogen in the Sun's convection zone at that time. Using the solar abundances listed in Asplund et al. (2009), the photospheric abundance of each element relative to hydrogen can be determined. Thus, the change in the abundance of each element due to the accretion of a certain multiple of $M_{\oplus}$ of Earth-like rocky material can be calculated.

Through the order-of-magnitude calculation described above, we derived the values for the [X/H]-$T_{\rm C}$ slopes in each of the accretion scenarios shown in Figure 3.6. For example, if a solar-type star were to accrete $5M_{\oplus}$of material with a chemical composition similar to the Earth, then from our calculation we would expect a trend with $T_{\rm C}$ among the refractories that corresponds to a slope of $(5.42 \pm 1.62) \times 10^5$ dex $\rm K^{-1}$ (Figure 3.6). Furthermore, as a result of our simulation of a Sun-like star accreting Earth-like planets, we would *not* expect a perfect correlation between abundance and $T_{\rm C}$. There is some scatter about the linear fit to the simulated data, as shown in Figure 3.6. Indeed, some of the elements deviate in a similar manner from the linear fit in both the observed and modeled data. For example, in Figures 3.4−3.6, the elements Na ($T_{\rm C}$ ~960 K), Al ($T_{\rm C}$ ~1653 K), and Sc ($T_{\rm C}$ ~1659 K) are consistently below the fits to both the simulated and observed data. Since these elements are similarly scattered about the fit in both the model and the observations, the scatter in the observed correlation may not solely be the result of observational noise.

There are several ways to extend the above calculation, for example, to take into account differences in the mass of the star, the mass-dependence of the size of the convection zone, and possible variations in the composition of the planets accreted by the star. Such additional considerations could perhaps explain additional scatter in the observed abundances. Here our intent is to illustrate the sense and magnitude of the effect. However, given that $\Delta T_{\rm eff} = +465 \pm 64$ K for HD 20782/81, we investigated how differences in the depths of their convection zones would affect the results of our simple model. Using Figure 1 from

Pinsonneault et al. (2001), which provides a relationship between $T_{\rm eff}$ and the mass of the convection zone, we estimate that for a star like HD 20781 ($T_{\rm eff}\sim$ 5300 K) the mass of the convection zone is at most $\sim 0.05 M_\odot$. Using the empirical relationships described in Torres et al. (2010)—which yield the mass and radius of a star as functions of the spectroscopic stellar parameters—we can estimate the mass of HD 20781 to be $\sim 0.9 M_\odot$. This means that about 6% of the mass of HD 20781 is in the convection zone (as opposed to ~3% for stars with masses similar to the Sun). Thus, while our simulation shows that the ingestion of $10 M_\oplus$ of Earth-like material would produce the measured slope for HD 20782, about twice as much material is required to produce the measured slope for HD 20781(Figure 3.6).

3.5.2 Interpretation of the positive slopes for HD 20782 and HD 20781

The positive trends with $T_{\rm C}$ seen among the refractory elemental abundances of HD 20782/81 may be due to the presence of eccentric giant planets that have migrated to orbits within ~1 AU. HD 20782 hosts a very eccentric Jupiter at 1.4 AU, with a pericenter of $a(1-e) = 1.4(1-0.97) \sim 0.04$ AU. HD 20781 possesses two close-in Neptunes at 0.2 and 0.3 AU. These giant planets could have pushed refractory-rich planetary material into their host stars as they migrated inward to their current orbits. We have shown in Section 3.5.1 that compared to a simple model of a solar-type star accreting Earth-like material, both HD 20782/81 have slopes that are consistent with the ingestion of $10-20 M_\oplus$ of rocky material.

Several studies have performed simulations of giant planet migration that result in a substantial amount of hydrogen-depleted material falling into the star (e.g., Ida & Lin, 2008;

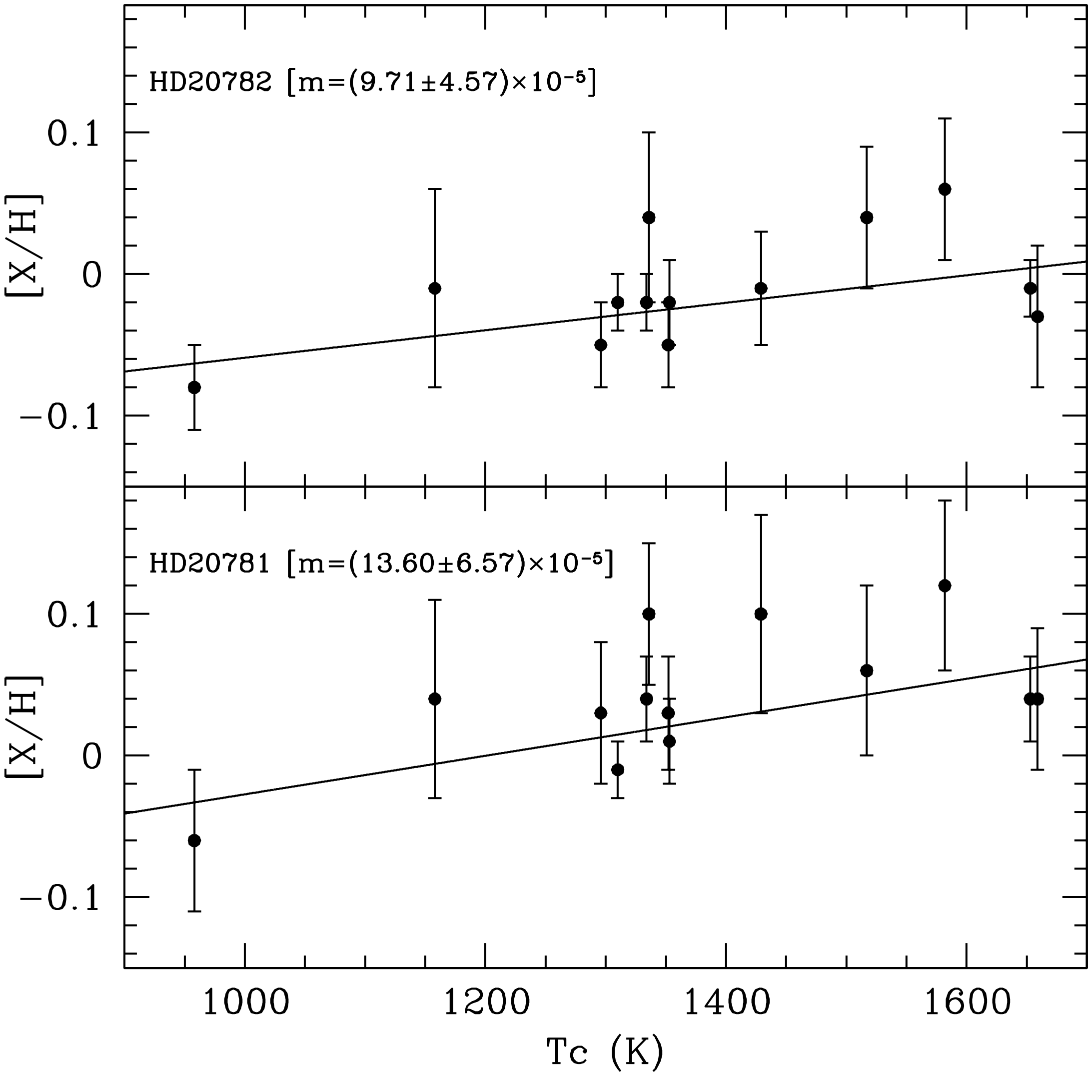

Figure 3.5: *Weighted* linear fits to abundances vs. condensation temperature ($T_{\rm C}$) for HD 20782/81.

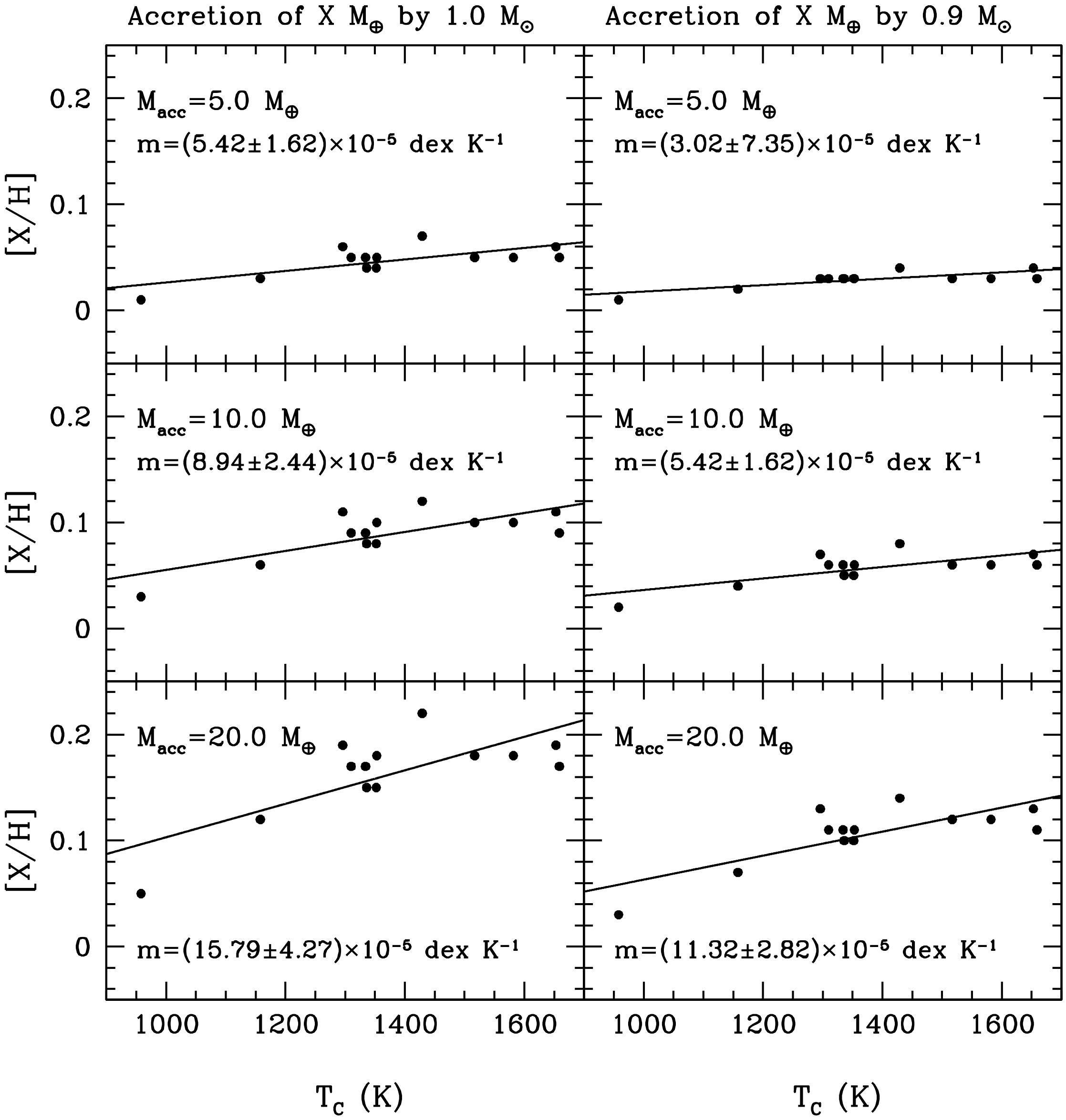

Figure 3.6: *Unweighted* linear fits to simulated abundances vs. condensation temperature ($T_{\rm C}$) from our modeled accretion of X amount of $M_\oplus$ by a solar-composition star (see Section 3.5.1). The *left* panel shows the results for the accretion of 5, 10, and 20 $M_\oplus$ by a 1.0 $M_\odot$ star, and the *right* panel shows the results for the accretion of the same three amounts of Earth-like material, but for a 0.9 $M_\odot$ star.

Raymond et al., 2011). This usually occurs because of planet-planet scattering in a rocky debris disk after the gas-rich protoplanetary disk has dissipated. Raymond et al. (2011) found that in 40% of their simulations, giants migrating in debris disk as as result of planet-planet scattering removed all rocky material from the planetary system, most of which was accreted by the host star. Furthermore, for giant planets with a minimum orbital distance less than ∼1 AU, all terrestrial material was destroyed. Both of the planets around HD 20781 have semi-major axes $\lesssim$0.3 AU, and the eccentric planet hosted by HD 20782 has a perihelion distance of only ∼0.04 AU. Therefore the simulations performed by Raymond et al. (2011) indicate that both planetary systems should be devoid of rocky material.

In addition, Kaib et al. (2013) also noted that over billions of years planets can be driven into their host stars because of the presence of a wide binary companion and Kozai resonances. As the binary pair orbits the galaxy, galactic tides can perturb the binary system and change the pericenter. At closest approach, each star can disrupt any planetary system that may exist around its binary companion. When Kaib et al. (2013) compared HD 20782/81 to wide binaries in their simulations with similar masses and semimajor axes, they found that ∼55% of the systems like HD 20782/81 triggered instabilities, and more that 90% of those instabilities occurred in the planetary system after 100 Myr. These instabilities resulted in planets colliding with the star 14% of the time. Therefore, both perturbations of the stellar binary as well as planetary migration through planet-planet scattering can lead to the ingestion of planetary material by the host star, and thereby generate the abundance patterns which are present in our data and predicted by our accretion model.

3.5.3 Comparison to previous work

Our findings, namely that the positive trends with $T_{\rm C}$ for the refractory elements indicate that both HD 20782/81 have accreted H-depleted, refractory-rich material, are consistent with the interpretations of Schuler et al. (2011a); Schuler et al. (2011b); Meléndez et al. (2009); Ramírez et al. (2009). In particular, Schuler et al. (2011a) analyzed abundances versus $T_{\rm C}$ trends for 10 stars known to host giant planets. The trends with $T_{\rm C}$ for these 10 stars were compared to a sample of 121 stars with and without detected giant planets from Gonzalez et al. (2010); the distribution of slopes with respect to [Fe/H] for the ∼120 stars from the Gonzalez et al. (2010) sample was interpreted as the general trend from Galactic chemical evolution. Of the 10 stars investigated by Schuler et al. (2011a), the four with very close-in (∼0.05 AU) giant planets were found to have positive slopes that lie above the Galactic trend. HD 20782/81 also have positive slopes that lie above this Galactic trend. The four stars from Schuler et al. (2011a) were also hypothesized to have ingested refractory-rich planetary material as a result of the evolution of their planetary systems. However, González Hernández et al. (2013) analyzed a sample of 61 late-F to early-G stars, 29 of which have detected planets and 32 do not. After correcting their trends with $T_{\rm C}$ for Galactic chemical evolution, they found that their stars with and without detected planets possessed similar [X/H]-$T_{\rm C}$ slopes. Therefore, they concluded that, in general, trends with $T_{\rm C}$ may not indicate the presence or absence of planets.

Part of the value of comparing coeval stars in wide binaries, is that any *difference* in their abundance trends is most certainly not the result of Galactic chemical processes. However, since HD 20782/81 exhibit *similar* abundance trends, this finding could in fact either be the result of the planet formation process or Galactic chemical evolution. In order to distinguish between these two scenarios, we compared the [X/H]-$T_{\rm C}$ slopes for HD 20782/81 to the distribution of slopes observed for the the ∼120 stars in the Gonzalez et al. (2010) sample. Among the stars within 0.1 dex of solar metallicity in this sample, the slopes of HD 20782/81 lie in the upper envelope of the distribution of slopes, which suggests that they are on the higher end of the Galactic trend. Furthermore, the fact that they both deviate from the Galactic trend in the same way also suggests that their abundances have most likely been changed by a similar process, i.e., the accretion of rocky planetary material. Finally, it is not obvious that Galactic chemical evolution can produce the specific element-by-element scatter that we observe (e.g., Na, Al, Sc, see Section 3.5.1), whereas the planet accretion scenario appears to reproduce it naturally, at least in our current simple model (Section 3.5.1).

Meléndez et al. (2009) and Ramírez et al. (2009) have performed studies of solar twins (stars with physical parameters nearly identical to the Sun), and found that solar refractory abundances decrease as a function of $T_{\rm C}$. Therefore, since the Sun formed terrestrial planets, they posit that a negative slope may indicate the presence of terrestrial planets, which contain the refractory-rich, H-depleted material that would have otherwise been accreted by the host star. Since we can rule out negative slopes for both HD 20782/81 at the 2σ level, the interpretation suggested by Meléndez et al. (2009) and Ramírez et al. (2009) implies that neither star hosts terrestrial planets, which, as noted previously for planetary systems with giant planets at $\lesssim$1 AU, is consistent with models of planet migration that predict that both

HD 20782/81 are unlikely to host rocky planets (Veras & Armitage, 2005; Raymond et al., 2011).

Unlike the work performed by Schuler et al. (2011a) on planet-hosting field stars, or the work by Meléndez et al. (2009) and Ramírez et al. (2009) on solar twins culled from a sample of field stars, or even the work by Schuler et al. (2011b) and Ramírez et al. (2011) on 16 Cyg, this paper's focus on HD 20782/81 permits the comparison of two coeval stars that *both* have detected planetary systems. The Kozai mechanism that is likely the source of the large eccentricity of 16 Cyg B b (Holman et al., 1997; Mazeh et al., 1997; Takeda & Rasio, 2005), is most likely the cause of the very high eccentricity of HD 20782 b as well. However, in the multiplanetary system hosted by the secondary star, the two planets HD 20781 b/c can dynamically interact with each other to suppress the effect of the Kozai mechanism, and prevent highly eccentric orbits (Innanen et al., 1997; Batygin et al., 2011; Kaib et al., 2011). Thus, while the architectures of the planetary systems hosted by HD 20782/81 are not identical, the fact that both stars possess giant planets with pericenters $\lesssim$0.2 AU probably resulted in the injection of $10 - 20\ M_{\oplus}$of Earth-like rocky material into both stars.

3.6 Conclusion

We have performed a detailed chemical abundance analysis of the planet-hosting wide binary HD 20782/81, which is presently the only known wide binary where both stars have detected planets. The mean element-to-element abundance difference between the two stars is 0.04 ± 0.07 dex, signifying that their bulk metallicities are identical, as expected for a binary system. Both stars show modestly significant ($\sim 2\sigma$) positive trends with T_{C} among their refractory elemental abundances. We cannot definitively rule out that these trends may be the result of Galactic chemical evolution. However, given the orbital characteristics of the stellar binary, and the fact that both stars have eccentric giant planets that approach within $\lesssim$0.2 AU, models of dynamical interactions between binary stellar companions and models of giant planet migration indicate that the host stars could have accreted rocky planetary bodies that would have initially formed interior to the giant planets. This is consistent with other studies that found positive trends with T_{C} in field stars with close-in giant planets.

According to our simple model for the accretion of Earth-like planets, the slopes of the weighted fits to these trends are consistent with HD 20782 accreting $\sim 10\ M_{\oplus}$ and HD 20781 accreting $\sim 20\ M_{\oplus}$ of material with Earth-like composition. Our model also predicts that there should not be a perfect correlation between refractory abundances and T_{C} for stars accreting H-depleted, rocky planetary material. Three elements (Na, Al, and Sc) are similarly discrepant with both the fit to the simulated data and the fit to the observed data. Therefore, the scatter in the [X/H]-T_{C} correlation is not necessarily due solely to observational noise, but may in fact be a signature of the accretion of refractory-rich material driven by the inward migration of the giant planets orbiting these stars. Indeed, the specific character of the element-by-element scatter might be used as a strong discriminant between the planetary accretion and Galactic chemical evolution scenarios. As we investigate other planet-hosting wide binaries, we hope to further refine these insights into abundances trends and their relation to the planet formation process.

Chapter IV

DETAILED ABUNDANCES OF PLANET-HOSTING WIDE BINARIES. II.
HD 80606+HD 80607

This chapter is based on work that will soon be submitted to the Astrophysical Journal.

4.1 Abstract

We present a detailed chemical abundance analysis of both stars in the planet-hosting wide binary system HD 80606 + HD 80607. Using high-resolution, high signal-to-noise echelle spectra obtained with Keck/HIRES, we derived the abundances ([X/H]) of 15 elements spanning a range of condensation temperatures ($T_{\rm C}$). Both stars are G5 dwarfs, and as in our previous analysis of the planet-hosting wide binary HD 20782 + HD 20781, we presume that the two stars formed at the same time within the same molecular cloud, and therefore had identical primordial chemical compositions. In this wide binary, HD 80606 is known to host a very eccentric ($e \sim 0.93$) giant planet at ∼0.5 AU, but HD 80607 has no detected planets. If close-in giant planets on eccentric orbits are very efficient at scattering rocky planetary material into their host stars, then one would expect that HD 80606 would show evidence of having accreted rocky material while HD 80607 would not. However, we found that the slopes of linear least-square fits to [X/H] vs $T_{\rm C}$ for HD 80606 and HD 80607 were statistically indistinguishable. This result may reflect the fact that the migration history of HD 80606 b was such that the giant planet was more likely to eject material from the system

rather than shepherd material in towards the star.

4.2 Introduction

This paper is the second in a series of papers that aims to investigate the relationship between the architectures of planetary systems and the detailed chemical composition of the host star by directly comparing the chemical abundances of each stellar pair in planet-hosting wide binaries. In the first paper (Mack et al. 2014), we analyzed the detailed chemical abundances of the planet-hosting wide binary HD 20782 + HD 20781. For both stars in that system, we found a trend between the elemental abundances ([X/H]) and the elemental condensation temperature (T_C) that, according to a simple model for the accretion of rocky planetary material by a solar-type star, was consistent with the ingestion of $10 - 20\ M_\oplus$ by each star.

In this paper, we present the analysis of the detailed abundance trends in the two stars comprising the HD 80606/07 system. HD 80606 and HD 80607 are a common proper motion wide binary with an angular separation of $20.6''$ and a projected physical separation of ~ 1200 AU (Raghavan et al. 2006). They are both solar-type stars with the same spectral type, G5V, and and apparent V magnitudes of 9.06 and 9.17, respectively (Kharchenko, 2001; ESA, 1997). HD 80606 hosts a $\sim 4\ M_{\rm Jup}$ on a very eccentric ($e \sim 0.93$) orbit at $\sim$0.5 AU (Pont et al., 2009). On the other hand, there are no detected planetary-mass companions to HD 80607.

If the presence of a close-in eccentric giant planet is an indicator that the host star has likely accreted a significant amount of rocky planetary material, as may be the case with HD 20782/81 (Mack et al. 2014) and a subset of single stars analyzed by Schuler et al. (2011a), then one might expect that the chemical abundances of HD 80606 might show evidence of rocky planetary accretion, while HD 80607 would not. If the chemical abundances of HD 80606/07 are not found to be distinct, then this suggests that there are other factors besides the present-day architecture of the planetary system that determine the amount of hydrogen-depleted refractory material that is ingested by a planet-hosting star. One of these factors might be the specific migration history of the giant planets in the system. As a result, not all host stars with close-in giant planets would necessarily exhibit the abundance trends seen in HD 20782/81. Indeed, the degree of the correlation between planetary-system architecture and the chemical composition of the host star is the main goal of this ongoing series of papers. If a correlation is discovered, then while we cannot expect it to be true for each specific system, it could still serve as tool for more targeted searches for Solar System analogs in general.

In Section 4.3, we describe our observations and spectral analysis. In Section 4.4, we present the main results, In Section 4.5 we discuss the results in the context of a simple model for how the accretion of Earth-like rocky planets would affect refractory elemental abundances as a function of T_{C}, as well as the results of numerical simulations found in the literature, that investigation how giant planet migration affects planetary material interior to the orbit of the giant. Finally, in Section 4.6 we briefly summarize the main conclusions.

4.3 Data and Analysis

For both HD 80606/07, on UT 2011 Mar 14 we obtained high-resolution, high-signal-to-noise ratio (SNR) spectra with the 10-m Keck I telescope and the HIRES echelle spectrograph (Vogt et al., 1994) in the $R = \lambda/\Delta\lambda = 72,000$ mode. We used the kv418 filter with the B2 slit setting ($0.574'' \times 7''$) and 2×1 binning (spatial × dispersion). The spectra covered a wavelength range from $\sim 3500 - 9500$Å. For each of the stars in the system, one exposure was taken with an integration time of 900s. The SNR in the continuum region near λ6700 of ∼300 for HD 80607 and ∼330 for HD 80606. The data were reduced using the MAKEE data reduction routines. A sample spectrum spanning the wavelength region λ6135-λ6175 is shown in Figure 4.1. We were unable to obtain a solar spectrum during the same observing run that we observed HD 80606/07. Therefore, for the derivation of the relative chemical abundances, we used a previous Keck/HIRES solar spectrum that we obtained in 2010 June. The solar spectrum has an SNR of ∼800 near λ6700.

For both HD 80606/07, chemical abundances relative to solar have been derived from the observed spectra for 15 elements. We used the 2010 version of the LTE spectral analysis package MOOG (Sneden, 1973) to perform the spectral analysis. The abundances were derived from measurements of the equivalent widths (EWs) of atomic lines using the SPECTRE analysis package (Fitzpatrick & Sneden, 1987). Stellar parameters were obtained by requiring excitation and ionization balance of the Fe I and Fe II lines. The atomic excitation energies (χ) and transition probabilities ($\log gf$) were taken from the Vienna Atomic Line Database (VALD; Piskunov et al., 1995; Kupka et al., 1999).

For the odd-Z elements V, Mn, and Co, in order to take into account hyper-fine structure (hfs) effects (Prochaska & McWilliam, 2000), spectral synthesis incorporating hfs components has been used to compare with the EW-based abundances. The hfs components for these elements were obtained from Johnson et al. (2006), and the line lists for wavelength regions encompassing each feature were taken from VALD. The adopted V, Mn, and Co abundances are derived from the hfs analysis and those lines with EWs that are less affected by hfs.

The abundance and error analyses for all elements are described in greater detail in Schuler et al. (2011a). The analysis we performed was nearly identical to our analysis of the planet-hosting wide binary HD 20782/81 (Mack et al. 2014). The stellar parameters and relative abundances

for HD 80606/07 are summarized in Table IV.1. The adopted line list, EWs, and line-by-line abundances of each element for HD 80606/07 and the Sun are given in Table IV.2.

4.4 Results

The stellar parameters (Table IV.1) determined for HD 80606/07 are consistent with both stars having a ~G5V spectral type. The stellar parameters agree within 1-σ: $\Delta T_{\rm eff} = 52 \pm 62$ K, $\Delta \log g = 0.04 \pm 0.10$ dex, and $\Delta \xi = 0.10 \pm 0.10$ km s^{-1}. The differential abundances of the 15 individual elements are plotted in Figure 4.2. These differential abundances are the means of the line-by-line differences for each element. The mean abundance difference is 0.022 ± 0.017 dex (HD 80607 − HD 80606).

Figures 4.3 and 4.4 show the elemental abundances of HD 80606/07 versus $T_{\rm C}$. The condensation temperatures were taken from the 50% $T_{\rm C}$ values listed in Lodders (2003). We performed both unweighted and weighted linear fits to the [X/H] versus $T_{\rm C}$ abundance relations to investigate possible correlations. As can be seen in Figure 4.3, the slopes of the unweighted linear least-squares fits are $m_{06} = (-11.56 \pm 6.40) \times 10^{-5}$ dex $\rm K^{-1}$ and $m_{07} = (-8.31 \pm 7.45) \times 10^{-5}$ dex $\rm K^{-1}$ for HD 80606 and HD 80607 respectively. In Figure 4.4, the slopes of the weighted linear least-squares fits are $m_{06} = (-0.92 \pm 0.21) \times 10^{-5}$ dex $\rm K^{-1}$ and $m_{07} = (-0.54 \pm 0.30) \times 10^{-5}$ dex $\rm K^{-1}$. For both the unweighted and weighted linear fits, the slopes are statistically indistinguishable, and within 2-σ the slopes are consistent with zero.

In the next section, we discuss these results in the context of a model that predicts the correlation between the elemental abundances and $T_{\rm C}$, assuming that HD 80607 has accreted some amount of rocky planetary material. Also, we consider how the accretion scenario might differ for host stars with close-in ($\lesssim$1 AU) giant planets on more circular orbits compared to host stars with close-in giants on more eccentric orbits.

4.5 Discussion

4.5.1 A model for the accretion of rocky planetary material by HD 80607

In our analysis of HD 20782/81 (Mack et al. 2014), we created a simple model for the impact that the accretion of a rocky planet would have on the atmospheric composition of a solar-type star. Because the bulk compositions of HD 20782/81 ($\rm [Fe/H]_{82} = -0.02$ and $\rm [Fe/H]_{81} = +0.04$) were consistent with solar, we were able to use our model to infer that the slope of [X/H] vs $T_{\rm C}$ for HD 20782 was consistent with the ingestion of $\sim$10 $M_\oplus$, while the slope for HD 20781 was consistent with the ingestion of $\sim$20 $M_\oplus$.

However, since the bulk compositions of HD 80606/07 ($[\rm Fe/H]_{06} = +0.35$ and $[\rm Fe/H]_{07} = +0.35$) are not consistent with solar, and are in fact quite metal-rich, we needed to modify our model accordingly. Instead of assuming the primordial composition of HD 80606/07 was consistent with solar (as we did in the case of HD 20782/81), we assumed that the primordial composition of HD 80606/07 was consistent with the present-day composition of HD 80607. We made this assumption because both Mack et al. 2014 and Schuler et al. (2011a) suggested that host stars with close-in ($\lesssim$1 AU) giant planets may exhibit abundance trends with $T_{\rm C}$ that are consistent with the accretion of rocky planetary material. Therefore, since HD 80606 is known to host a very eccentric close-in giant, while HD 80607 does not, we would expect that only HD 80606 would have accreted rocky planetary material, as a result of HD 80606 b pushing material into the star as it migrated inward to its present location.

In modifying our model so that the primordial composition is consistent with HD 80607, we began with the same approached described in Mack et al. 2014. Namely, we determine the amount of a given element present in X $M_\oplus$ of rocky material. Then we determine the amount of the same element present in the convection zone of a X $M_\odot$ star. By adding these two amounts together, we can derive how much the photospheric abundance of a given element increases as a result of accreting a rocky planet. In our previous paper, to determine the amount of a given element initially present in the convection zone, we used the solar photospheric abundances given in Asplund et al. (2009) (since HD 20782/81 had bulk compositions consistent with solar, this was a reasonable assumption). However, in this paper, instead of setting the initial photospheric abundance (i.e., the primordial abundance of the element in the convection zone) equal to the present-day solar photospheric abundances, we set the initial photospheric abundance equal to the present-day abundances for HD 80607. Also, even though HD 80606/07 are much more metal-rich, given their effective temperatures, we would expect their masses to be similar to solar. Furthermore, Pinsonneault et al. (2001) showed that for stars with $T_{\rm eff} = 5500 - 5600$ K, the mass in the convection zone ranges from $\sim 0.03 - 0.04\ M_{\odot}$. Therefore, in our model, it is a reasonable approximation to set the mass of HD 80607 to the mass of the Sun, and the mass of the convection zone in HD 80607 to the mass of the solar convection zone.

The results of simulating the accretion of 5 $M_{\oplus}$ and 20 $M_{\oplus}$ by HD 80607 are shown in Figures 4.5–4.6. Like the planetary accretion model for solar-type stars in Mack et al. 2014, the accretion model for metal-rich stars like HD 80607 also predicts that the accretion of rocky planetary material with Earth-like composition tends to create a more positive correlation between [X/H] and $T_{\rm C}$. Increasing the amount of accreted material causes the slopes to become more positive (or equivalently, less negative). However, even though the values of the slopes increase from -8.31 (the trend in the present-day abundances of HD 80607, which are assumed to be equivalent to the primordial abundances in our model) to -1.02 (the trend after the addition of 20 $M_{\oplus}$), the uncertainties in the slopes are so large that the slopes are statistically indistinguishable. This is likely the result of the large scatter in the abundances with respect to the trendlines.

4.5.2 Interpretation of the similar trends found in the abundances of HD 80606/07

Given the proximity of HD 80606 b to its host star, as well as its very eccentric orbit, one might expect that it would have injected a detectable amount of rocky planetesimals into the host star. Given that HD 80607 does not host a close-in giant planet, one might expect its present-day photospheric abundances to be essentially identical to its primordial abundances. Therefore, it is surprising that HD 80606 b did not push enough rocky planetary material into the host star for trends between [X/H] vs $T_{\rm C}$ to be statistically distinct when comparing HD 80606 to HD 80607. The fact that the $T_{\rm C}$-slopes are so similar may result from the migration history of HD 80606 b, which could be quite different from the migration history of HD 20782 b or HD 20781 b/c, two planetary systems with eccentric, close-in giant planets that appear to have accreted a significant amount of rocky planetary material. It may be that less eccentric close-in giant planets are more effective at shepherding inner rocky planetesimals into the host star. HD 20781 b/c may have been more effective than HD 20782 b which may have been more effective than HD 80606 b.

The idea is that giant planets that migrate inward on more circular orbits are more effective at shepherding rocky planetesimals inside their orbits toward the host stars. Giant planets migrating on eccentric orbits are more likely to be disruptive and eject material inside their orbits from the planetary system (or accrete the material onto the giant planets themselves). This idea may have some merit given that among the host stars that we have analyzed so far, the one with the strongest correlation between [X/H] and $T_{\rm C}$ is HD 20781 which has the giant planets on the most circular orbits (Table IV.3).

Furthemore, numerical simulations of planetary migration seem to suggest that less eccentric giant planets tend to be more efficient shepherders. Many studies of giant planet migration have shown that material interior to a giant planet's orbit can become trapped in mean-motion resonances (e.g., Raymond et al. 2006). Furthermore, the type of resonance that the material becomes locked in depends on the initial eccentricities and the relative rate of migration that would take place if the giant planet and the material were to migrate independently (Lubow & Ida, 2011). In addition, Raymond et al. 2006 note that giant planets that migrate faster tend to increase the survival rate of material exterior to the giant planet's orbit, and giant planets that migrate slower tend to decrease the survival of material exterior to the giant planet's orbit.

In summary, the survival rate of material interior to a migrating giant planet's orbit depends on the giant planet's migration speed: fast migration tends to cause less material to be shepherded in towards the star, and while slow migration tends to be more effective at shepherding. Therefore, planetary systems with similar present-day architectures may leave dissimilar chemical imprints on the surfaces of their host stars as a result of their different migration histories.

4.6 Conclusion

We have performed a detailed chemical abundance analysis of the planet-hosting wide binary HD 80606/07. The mean element-to-element abundance difference between the two stars is 0.022 ± 0.017 dex (HD 80607 $-$ HD 80606). Linear least-squares fits to plots of the refractory elemental abundancs ([X/H]) versus elemental condensation temperature (T_{C}) yield slopes that are statistically indistinguishable. Given the fact that HD 80606 has a very eccentric giant planet that approaches within $\lesssim$0.03 AU, it is surprising that its slope for [X/H] versus T_{C} does not suggest the accretion of rocky planetary material, unlike the stars in the wide binary HD 20782/81, which both have close-in eccentric giant planets.

The lack of a statistically significant correlation between the chemical abundances of HD 80606 and T_{C} may be a result of the migration history of its giant planet. If the giant planet migrated inward quickly, then it may have been an inefficient shepherder of material interior to its orbit, and thereby was much less likely to push a significant amount of rocky planetary material into the host star. Since HD 80606 b's present-day eccentricity is related to its migration history, it may be that more eccentric giant planets, when compared to less eccentric giant planets, are less efficient at shepherding planetary material into their host stars. This idea seems plausible given that larger orbital eccentricities are often the result of a more violent migration history, such as planet-planet scattering.

Table IV.1. HD 80606/07: Stellar Parameters & Abundances

	HD 80606	HD 80607
$T_{\rm eff}$ (K)	5613 ± 44	5561 ± 43
$\log g$ (cgs)	4.43 ± 0.08	4.47 ± 0.06
ξ (km s^{-1})	1.36 ± 0.07	1.26 ± 0.07
[Na/H][a]...	$+0.45 \pm 0.03$[b] ± 0.05[c]	$+0.46 \pm 0.04 \pm 0.05$
[Mg/H][d]..	$+0.40 \pm 0.00 \pm 0.03$	$+0.47 \pm 0.00 \pm 0.03$
[Al/H] ...	$+0.39 \pm 0.01 \pm 0.03$	$+0.37 \pm 0.02 \pm 0.03$
[Si/H] ...	$+0.34 \pm 0.01 \pm 0.01$	$+0.34 \pm 0.01 \pm 0.01$
[Ca/H] ...	$+0.28 \pm 0.01 \pm 0.05$	$+0.31 \pm 0.01 \pm 0.04$
[Sc/H] ...	$+0.36 \pm 0.02 \pm 0.04$	$+0.39 \pm 0.04 \pm 0.05$
[Ti/H] ...	$+0.36 \pm 0.02 \pm 0.05$	$+0.42 \pm 0.02 \pm 0.05$
[V/H]	$+0.41 \pm 0.01 \pm 0.05$	$+0.45 \pm 0.02 \pm 0.06$
[Cr/H] ...	$+0.34 \pm 0.04 \pm 0.06$	$+0.39 \pm 0.04 \pm 0.05$
[Mn/H][d]..	$+0.42 \pm 0.00 \pm 0.06$	$+0.39 \pm 0.00 \pm 0.06$
[Fe/H] ...	$+0.35 \pm 0.01 \pm 0.02$	$+0.35 \pm 0.01 \pm 0.02$
[Co/H] ...	$+0.44 \pm 0.01 \pm 0.04$	$+0.46 \pm 0.01 \pm 0.04$
[Ni/H] ...	$+0.40 \pm 0.01 \pm 0.03$	$+0.43 \pm 0.01 \pm 0.03$

[a] Adopted solar parameters: $T_{\rm eff} = 5777$ K, $\log g = 4.44$, and $\xi = 1.38$ km s^{-1}.

[b] σ_μ – the uncertainty in the mean

[c] σ_{Total}– quadratic sum of σ_μ and uncertainties due to uncertainties in $T_{\rm eff}$, $\log g$, and ξ.

[d] In both stars, the abundance measurements for Mg and Mn were determined from a single spectral line. That is why the uncertainty in the mean is 0.00 in both stars.

Table IV.2. HD 80606/07: Lines Measured, Equivalent Widths, and Abundances

	λ	χ				HD 80606		HD 80607	
Ion	(Å)	(eV)	log gf	$\mathrm{EW}_\odot$	$\log N_\odot$	EW	$\log N$	EW	$\log N$
Na I	5682.63	2.10	-0.700	100.9	6.30	142.9	6.70	146.0	6.70
	6154.23	2.10	-1.560	38.4	6.31	76.5	6.77	80.4	6.80
	6160.75	2.10	-1.260	56.1	6.28	100.6	6.78	102.1	6.77

Note. — This table is provided in its entirety in the appendix. A portion is shown here for guidance regarding its form and content.

Table IV.3. Giant Planet Orbital Characteristics & Host Star [X/H] vs T_C Slopes

	Mass (M_Jup)	a (AU)	e	Host star T_C-slope	Host star [Fe/H]
HD 20781 b,c[a]	0.04,0.05	0.17,0.35	0.11,0.28	$(+13.60 \pm 6.57) \times 10^{-5}$	+0.04
HD 20782 b	1.9	1.38	0.97	$(+9.71 \pm 4.57) \times 10^{-5}$	−0.02
HD 80606 b	3.9	0.45	0.93	$(-0.92 \pm 0.21) \times 10^{-5}$	+0.35
16 Cyg B b	1.68	1.68	0.69	$(+4.42 \pm 1.94) \times 10^{-5}$	+0.05

[a] Values for the orbital parameters obtained from The Extrasolar Planets Encyclopedia (exoplanet.eu).

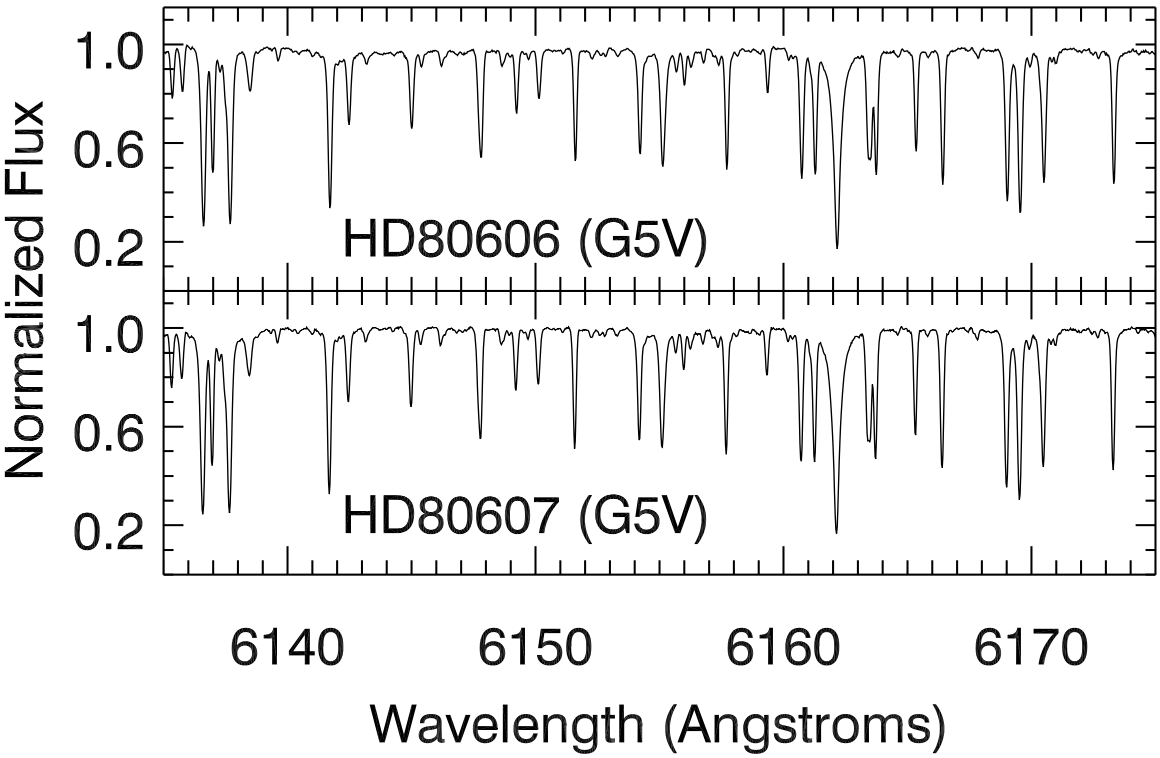

Figure 4.1: Sample Keck/HIRES spectra for HD 80606/07, spanning the wavelength range from $\lambda6135 - \lambda6175$.

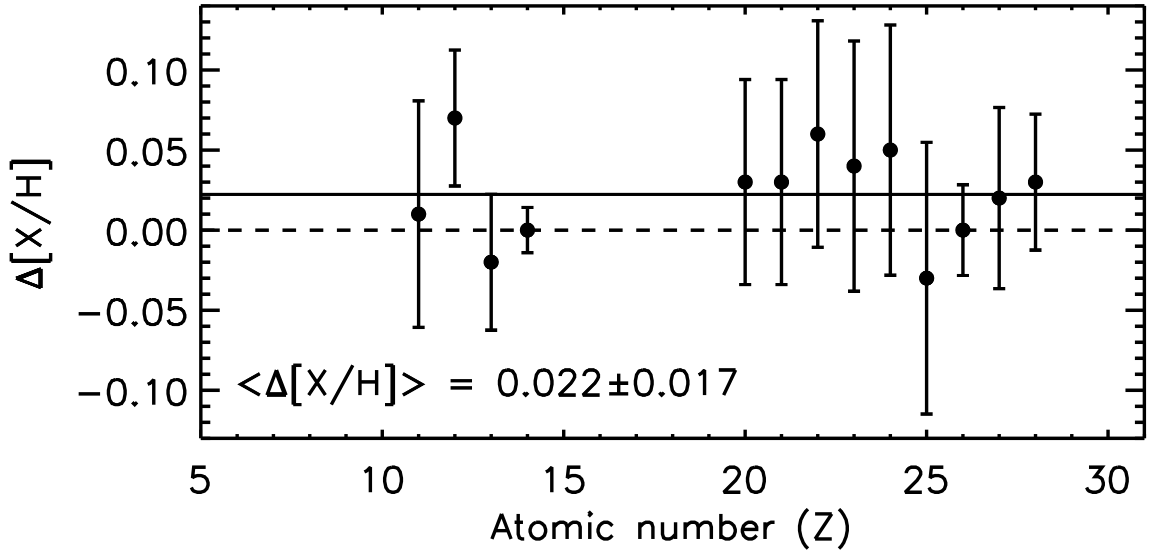

Figure 4.2: Differential abundances (HD 80607 − HD 80606) as a function of atomic number (Z). The solid line represents the mean difference of 0.022 ± 0.017 dex, and the dashed line is meant to guide the eye at 0.00 dex.

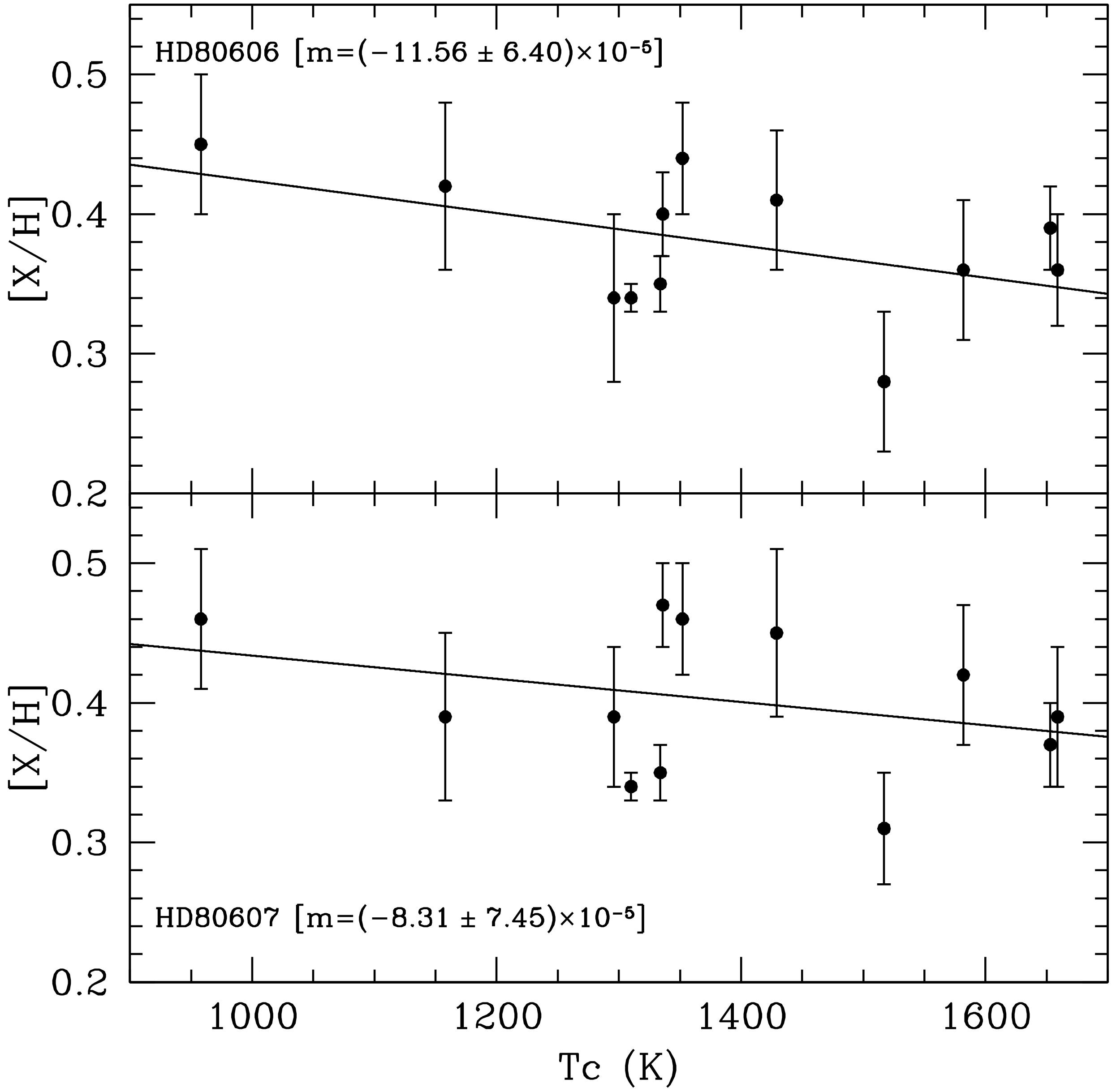

Figure 4.3: *Unweighted* linear fits to abundance vs. condensation temperature (T_C) for HD 80606/07.

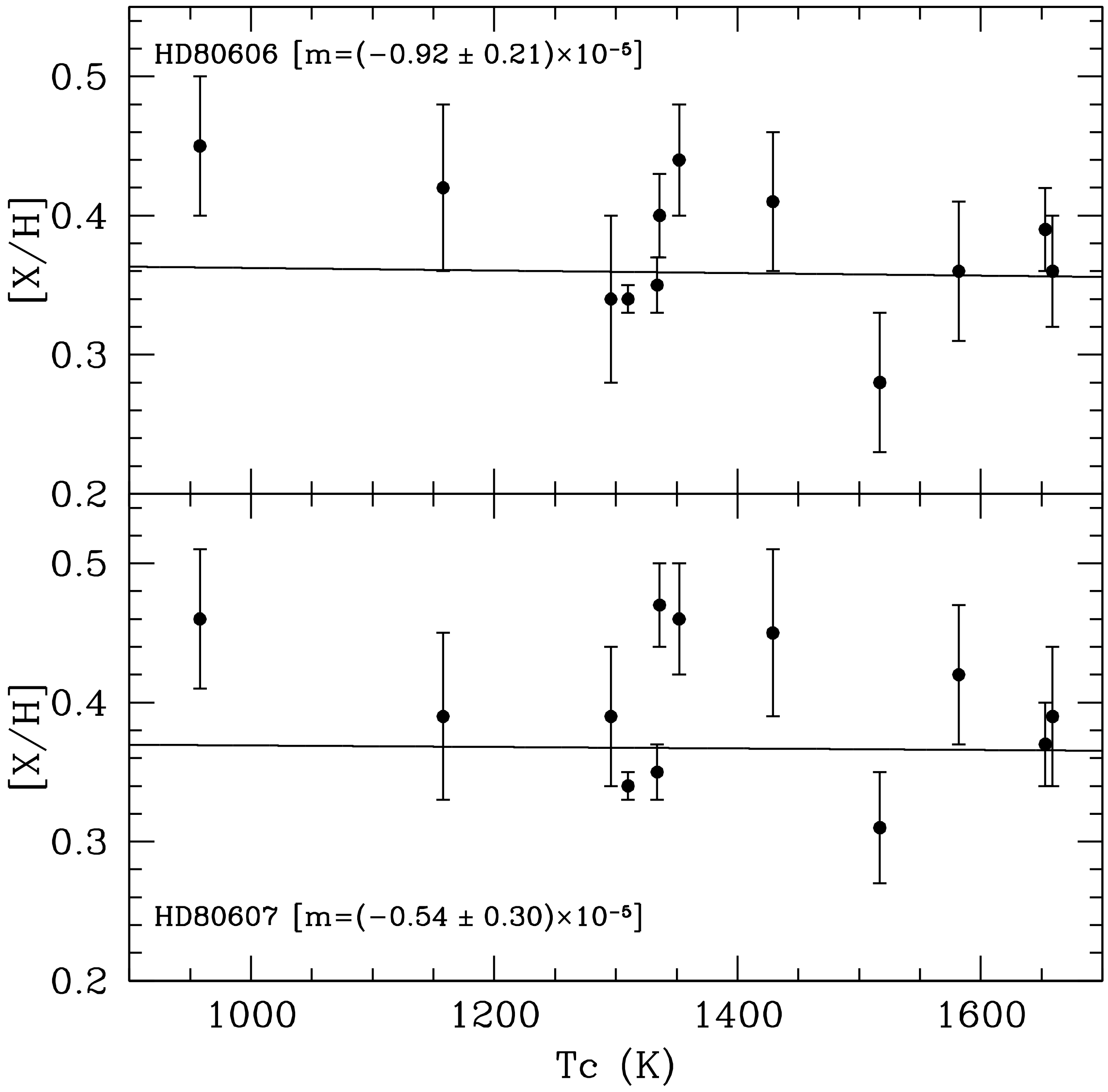

Figure 4.4: *Weighted* linear fits to abundances vs. condensation temperature (T_C) for HD 80606/07.

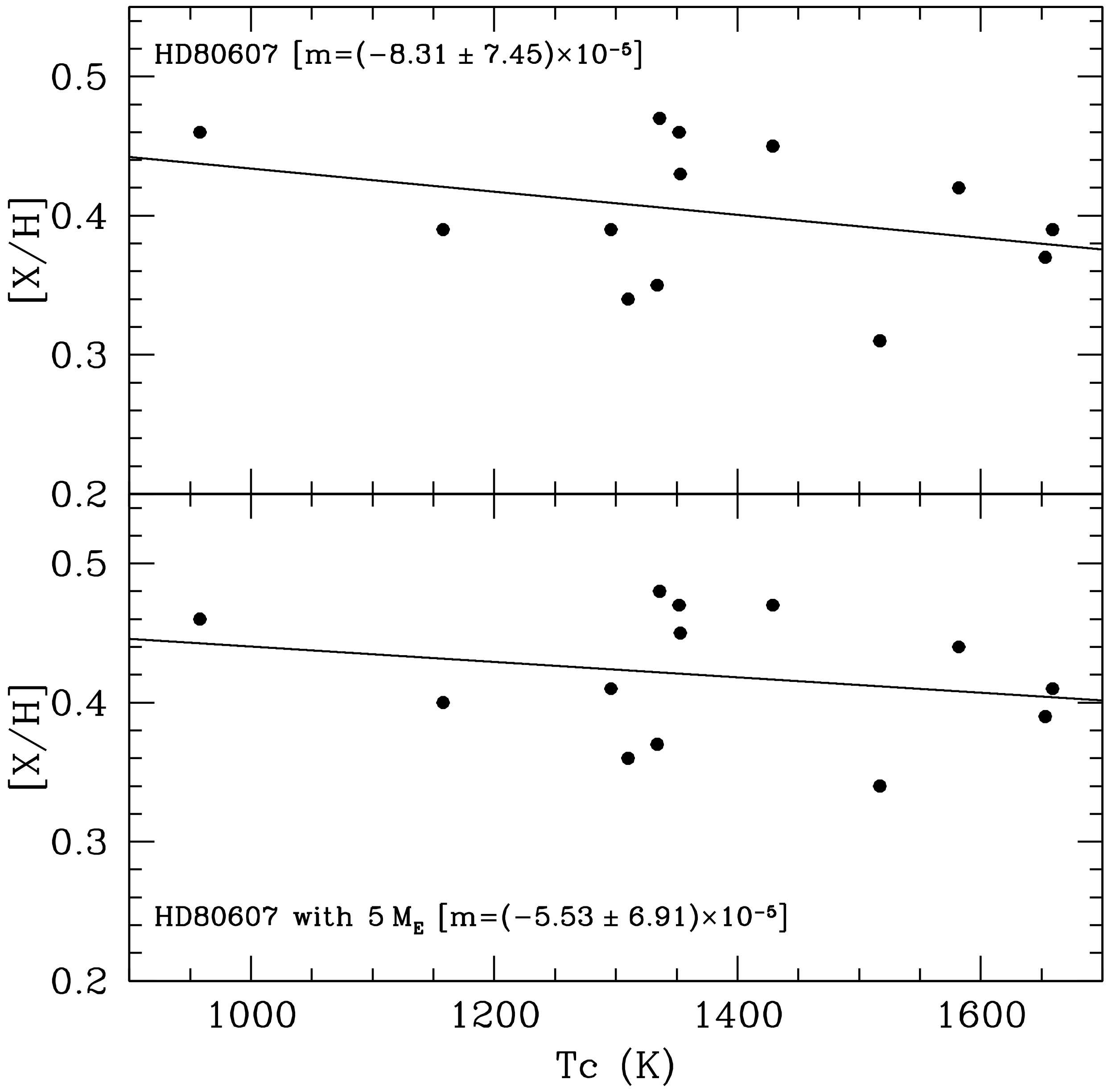

Figure 4.5: *Unweighted* linear fits to simulated abundances vs. condensation temperature (T_{C}) from our modeled accretion of $5M_{\oplus}$ of material with Earth-like composition by a star like HD 80607.

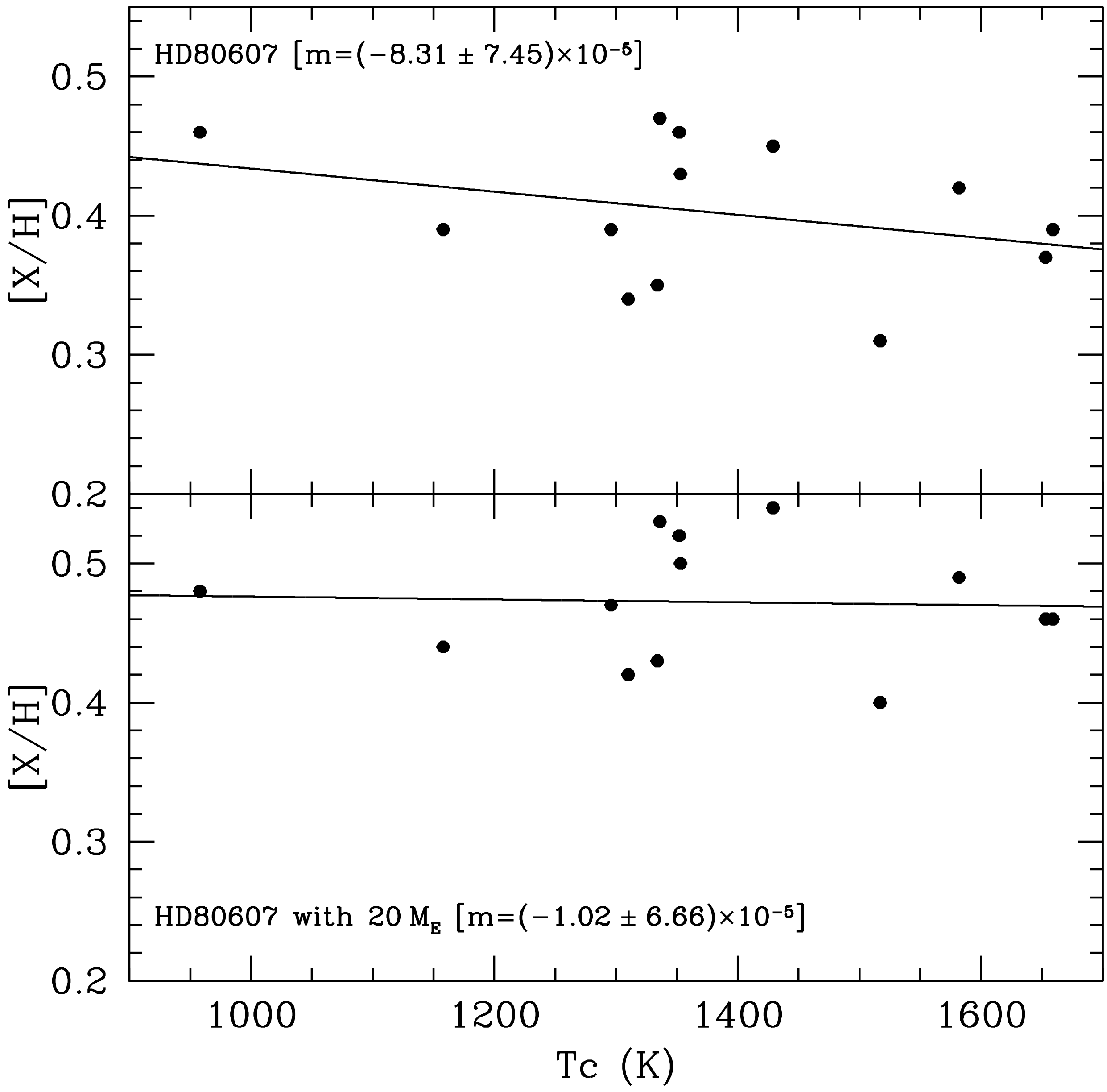

Figure 4.6: *Unweighted* linear fits to simulated abundances vs. condensation temperature (T_C) from our modeled accretion of $20M_\oplus$ of material with Earth-like composition by a star like HD 80607.

Chapter V

FUTURE WORK

At the present time, the future research plan is to continue analyzing the sample of known planet-hosting wide binaries where both stellar components are FGK stars (i.e., the kinds of stars that can be analyzed with our method of determining the detailed chemical composition). In addition to HD 20782/81 and HD 80606/07, we have data for about seven other systems (also obtained with either Keck/HIRES or Magellan/MIKE). With the results from these additional seven planet-hosting wide binaries, and the results from HD 20782/81 and HD 80606/07 (plus the previously analyzed 16 Cyg A and B), we will be able to begin to see what kinds of patterns or trends in the detailed abundances may exist among our sample. With only 10 systems, we cannot make any strong statistical claims, but as the number of known planet-hosting wide binaries continues to grow[1], we hope to build a catalog that can be used to perform a thorough statistical analysis once the sample size is large enough.

In addition to planet-hosting wide binaries, we also plan to begin an investigation of planet-hosting open clusters. Just like wide binaries, open clusters provide the special opportunity to compare the detailed chemical compositions of stars that presumably formed from the same material at the same time, but with an added bonus: open clusters inherently contain a large sample of stars with similar spectral types for comparing planet-hosts

---

[1] At least five additional systems suitable for our sample were reported over the past year or so!—HD 108863 AB, HAT-P-4 AB, WASP-94 AB, WASP-77 AB and WASP-70 AB; see Maxted et al. (2013); Anderson et al. (2014); Neveu-VanMalle et al. (2014); Mugrauer et al. (2014)

to non-planet-hosts. Currently, we have Keck/HIRES spectra for a sample of stars in the first known planet-hosting open cluster[2]: the Praesepe (or "Beehive") cluster (Quinn et al., 2012). In this cluster, we obtained spectra of a planet-hosting cluster member, as well as three other cluster members whose RVs were monitored by Quinn et al. (2012), and as a result, we can be reasonably sure that these three stars do not host any "hot Jupiters". After analyzing the detailed composition of the stars in our Praesepe sample, we hope to perform similar analyses with other known planet-hosting clusters, such as the Hyades cluster, M 67, and NGC 6811 (Quinn et al., 2014; Brucalassi et al., 2014; Meibom et al., 2013).

Finally, there are two nascent projects that will utilize the spectroscopic analysis skills gained from the work on planet-hosting wide binaries and open clusters. The ideas for these projects are in their infancy, and have not been completely fleshed out. The first project would be to perform detailed abundance analysis of planet-hosting stars detected by the KELT transiting survey for exoplanets[3] For the KELT sample, the statistical biases are well understood, so even though the sample consists of a number of single stars, it could be a useful testing ground for confirming that any chemical abundance trends uncovered among stars in planet-hosting wide binaries and open clusters, are also present in single stars with similar kinds of planetary system architectures.

In a somewhat similar vein, with the sample of planet-hosts discovered by the *Kepler* mission, it may be possible to investigate the relationship between the age and chemical

---

[2] That is, the first open cluster with the confirmed detection of exoplanets around solar-type stars.

[3] One of the KELT planet-hosts is actually a component of a wide binary that will become a part of our sample.

composition of a host star and the size of its giant planets. There is evidence that metal-poor stars host giant planets that on average tend to have larger radii than giant planets around metal-rich stars (Dodson-Robinson, 2012). Such a trend seems plausible given that metal-poor stars should produce metal-poor planets, and metal-poor planets should be less dense, and therefore have larger radii, then metal-rich planets of the same mass. As a result, by using a large enough sample of Kepler stars known to host giant planets, one could determine if there was a strong correlation between host star age and composition, and the size of its giant planet(s). Such a correlation might show that giant planet radii are directly related to Galactic chemical evolution.

Appendix A

TABLE II.1: COMPLETE AND UNABRIDGED

Table A.1. Observed heliocentric single-lined radial velocities for TYC 3010

HJD	Instrument$^{\mathrm{a}}$	RV (km s^{-1})	σ_{RV} (km s^{-1})
2454927.82470	M	62.681	0.148
2454928.85061	M	62.564	0.139
2454964.76792	M	61.479	0.108
2454965.77714	M	61.374	0.113
2454994.69536	M	59.933	0.115
2455193.91250	M	62.102	0.165
2455197.96727	M	61.753	0.134
2455198.94828	M	61.714	0.095
2455199.96552	M	61.664	0.139
2455200.98947	M	61.585	0.097
2455201.97760	M	61.587	0.116
2455202.99063	M	61.528	0.149
2455258.88272	M	39.192	0.091
2455259.83118	M	41.327	0.092
2455260.82412	M	45.097	0.145
2455261.82050	M	48.416	0.096
2455280.77587	M	61.103	0.105
2455280.76844	M	61.174	0.117
2455283.81484	M	61.411	0.154
2455284.75054	M	61.461	0.112
2455311.68421	M	62.493	0.209
2455313.62591	M	62.402	0.174
2455369.64423	M	62.531	0.333
2455551.99403	M	62.788	0.120
2455552.98222	M	62.856	0.104
2455553.98561	M	62.795	0.121

Table A.1 (cont'd)

HJD	Instrument[a]	RV (km s^{-1})	σ_{RV} (km s^{-1})
2455556.97163	M	62.821	0.123
2455557.97465	M	62.801	0.104
2455471.98302	A	60.138	0.116
2455519.95995	A	61.359	0.052
2455519.98157	A	61.371	0.051
2455637.88366	A	62.452	0.055
2455637.92209	A	62.278	0.048
2455654.83350	A	62.390	0.059
2455665.65219	A	62.323	0.065
2455665.69165	A	61.664	0.075
2455669.60113	A	61.827	0.052
2455686.82409	A	60.946	0.076
2455695.66512	A	60.949	0.039
2455695.70529	A	60.931	0.053
2455703.61994	A	60.942	0.116
2455709.77767	A	59.749	0.098
2455903.90846	H	62.448	0.051
2455917.87269	H	62.237	0.060
2455928.84083	H	61.759	0.046
2455940.80855	H	61.122	0.058
2455946.80490	H	60.285	0.055
2455950.80134	H	59.539	0.045
2455953.82447	A	58.385	0.049
2455954.00566	H	58.467	0.050

[a] Instruments: MARVELS (M), ARCES (A), and HRS (H) spectrographs.

Note. — The ARCES and HRS RV values were measured as absolute heliocentric RVs, while the MARVELS discovery data were measured on a relative instrumental scale; the MARVELS RVs have been offset to the same (heliocentric) scale as the ARCES and HRS measurements.

Appendix B

TABLE III.2: COMPLETE AND UNABRIDGED

Table B.1. HD 20782/81: Lines Measured, Equivalent Widths, and Abundances

	λ	χ					HD 20782			HD 20781		
Element	(Å)	(eV)	log gf	EW$_\odot$	log $N_\odot$	log $N_{\odot,\mathrm{synth}}$[a]	EW	log N	log N_{synth}	EW	log N	log N_{synth}
C I	5052.17	7.68	-1.304	36.2	8.51	···	36.1	8.50	···	17.2	8.35	···
C2	5086	···	···	···	···	8.43	···	···	8.32	···	···	8.35
C2	5135	···	···	···	···	8.44	···	···	8.36	···	···	8.43
C I	5380.34	7.68	-1.615	22.8	8.54	···	20.8	8.47	···	10.9	8.44	···
O I	6300.30	0.00	-9.717	5.5	8.69	···	6.3	8.72	···	6.5	8.52	···
O I	7771.94	9.15	0.369	65.6	8.77	···	71.2	8.84	···	34.7	8.71	···
O I	7774.17	9.15	0.223	57.8	8.79	···	60.5	8.82	···	30.4	8.74	···
O I	7775.39	9.15	0.001	46.5	8.80	···	47.5	8.81	···	23.1	8.75	···
Na I	5682.63	2.10	-0.700	119.9	6.52	···	107.9	6.41	···	135.1	6.41	···
Na I	6154.23	2.10	-1.560	38.2	6.31	···	33.2	6.23	···	49.2	6.23	···
Na I	6160.75	2.10	-1.260	58.1	6.31	···	53.9	6.26	···	76.4	6.31	···
Mg I	5711.09	4.35	-1.833	100.8	7.56	···	102.0	7.59	···	128.3	7.66	···
Mg I	6841.19	5.75	-1.610	64.1	7.85	···	66.0	7.89	···	74.6	8.14[b]	···
Al I	6696.02	3.14	-1.347	36.7	6.24	···	34.9	6.23	···	52.7	6.28	···
Al I	6698.67	3.14	-1.647	20.7	6.21	···	19.8	6.20	···	32.6	6.25	···
Si I	5690.43	4.93	-1.769	53.6	7.53	···	47.3	7.44	···	51.1	7.52	···
Si I	5701.10	4.93	-1.581	39.2	7.11	···	35.9	7.05	···	36.1	7.07	···
Si I	5708.40	4.95	-1.034	74.2	7.11	···	73.9	7.11	···	75.4	7.16	···
Si I	5772.15	5.08	-1.358	57.0	7.31	···	54.2	7.27	···	53.8	7.29	···
Si I	6125.02	5.61	-1.464	31.5	7.46	···	32.3	7.48	···	27.7	7.43	···
Si I	6142.48	5.62	-1.295	35.7	7.37	···	34.4	7.35	···	32.7	7.36	···
Si I	6145.02	5.62	-1.310	40.5	7.46	···	38.1	7.42	···	35.7	7.43	···
Si I	6243.81	5.62	-1.242	48.6	7.52	···	47.1	7.50	···	43.7	7.50	···

Table B.1 (cont'd)

	λ	χ					HD 20782			HD 20781		
Element	(Å)	(eV)	log gf	$\mathrm{EW}_\odot$	$\log N_\odot$	$\log N_{\odot,\mathrm{synth}}$[a]	EW	$\log N$	$\log N_\mathrm{synth}$	EW	$\log N$	$\log N_\mathrm{synth}$
Si I	6244.47	5.62	-1.093	45.8	7.33	···	46.6	7.34	···	43.7	7.35	···
Si I	6414.98	5.87	-1.035	54.3	7.58	···	51.5	7.54	···	46.8	7.54	···
Si I	6741.63	5.98	-1.428	15.0	7.34	···	16.1	7.38	···	12.3	7.31	···
Si I	6848.58	5.86	-1.524	17.3	7.40	···	17.4	7.40	···	14.8	7.38	···
Si I	7405.77	5.61	-0.313	84.1	7.04	···	82.9	7.02	···	80.1	7.05	···
Ca I	5867.56	2.93	-1.570	26.4	6.35	···	25.4	6.34	···	36.3	6.29	···
Ca I	6161.30	2.52	-1.266	67.6	6.37	···	69.9	6.43	···	95.7	6.52	···
Ca I	6166.44	2.52	-1.142	71.0	6.30	···	72.6	6.35	···	95.6	6.39	···
Ca I	6169.04	2.52	-0.797	96.0	6.33	···	96.8	6.37	···	125.7	6.41	···
Ca I	6169.56	2.53	-0.478	116.0	6.28	···	116.9	6.32	···	153.8	6.36	···
Ca I	6455.60	2.52	-1.340	54.0	6.21	···	54.4	6.24	···	74.7	6.26	···
Ca I	6493.78	2.52	-0.109	126.4	6.01	···	127.6	6.05	···	160.5	6.02	···
Ca I	6499.65	2.52	-0.818	85.9	6.18	···	87.5	6.24	···	109.7	6.23	···
Sc II	6245.64	1.51	-1.030	35.5	3.08	···	37.4	3.09	···	33.0	3.14	···
Sc II	6320.85	1.50	-1.819	8.2	3.06	···	8.5	3.03	···	7.2	3.07	···
Sc II	6604.60	1.36	-1.309	38.1	3.24	···	36.1	3.17	···	35.1	3.29	···
Ti I	5022.87	0.83	-0.434	67.9	4.71	···	70.3	4.80	···	93.4	4.82	···
Ti I	5024.84	0.82	-0.602	67.5	4.86	···	69.6	4.94	···	88.1	4.87	···
Ti I	5039.96	0.02	-1.130	73.1	4.69	···	74.3	4.77	···	97.3	4.73	···
Ti I	5064.65	0.05	-0.991	88.5	4.89	···	89.5	4.97	···	117.8	4.99	···
Ti I	5210.39	0.05	-0.884	93.4	4.86	···	91.1	4.87	···	138.1	5.13	···
Ti I	5739.47	2.25	-0.600	6.8	4.74	···	8.0	4.83	···	19.6	4.90	···
Ti I	5866.45	1.07	-0.840	53.3	5.01	···	52.6	5.03	···	85.6	5.19	···

Table B.1 (cont'd)

	λ	χ					HD 20782			HD 20781		
Element	(Å)	(eV)	log gf	EW$_{\odot}$	log $N_{\odot}$	log $N_{\odot,\mathrm{synth}}$[a]	EW	log N	log N_{synth}	EW	log N	log N_{synth}
Ti I	6091.17	2.27	-0.423	15.0	4.95	···	15.7	4.99	···	30.8	4.99	···
Ti I	6098.66	3.06	-0.010	4.8	4.76	···	5.3	4.82	···	12.1	4.89	···
Ti I	6258.10	1.44	-0.355	51.0	4.83	···	53.6	4.91	···	80.4	4.96	···
Ti I	6261.10	1.43	-0.479	54.9	5.01	···	50.2	4.96	···	82.9	5.12	···
Ti II	5154.07	1.57	-1.750	75.2	5.07	···	81.0	5.18	···	73.0	5.21	···
Ti II	5336.79	1.58	-1.590	66.1	4.73	···	71.1	4.81	···	62.7	4.84	···
Ti II	5381.02	1.57	-1.920	61.5	4.95	···	63.5	4.97	···	58.3	5.05	···
V I	6081.44	1.05	-0.579	14.7	3.89	···	14.3	3.89	···	36.7	3.96	···
V I	6090.21[c]	1.08	-0.062	32.0	3.84	3.78	31.1	3.84	3.76	59.0	3.90	3.86
V I	6111.65[c]	1.04	-0.715	11.5	3.89	3.80	10.2	3.85	3.80	33.6	4.02	3.92
V I	6224.53	0.29	-2.010	5.6	4.09	···	5.3	4.08	···	22.2	4.22	···
Cr I	5702.31	3.45	-0.667	24.5	5.81	···	20.8	5.73	···	38.0	5.83	···
Cr I	5783.06	3.32	-0.500	38.2	5.81	···	33.2	5.73	···	51.5	5.78	···
Cr I	5783.85	3.32	-0.295	49.2	5.80	···	45.1	5.74	···	68.6	5.87	···
Cr I	5787.92	3.32	-0.083	54.3	5.67	···	49.8	5.61	···	71.2	5.70	···
Cr I	6330.09	0.94	-2.920	28.2	5.66	···	25.4	5.62	···	49.7	5.61	···
Cr I	7400.25	2.90	-0.111	69.3	5.46	···	67.9	5.46	···	97.6	5.62	···
Mn I	5399.50	3.85	-0.287	31.8	5.41	···	33.7	5.46	···	48.5	5.50	···
Mn I	5432.55[c]	0.00	-3.795	47.9	5.42	5.27	43.5	5.37	5.21	112.9	6.23	5.26
Fe I	5322.04	2.28	-2.800	59.0	7.23	···	55.6	7.19	···	72.3	7.24	···
Fe I	5379.57	3.69	-1.510	64.0	7.40	···	60.7	7.36	···	73.9	7.40	···
Fe I	5522.45	4.21	-1.550	43.2	7.55	···	41.3	7.53	···	53.3	7.56	···
Fe I	5543.94	4.22	-1.140	63.7	7.50	···	61.7	7.49	···	74.7	7.53	···

Table B.1 (cont'd)

	λ	χ					HD 20782			HD 20781		
Element	(Å)	(eV)	log gf	EW$_\odot$	log $N_\odot$	log $N_{\odot,\rm synth}$[a]	EW	log N	log $N_{\rm synth}$	EW	log N	log $N_{\rm synth}$
Fe I	5546.50	4.37	-1.310	53.4	7.63	···	50.6	7.60	···	64.1	7.66	···
Fe I	5546.99	4.22	-1.910	29.7	7.65	···	26.1	7.58	···	45.3	7.78	···
Fe I	5560.21	4.43	-1.190	51.3	7.53	···	52.4	7.57	···	63.7	7.60	···
Fe I	5577.03	5.03	-1.550	11.6	7.53	···	10.1	7.47	···	17.1	7.59	···
Fe I	5579.34	4.23	-2.400	10.0	7.55	···	10.6	7.59	···	16.5	7.62	···
Fe I	5587.57	4.14	-1.850	40.6	7.72	···	40.8	7.74	···	49.3	7.71	···
Fe I	5651.47	4.47	-2.000	20.9	7.76	···	17.5	7.67	···	29.1	7.79	···
Fe I	5652.32	4.26	-1.950	28.8	7.70	···	25.3	7.63	···	38.2	7.72	···
Fe I	5661.35	4.28	-1.740	24.1	7.40	···	22.7	7.38	···	34.7	7.46	···
Fe I	5667.52	4.18	-1.580	56.3	7.77	···	53.6	7.74	···	69.2	7.84	···
Fe I	5677.68	4.10	-2.700	6.9	7.55	···	7.5	7.59	···	12.9	7.65	···
Fe I	5679.02	4.65	-0.920	63.6	7.66	···	63.3	7.67	···	74.9	7.69	···
Fe I	5680.24	4.19	-2.580	12.5	7.80	···	10.5	7.72	···	18.4	7.81	···
Fe I	5732.27	4.99	-1.560	17.1	7.70	···	15.1	7.64	···	21.7	7.69	···
Fe I	5741.85	4.26	-1.850	33.0	7.69	···	31.6	7.67	···	45.0	7.75	···
Fe I	5752.03	4.55	-1.180	57.6	7.73	···	55.2	7.70	···	66.7	7.74	···
Fe I	5775.08	4.22	-1.300	61.8	7.62	···	64.0	7.68	···	78.2	7.74	···
Fe I	5778.45	2.59	-3.480	24.7	7.51	···	24.5	7.52	···	40.4	7.56	···
Fe I	6079.00	4.65	-1.120	43.0	7.50	···	40.9	7.48	···	55.6	7.58	···
Fe I	6085.26	2.76	-3.100	41.3	7.62	···	39.0	7.60	···	62.8	7.78	···
Fe I	6098.24	4.56	-1.880	16.0	7.56	···	16.9	7.60	···	21.7	7.57	···
Fe I	6151.62	2.18	-3.300	50.8	7.42	···	50.6	7.44	···	68.3	7.46	···
Fe I	6159.37	4.61	-1.970	12.7	7.58	···	11.7	7.55	···	18.8	7.63	···

Table B.1 (cont'd)

	λ	χ					HD 20782			HD 20781		
Element	(Å)	(eV)	log gf	EW$_\odot$	log $N_\odot$	log $N_{\odot,\mathrm{synth}}$[a]	EW	log N	log N_synth	EW	log N	log N_synth
Fe I	6165.36	4.14	-1.470	47.3	7.44	···	46.2	7.44	···	57.6	7.46	···
Fe I	6187.99	3.94	-1.720	53.3	7.61	···	50.1	7.57	···	66.2	7.67	···
Fe I	6220.78	3.88	-2.460	19.5	7.60	···	17.3	7.54	···	29.4	7.64	···
Fe I	6226.73	3.88	-2.220	29.6	7.60	···	27.0	7.55	···	40.3	7.62	···
Fe I	6229.23	2.85	-2.810	38.9	7.37	···	37.2	7.35	···	54.7	7.41	···
Fe I	6240.65	2.22	-3.230	49.2	7.35	···	44.6	7.29	···	66.1	7.38	···
Fe I	6380.74	4.19	-1.380	55.2	7.53	···	53.3	7.51	···	64.4	7.53	···
Fe I	6392.54	2.28	-4.030	21.6	7.64	···	19.0	7.58	···	35.6	7.64	···
Fe I	6608.02	2.28	-4.030	18.1	7.53	···	18.6	7.56	···	34.5	7.60	···
Fe I	6609.11	2.56	-2.690	66.2	7.42	···	65.2	7.44	···	85.0	7.53	···
Fe I	6627.54	4.55	-1.680	30.7	7.71	···	28.8	7.68	···	39.0	7.72	···
Fe I	6653.85	4.15	-2.520	12.8	7.68	···	11.9	7.65	···	19.6	7.71	···
Fe I	6703.57	2.76	-3.160	36.3	7.55	···	34.6	7.54	···	51.6	7.58	···
Fe I	6710.32	1.49	-4.880	16.1	7.53	···	15.4	7.52	···	31.6	7.53	···
Fe I	6713.74	4.80	-1.600	19.9	7.61	···	20.9	7.64	···	27.6	7.65	···
Fe I	6716.22	4.58	-1.920	16.0	7.60	···	16.3	7.62	···	24.3	7.67	···
Fe I	6725.35	4.10	-2.300	17.6	7.57	···	17.0	7.56	···	26.3	7.61	···
Fe I	6726.67	4.61	-1.130	46.6	7.51	···	44.2	7.48	···	56.8	7.55	···
Fe I	6733.15	4.64	-1.580	27.4	7.61	···	25.7	7.59	···	35.2	7.63	···
Fe I	6739.52	1.56	-4.790	12.1	7.36	···	10.9	7.32	···	26.2	7.39	···
Fe I	6745.09	4.58	-2.160	8.4	7.52	···	8.3	7.52	···	13.6	7.59	···
Fe I	6745.96	4.08	-2.770	6.8	7.55	···	7.3	7.59	···	11.9	7.62	···
Fe I	6752.72	4.64	-1.300	38.6	7.56	···	36.1	7.53	···	47.6	7.59	···

Table B.1 (cont'd)

	λ	χ					HD 20782			HD 20781		
Element	(Å)	(eV)	log gf	EW$_{\odot}$	log $N_{\odot}$	log $N_{\odot,\mathrm{synth}}$[a]	EW	log N	log N_{synth}	EW	log N	log N_{synth}
Fe II	5197.58	3.23	-2.348	77.7	7.33	···	80.6	7.38	···	65.2	7.45	···
Fe II	5234.62	3.22	-2.279	90.4	7.51	···	91.6	7.53	···	71.6	7.51	···
Fe II	5414.07	3.22	-3.645	28.6	7.56	···	29.4	7.55	···	18.2	7.54	···
Fe II	6084.11	3.20	-3.881	20.1	7.54	···	21.0	7.53	···	13.1	7.56	···
Fe II	6113.32	3.22	-4.230	14.4	7.71	···	13.7	7.65	···	9.2	7.73	···
Fe II	6149.26	3.89	-2.841	37.4	7.57	···	38.5	7.57	···	24.1	7.59	···
Fe II	6247.56	3.89	-2.435	56.0	7.56	···	55.3	7.52	···	38.4	7.58	···
Fe II	7449.34	3.89	-3.488	22.0	7.80	···	19.6	7.70	···	15.2	7.91	···
Fe II	7711.72	3.90	-2.683	52.2	7.67	···	54.0	7.68	···	36.8	7.76	···
Co I	5301.04[c]	1.71	-2.000	20.4	4.97	4.88	19.0	4.94	4.86	33.9	4.98	4.95
Co I	5647.23	2.28	-1.560	15.4	4.92	···	14.1	4.88	···	26.2	4.95	···
Co I	6093.14	1.74	-2.440	9.5	5.00	···	8.5	4.95	···	18.3	5.01	···
Co I	6632.43	2.28	-2.000	10.4	5.10	···	8.5	5.01	···	17.5	5.10	···
Co I	6814.94[c]	1.96	-1.900	19.8	5.00	4.93	15.7	4.89	4.88	32.8	5.02	4.97
Ni I	5748.35	1.68	-3.260	30.3	6.24	···	28.5	6.21	···	42.1	6.24	···
Ni I	5754.65	1.94	-2.330	82.4	6.55	···	78.5	6.52	···	93.1	6.60	···
Ni I	5760.83	4.11	-0.800	38.4	6.30	···	35.1	6.25	···	39.4	6.24	···
Ni I	5805.21	4.17	-0.640	40.7	6.25	···	37.3	6.19	···	42.2	6.20	···
Ni I	5846.99	1.68	-3.210	22.5	6.01	···	22.4	6.01	···	36.0	6.06	···
Ni I	6108.11	1.68	-2.450	63.3	6.02	···	60.5	6.00	···	75.4	6.08	···
Ni I	6111.07	4.09	-0.870	33.2	6.24	···	29.9	6.18	···	36.0	6.22	···
Ni I	6128.96	1.68	-3.330	26.2	6.19	···	24.0	6.15	···	36.0	6.16	···
Ni I	6130.13	4.27	-0.960	20.9	6.22	···	20.6	6.21	···	24.4	6.22	···

Table B.1 (cont'd)

							HD 20782			HD 20781		
Element	λ (Å)	χ (eV)	log gf	$\mathrm{EW}_{\odot}$	$\log N_{\odot}$	$\log N_{\odot,\mathrm{synth}}$[a]	EW	$\log N$	$\log N_{\mathrm{synth}}$	EW	$\log N$	$\log N_{\mathrm{synth}}$
Ni I	6133.96	4.09	-1.830	5.4	6.24	···	5.7	6.27	···	6.8	6.24	···
Ni I	6175.36	4.09	-0.559	51.4	6.27	···	50.2	6.26	···	55.9	6.29	···
Ni I	6176.81	4.09	-0.260	66.3	6.22	···	65.5	6.23	···	73.4	6.28	···
Ni I	6177.24	1.83	-3.500	16.3	6.25	···	15.6	6.23	···	26.1	6.27	···
Ni I	6186.71	4.11	-0.960	32.3	6.33	···	31.9	6.33	···	37.5	6.35	···
Ni I	6204.60	4.09	-1.100	20.8	6.18	···	19.0	6.14	···	23.8	6.17	···
Ni I	6223.98	4.11	-0.910	27.1	6.17	···	24.5	6.11	···	30.3	6.15	···
Ni I	6230.09	4.11	-1.260	21.8	6.39	···	20.5	6.36	···	28.4	6.46	···
Ni I	6327.59	1.68	-3.150	36.5	6.22	···	35.6	6.21	···	51.8	6.29	···
Ni I	6370.34	3.54	-1.940	13.8	6.27	···	14.6	6.31	···	19.0	6.31	···
Ni I	6378.25	4.15	-0.830	32.1	6.23	···	31.0	6.21	···	35.9	6.23	···
Ni I	6598.59	4.24	-0.980	27.4	6.35	···	24.2	6.28	···	27.0	6.26	···
Ni I	6635.12	4.42	-0.820	27.6	6.37	···	24.8	6.31	···	28.1	6.31	···
Ni I	6643.63	1.68	-2.300	98.0	6.45	···	95.2	6.44	···	117.7	6.58	···
Ni I	6767.77	1.83	-2.170	80.6	6.15	···	81.1	6.19	···	94.0	6.23	···
Ni I	6842.03	3.66	-1.480	28.0	6.30	···	25.3	6.24	···	30.8	6.25	···

[a] Indicates the $\log N$ abundance determined from the synthetic fit to a given line. Each synthetic fit was performed with the MOOG *synth* driver. Synthetic fits were only performed for the C_2 features and the subset of V, Mn, and Co lines that were tested for hfs.

[b] The $\log N$ abundance for this line was rejected as spurious, as described in paragraph 4 of Section 3.3.

[c] Indicates that the spectral line was tested for hfs.

Appendix C

TABLE IV.2: COMPLETE AND UNABRIDGED

Table C.1. HD 80606/07: Lines Measured, Equivalent Widths, and Abundances

	λ	χ					HD 80606			HD 80607		
Element	(Å)	(eV)	log gf	$\mathrm{EW}_{\odot}$	$\log N_{\odot}$	$\log N_{\odot,\mathrm{synth}}$[a]	EW	$\log N$	$\log N_{\mathrm{synth}}$	EW	$\log N$	$\log N_{\mathrm{synth}}$
Na I	5682.63	2.10	-0.700	100.9	6.30	···	142.9	6.70	···	146.0	6.70	···
Na I	6154.23	2.10	-1.560	38.4	6.31	···	76.5	6.77	···	80.4	6.80	···
Na I	6160.75	2.10	-1.260	56.1	6.28	···	100.6	6.78	···	102.1	6.77	···
Mg I	4730.03	4.35	-2.523	67.3	7.83	···	103.0	8.23	···	110.2	8.30	···
Al I	6696.02	3.14	-1.347	38.3	6.27	···	70.4	6.66	···	70.8	6.65	···
Al I	6698.67	3.14	-1.647	22.9	6.27	···	47.9	6.65	···	47.9	6.62	···
Si I	5701.10	4.93	-1.581	37.2	7.08	···	59.8	7.46	···	57.6	7.44	···
Si I	5772.15	5.08	-1.358	51.8	7.23	···	72.6	7.56	···	71.8	7.56	···
Si I	6125.02	5.61	-1.464	30.3	7.44	···	52.2	7.83	···	50.5	7.81	···
Si I	6142.48	5.62	-1.295	32.4	7.31	···	52.8	7.67	···	53.2	7.69	···
Si I	6145.02	5.62	-1.310	37.2	7.41	···	58.4	7.76	···	56.0	7.74	···
Si I	6243.81	5.62	-1.242	47.0	7.50	···	67.9	7.83	···	68.2	7.84	···
Si I	6244.47	5.62	-1.093	47.3	7.35	···	67.5	7.67	···	67.7	7.68	···
Si I	6414.98	5.87	-1.035	51.5	7.55	···	71.2	7.83	···	70.3	7.82	···
Si I	6741.63	5.98	-1.428	15.2	7.35	···	29.1	7.72	···	29.0	7.72	···
Si I	6848.58	5.86	-1.524	17.5	7.41	···	32.7	7.78	···	30.6	7.76	···
Si I	7405.77	5.61	-0.313	97.9	7.19	···	115.8	7.44	···	···	···	···
Ca I	6161.30	2.52	-1.266	63.5	6.30	···	90.5	6.62	···	92.7	6.64	···
Ca I	6166.44	2.52	-1.142	67.2	6.24	···	93.6	6.54	···	96.0	6.56	···
Ca I	6169.04	2.52	-0.797	89.4	6.23	···	118.7	6.55	···	123.3	6.58	···
Ca I	6169.56	2.53	-0.478	107.7	6.18	···	138.9	6.47	···	145.4	6.51	···
Ca I	6455.60	2.52	-1.340	60.6	6.32	···	81.6	6.54	···	84.3	6.56	···
Ca I	6499.65	2.52	-0.818	86.5	6.19	···	108.8	6.41	···	112.5	6.44	···

Table C.1 (cont'd)

	λ	χ					HD 80606			HD 80607		
Element	(Å)	(eV)	log gf	$EW_\odot$	$\log N_\odot$	$\log N_{\odot,\mathrm{synth}}$[a]	EW	$\log N$	$\log N_{\mathrm{synth}}$	EW	$\log N$	$\log N_{\mathrm{synth}}$
Sc II	6245.64	1.51	-1.030	34.7	3.07	···	48.9	3.44	···	49.4	3.49	···
Sc II	6604.60	1.36	-1.309	38.5	3.25	···	51.3	3.59	···	50.1	3.60	···
Ti I	5022.87	0.83	-0.434	69.5	4.74	···	94.2	5.04	···	101.2	5.17	···
Ti I	5024.84	0.82	-0.602	66.4	4.84	···	97.0	5.26	···	99.7	5.30	···
Ti I	5039.96	0.02	-1.130	69.8	4.63	···	99.2	5.00	···	105.6	5.12	···
Ti I	5866.45	1.07	-0.840	48.2	4.92	···	77.3	5.25	···	82.0	5.31	···
Ti I	6091.17	2.27	-0.423	15.5	4.97	···	33.0	5.27	···	36.2	5.29	···
Ti I	6098.66	3.06	-0.010	5.0	4.78	···	15.2	5.21	···	16.9	5.23	···
Ti I	6258.10	1.44	-0.355	49.2	4.80	···	77.7	5.12	···	80.8	5.15	···
Ti II	5336.79	1.58	-1.590	68.5	4.78	···	81.0	5.13	···	78.9	5.14	···
Ti II	5381.02	1.57	-1.920	56.4	4.86	···	73.4	5.29	···	73.8	5.35	···
V I	6081.44	1.05	-0.579	14.0	3.88	···	38.8	4.29	···	43.2	4.32	···
V I	6090.21[c]	1.08	-0.062	32.9	3.86	3.83	66.3	4.27	4.22	69.1	4.29	4.22
V I	6111.65[c]	1.04	-0.715	10.7	3.86	3.81	37.5	4.39	4.26	41.3	4.41	4.29
V I	6251.83	0.29	-1.340	17.9	3.98	···	46.4	4.37	···	53.5	4.44	···
Cr I	5702.31	3.45	-0.667	23.1	5.78	···	49.1	6.19	···	53.4	6.25	···
Cr I	5783.06	3.32	-0.500	35.9	5.76	···	55.2	6.01	···	···	···	···
Cr I	5783.85	3.32	-0.295	43.0	5.69	···	72.0	6.08	···	73.3	6.09	···
Cr I	5787.92	3.32	-0.083	44.8	5.51	···	69.8	5.83	···	70.5	5.83	···
Cr I	7400.25	2.90	-0.111	77.1	5.58	···	107.6	5.93	···	109.2	5.93	···
Mn I	5432.55[c]	0.00	-3.795	46.1	5.38	5.27	43.5	5.37	5.21	111.1	6.25	5.66
Fe I	5322.04	2.28	-2.800	57.6	7.20	···	80.6	7.52	···	81.0	7.54	···
Fe I	5379.57	3.69	-1.510	58.4	7.30	···	84.6	7.69	···	81.6	7.64	···

Table C.1 (cont'd)

	λ	χ					HD 80606			HD 80607		
Element	(Å)	(eV)	log gf	$\mathrm{EW}_\odot$	$\log N_\odot$	$\log N_{\odot,\mathrm{synth}}$[a]	EW	$\log N$	$\log N_{\mathrm{synth}}$	EW	$\log N$	$\log N_{\mathrm{synth}}$
Fe I	5522.45	4.21	-1.550	42.7	7.54	···	61.7	7.81	···	64.4	7.86	···
Fe I	5543.94	4.22	-1.140	59.5	7.43	···	82.9	7.77	···	85.4	7.81	···
Fe I	5546.50	4.37	-1.310	49.7	7.57	···	71.4	7.88	···	73.0	7.91	···
Fe I	5546.99	4.22	-1.910	27.9	7.61	···	55.7	8.07	···	57.7	8.10	···
Fe I	5560.21	4.43	-1.190	49.6	7.50	···	69.3	7.79	···	69.3	7.78	···
Fe I	5577.03	5.03	-1.550	12.0	7.55	···	23.3	7.85	···	23.8	7.85	···
Fe I	5579.34	4.23	-2.400	11.1	7.61	···	24.5	7.96	···	24.1	7.94	···
Fe I	5587.57	4.14	-1.850	37.6	7.67	···	59.5	8.00	···	59.5	7.99	···
Fe I	5651.47	4.47	-2.000	18.5	7.70	···	34.9	8.02	···	35.5	8.02	···
Fe I	5652.32	4.26	-1.950	25.8	7.64	···	45.0	7.96	···	46.0	7.97	···
Fe I	5661.35	4.28	-1.740	21.6	7.34	···	41.5	7.70	···	42.4	7.71	···
Fe I	5667.52	4.18	-1.580	49.2	7.65	···	78.6	8.09	···	79.1	8.10	···
Fe I	5677.68	4.10	-2.700	6.5	7.52	···	15.8	7.89	···	16.6	7.90	···
Fe I	5679.02	4.65	-0.920	57.7	7.56	···	77.6	7.83	···	78.8	7.85	···
Fe I	5680.24	4.19	-2.580	9.8	7.68	···	22.7	8.05	···	24.0	8.07	···
Fe I	5732.27	4.99	-1.560	13.8	7.59	···	29.3	7.96	···	29.8	7.96	···
Fe I	5741.85	4.26	-1.850	31.0	7.65	···	51.8	7.97	···	52.9	7.98	···
Fe I	5752.03	4.55	-1.180	54.1	7.67	···	73.6	7.94	···	73.3	7.94	···
Fe I	5775.08	4.22	-1.300	55.8	7.52	···	79.4	7.86	···	79.6	7.86	···
Fe I	5778.45	2.59	-3.480	21.7	7.44	···	43.9	7.79	···	44.5	7.78	···
Fe I	6079.00	4.65	-1.120	43.8	7.52	···	64.3	7.81	···	66.7	7.85	···
Fe I	6085.26	2.76	-3.100	42.2	7.64	···	71.3	8.05	···	75.3	8.13	···
Fe I	6098.24	4.56	-1.880	16.4	7.58	···	36.0	7.99	···	33.2	7.92	···

Table C.1 (cont'd)

							HD 80606			HD 80607		
Element	λ (Å)	χ (eV)	log gf	EW$_\odot$	log $N_\odot$	log $N_{\odot,\mathrm{synth}}$[a]	EW	log N	log N_{synth}	EW	log N	log N_{synth}
Fe I	6151.62	2.18	-3.300	48.1	7.37	···	70.6	7.64	···	72.5	7.67	···
Fe I	6159.37	4.61	-1.970	12.3	7.57	···	27.3	7.95	···	29.2	7.98	···
Fe I	6165.36	4.14	-1.470	43.6	7.38	···	65.5	7.69	···	65.4	7.69	···
Fe I	6187.99	3.94	-1.720	46.2	7.48	···	71.6	7.85	···	73.3	7.88	···
Fe I	6220.78	3.88	-2.460	18.6	7.57	···	37.3	7.92	···	39.8	7.96	···
Fe I	6226.73	3.88	-2.220	28.3	7.57	···	54.7	8.00	···	51.2	7.93	···
Fe I	6229.23	2.85	-2.810	37.7	7.35	···	64.1	7.72	···	62.4	7.68	···
Fe I	6240.65	2.22	-3.230	47.7	7.32	···	75.8	7.69	···	75.2	7.68	···
Fe I	6380.74	4.19	-1.380	52.2	7.48	···	77.1	7.83	···	72.6	7.76	···
Fe I	6608.02	2.28	-4.030	17.1	7.50	···	37.4	7.85	···	39.2	7.86	···
Fe I	6609.11	2.56	-2.690	65.1	7.40	···	90.9	7.74	···	92.1	7.76	···
Fe I	6627.54	4.55	-1.680	29.4	7.68	···	52.3	8.05	···	50.3	8.01	···
Fe I	6653.85	4.15	-2.520	10.9	7.60	···	21.3	7.88	···	24.1	7.93	···
Fe I	6703.57	2.76	-3.160	36.2	7.55	···	62.4	7.90	···	60.1	7.85	···
Fe I	6710.32	1.49	-4.880	18.8	7.61	···	42.1	7.96	···	40.6	7.90	···
Fe I	6713.74	4.80	-1.600	20.2	7.61	···	40.5	8.00	···	39.2	7.97	···
Fe I	6716.22	4.58	-1.920	15.5	7.58	···	31.4	7.93	···	30.9	7.91	···
Fe I	6725.35	4.10	-2.300	17.4	7.56	···	34.7	7.90	···	36.5	7.92	···
Fe I	6726.67	4.61	-1.130	45.8	7.49	···	71.0	7.86	···	69.3	7.83	···
Fe I	6733.15	4.64	-1.580	26.4	7.59	···	49.4	7.98	···	48.4	7.95	···
Fe I	6739.52	1.56	-4.790	11.8	7.35	···	27.8	7.67	···	30.3	7.69	···
Fe I	6745.09	4.58	-2.160	8.6	7.53	···	19.0	7.87	···	19.2	7.86	···
Fe I	6745.96	4.08	-2.770	7.6	7.60	···	16.1	7.90	···	17.4	7.93	···

Table C.1 (cont'd)

	λ	χ					HD 80606			HD 80607		
Element	(Å)	(eV)	log gf	EW$_\odot$	log $N_\odot$	log $N_{\odot,\mathrm{synth}}$[a]	EW	log N	log N_{synth}	EW	log N	log N_{synth}
Fe I	6752.72	4.64	-1.300	34.6	7.49	···	59.1	7.86	···	58.3	7.85	···
Fe II	5197.58	3.23	-2.348	77.1	7.32	···	86.7	7.69	···	80.0	7.63	···
Fe II	5234.62	3.22	-2.279	77.8	7.26	···	88.5	7.64	···	86.9	7.69	···
Fe II	5414.07	3.22	-3.645	28.6	7.56	···	32.4	7.80	···	31.7	7.84	···
Fe II	6084.11	3.20	-3.881	20.0	7.53	···	27.3	7.89	···	25.6	7.89	···
Fe II	6113.32	3.22	-4.230	12.5	7.64	···	16.8	7.94	···	17.6	8.01	···
Fe II	6149.26	3.89	-2.841	34.5	7.51	···	45.6	7.93	···	39.1	7.85	···
Fe II	6239.95	3.89	-3.573	13.3	7.63	···	19.3	8.00	···	17.8	8.00	···
Fe II	6247.56	3.89	-2.435	51.2	7.46	···	58.5	7.80	···	54.5	7.79	···
Co I	5301.04[c]	1.71	-2.000	19.9	4.96	···	5.9	4.25	5.40	50.4	5.47	5.40
Co I	5647.23	2.28	-1.560	14.9	4.90	···	35.7	5.32	···	37.8	5.35	···
Co I	6093.14	1.74	-2.440	8.5	4.94	···	26.7	5.43	···	···	···	···
Co I	6678.80	1.96	-2.680	6.3	5.22	···	17.7	5.63	···	20.5	5.68	···
Co I	6814.94[c]	1.96	-1.900	18.8	4.97	···	49.5	5.50	5.42	51.5	5.52	5.46
Ni I	5748.35	1.68	-3.260	27.7	6.18	···	54.4	6.61	···	55.7	6.63	···
Ni I	5754.65	1.94	-2.330	75.9	6.43	···	105.4	6.90	···	107.3	6.95	···
Ni I	5760.83	4.11	-0.800	34.1	6.30	···	55.6	6.59	···	54.5	6.58	···
Ni I	5846.99	1.68	-3.210	22.2	6.00	···	47.6	6.43	···	48.7	6.44	···
Ni I	6111.07	4.09	-0.870	34.0	6.26	···	60.2	6.72	···	59.6	6.71	···
Ni I	6128.96	1.68	-3.330	25.8	6.19	···	50.0	6.57	···	51.0	6.58	···
Ni I	6130.13	4.27	-0.960	21.4	6.23	···	40.0	6.61	···	40.3	6.62	···
Ni I	6133.96	4.09	-1.830	4.9	6.20	···	13.4	6.65	···	14.2	6.68	···
Ni I	6175.36	4.09	-0.559	47.6	6.20	···	68.6	6.55	···	70.2	6.59	···

Table C.1 (cont'd)

	λ	χ					HD 80606			HD 80607		
Element	(Å)	(eV)	log gf	EW$_\odot$	log $N_\odot$	log $N_{\odot,\mathrm{synth}}$[a]	EW	log N	log N_{synth}	EW	log N	log N_{synth}
Ni I	6176.81	4.09	-0.260	61.8	6.15	···	86.4	6.54	···	89.1	6.59	···
Ni I	6177.24	1.83	-3.500	15.4	6.22	···	33.9	6.60	···	36.0	6.63	···
Ni I	6186.71	4.11	-0.960	31.1	6.30	···	52.0	6.67	···	52.8	6.69	···
Ni I	6223.98	4.11	-0.910	28.4	6.20	···	51.4	6.61	···	50.2	6.60	···
Ni I	6230.09	4.11	-1.260	22.4	6.40	···	42.4	6.80	···	44.1	6.83	···
Ni I	6327.59	1.68	-3.150	40.0	6.28	···	65.4	6.65	···	70.1	6.74	···
Ni I	6370.34	3.54	-1.940	12.7	6.23	···	30.7	6.69	···	30.7	6.69	···
Ni I	6378.25	4.15	-0.830	34.5	6.28	···	55.0	6.63	···	57.2	6.68	···
Ni I	6643.63	1.68	-2.300	93.6	6.37	···	124.0	6.78	···	128.2	6.86	···
Ni I	6767.77	1.83	-2.170	76.5	6.08	···	104.8	6.48	···	106.4	6.53	···

[a] Indicates the log N abundance determined from the synthetic fit to a given line. Each synthetic fit was performed with the MOOG *synth* driver. Synthetic fits were only performed for the subset of V, Mn, and Co lines that were tested for hfs.

[c] Indicates that the spectral line was tested for hfs.

REFERENCES

Allende Prieto, C., Barklem, P. S., Lambert, D. L., & Cunha, K. 2004, A&A, 420, 183

Allende Prieto, C., & Lambert, D. L. 2000, AJ, 119, 2445

Anderson, D. R., Collier Cameron, A., Delrez, L., et al. 2014, MNRAS, 445, 1114

Asplund, M., Grevesse, N., Sauval, A. J., & Scott, P. 2009, ARA&A, 47, 481

Baraffe, I., & Chabrier, G. 2010, A&A, 521, A44+

Baranne, A., Queloz, D., Mayor, M., et al. 1996, A&AS, 119, 373

Batygin, K., Morbidelli, A., & Tsiganis, K. 2011, A&A, 533, A7

Bender, C. F., Mahadevan, S., Deshpande, R., et al. 2012, ApJ, 751, L31

Bernstein, R., Shectman, S. A., Gunnels, S. M., Mochnacki, S., & Athey, A. E. 2003, Proc. SPIE, 4841, 1694

Bertelli, G., Bressan, A., Chiosi, C., Fagotto, F., & Nasi, E. 1994, A&AS, 106, 275

Brucalassi, A., Pasquini, L., Saglia, R., et al. 2014, A&A, 561, LL9

Bouchy, F. e. 2006, in Tenth Anniversary of 51 Peg-b: Status of and prospects for hot Jupiter studies, ed. L. Arnold, F. Bouchy, & C. Moutou, 319–325

Castelli, F., & Kurucz, R. L. 2004, ArXiv Astrophysics e-prints

Crifo, F., Jasniewicz, G., Soubiran, C., et al. 2010, A&A, 524, A10

Cutri, R. M., Skrutskie, M. F., van Dyk, S., et al. 2003, VizieR Online Data Catalog, 2246, 0

De Lee, N., Ge, J., Crepp, J. R., et al. 2013, AJ, 145, 155

Delfosse, X., Forveille, T., Ségransan, D., et al. 2000, A&A, 364, 217

Demarque, P., Woo, J.-H., Kim, Y.-C., & Yi, S. K. 2004, ApJS, 155, 667

Desidera, S., Gratton, R. G., Scuderi, S., et al. 2004, A&A, 420, 683

Desidera, S., Gratton, R. G., Lucatello, S., & Claudi, R. U. 2006, A&A, 454, 581

Desidera, S., & Barbieri, M. 2007, A&A, 462, 345

Dodson-Robinson, S. E. 2012, ApJ, 752, 72

Duquennoy, A., & Mayor, M. 1991, A&A, 248, 485

Eastman, J., Gaudi, B. S., & Agol, E. 2013, PASP, 125, 83

Eisenstein, D. J., Weinberg, D. H., Agol, E., et al. 2011, AJ, 142, 72

Erskine, D. J. 2003, PASP, 115, 255

ESA 1997, The HIPPARCOS and TYCHO catalogues. Astrometric and photometric star catalogues derived from the ESA HIPPARCOS Space Astrometry Mission, ESA Special Publication, 1200

Femenía, B., Rebolo, R., Pérez-Prieto, J. A., et al. 2011, MNRAS, 413, 1524

Fischer, D. A., & Valenti, J. 2005, ApJ, 622, 1102

Fitzpatrick, M. J., & Sneden, C. 1987, in Bulletin of the American Astronomical Society, Vol. 19, Bulletin of the American Astronomical Society, 1129–+

Fleming, S. W., Ge, J., Mahadevan, S., et al. 2010, ApJ, 718, 1186

Fleming, S. W., Ge, J., Barnes, R., et al. 2012, AJ, 144, 72

Ford, E. B., & Rasio, F. A. 2008, ApJ, 686, 621

Ge, J. 2002, ApJ, 571, L165

Ge, J., & Eisenstein, D. 2009, in ArXiv Astrophysics e-prints, Vol. 2010, astro2010: The Astronomy and Astrophysics Decadal Survey, 86

Ge, J., Erskine, D. J., & Rushford, M. 2002, PASP, 114, 1016

Ge, J., van Eyken, J., Mahadevan, S., et al. 2006, ApJ, 648, 683

Ge, J., Mahadevan, S., Lee, B., et al. 2008, in Astronomical Society of the Pacific Conference Series, Vol. 398, Extreme Solar Systems, ed. D. Fischer, F. A. Rasio, S. E. Thorsett, & A. Wolszczan, 449

Ge, J., Lee, B., de Lee, N., et al. 2009, in Society of Photo-Optical Instrumentation Engineers (SPIE) Conference Series, Vol. 7440, Society of Photo-Optical Instrumentation Engineers (SPIE) Conference Series

Ghezzi, L., Cunha, K., Smith, V. V., et al. 2010, ApJ, 720, 1290

Girardi, L., Bertelli, G., Bressan, A., et al. 2002, A&A, 391, 195

Gonzalez, G. 1997, MNRAS, 285, 403

Gonzalez, G., Carlson, M. K., & Tobin, R. W. 2010, MNRAS, 407, 314

González Hernández, J. I., Bonifacio, P., Ludwig, H.-G., et al. 2008, A&A, 480, 233

González Hernández, J. I., Delgado-Mena, E., Sousa, S. G., et al. 2013, A&A, 552, A6

Gray, D. F. 1994, PASP, 106, 1248

Gray, R. O., Corbally, C. J., Garrison, R. F., et al. 2006, AJ, 132, 161

Gudehus, D. H. 2001, in Bulletin of the American Astronomical Society, Vol. 33, American Astronomical Society Meeting Abstracts #198, 850

Gunn, J. E., Siegmund, W. A., Mannery, E. J., et al. 2006, AJ, 131, 2332

Hauschildt, P. H., Allard, F., & Baron, E. 1999, ApJ, 512, 377

Henden, A. A., Levine, S. E., Terrell, D., Smith, T. C., & Welch, D. 2012, Journal of the American Association of Variable Star Observers (JAAVSO), 40, 430

Henry, T. J. 2004, in Astronomical Society of the Pacific Conference Series, Vol. 318, Spectroscopically and Spatially Resolving the Components of the Close Binary Stars, ed. R. W. Hilditch, H. Hensberge, & K. Pavlovski, 159–165

Henry, T. J., Franz, O. G., Wasserman, L. H., et al. 1999, ApJ, 512, 864

Høg, E., Fabricius, C., Makarov, V. V., et al. 2000, A&A, 355, L27

Holman, M., Touma, J., & Tremaine, S. 1997, Nature, 386, 254

Ida, S., & Lin, D. N. C. 2008, ApJ, 673, 487

Innanen, K. A., Zheng, J. Q., Mikkola, S., & Valtonen, M. J. 1997, AJ, 113, 1915

Israelian, G., et al. 2009, Nature, 462, 189

Jensen, E. L. N., Mathieu, R. D., & Fuller, G. A. 1996, ApJ, 458, 312

Jiang, P., Ge, J., Cargile, P., et al. 2013, AJ, 146, 65

Johnson, J. A., Ivans, I. I., & Stetson, P. B. 2006, ApJ, 640, 801

Jones, H. R. A., Butler, R. P., Tinney, C. G., et al. 2006, MNRAS, 369, 249

Kaib, N. A., Raymond, S. N., & Duncan, M. J. 2011, ApJ, 742, L24

Kaib, N. A., Raymond, S. N., & Duncan, M. 2013, Nature, 493, 381

King, J. R., Deliyannis, C. P., Hiltgen, D. D., Stephens, A., Cunha, K., & Boesgaard, A. M. 1997, AJ, 113, 1871

Kratter, K. M. 2011, Evolution of Compact Binaries, ASPC, 447, 47

Kupka, F., Piskunov, N., Ryabchikova, T. A., Stempels, H. C., & Weiss, W. W. 1999, A&AS, 138, 119

Kurucz, R. 1993, ATLAS9 Stellar Atmosphere Programs and 2 km/s grid. Kurucz CD-ROM No. 13. Cambridge, Mass.: Smithsonian Astrophysical Observatory, 1993., 13

Laws, C., & Gonzalez, G. 2001, ApJ, 553, 405

Lee, B. L., Ge, J., Fleming, S. W., et al. 2011, ApJ, 728, 32

Lissauer, J. J., & Stevenson, D. J. 2007, Protostars and Planets V, 591

Lodders, K. 2003, ApJ, 591, 1220

Lytle, D. M. 1993, in Astronomical Society of the Pacific Conference Series, Vol. 52, Astronomical Data Analysis Software and Systems II, ed. R. J. Hanisch, R. J. V. Brissenden, & J. Barnes, 18

Kharchenko, N. V. 2001, Kinematika i Fizika Nebesnykh Tel, 17, 409

Lubow, S. H., & Ida, S. 2011, Exoplanets, edited by S. Seager. Tucson, AZ: University of Arizona Press, 2011, 526 pp. ISBN 978-0-8165-2945-2., p.347-371, 347

Ma, B., Ge, J., Barnes, R., et al. 2013, AJ, 145, 20

Mack, C. E., III, Schuler, S. C., Stassun, K. G., & Norris, J. 2014, ApJ, 787, 98

Mamajek, E. 2011, Univ. Rochester internal memorandum. http://www.pas.rochester.edu/∼emamajek/EEM_dwarf_UBVIJHK_color_Teff.dat

Mandushev, G., Torres, G., Latham, D. W., et al. 2005, ApJ, 621, 1061

Marcy, G. W., & Butler, R. P. 2000, PASP, 112, 137

Matthews, K., & Soifer, B. T. 1994, Astronomy with Arrays, The Next Generation, 190, 239

Maxted, P. F. L., Anderson, D. R., Collier Cameron, A., et al. 2013, PASP, 125, 48

Mayer, L., Wadsley, J., Quinn, T., & Stadel, J. 2005, MNRAS, 363, 641

Mayor, M., Marmier, M., Lovis, C., et al. 2011, arXiv:1109.2497

Mayor, M., & Queloz, D. 1995, Nature, 378, 355

Mazeh, T., Krymolowski, Y., & Rosenfeld, G. 1997, ApJ, 477, L103+

McDonough, W. 2001, in The Composition of the Earth, in Earthquake Thermodynamics and Phase Transitions in the Earth's Interior (International Geophysics Series, Vol. 76), ed. R. Teisseyre & E. Majewski (San Diego, CA: Academic Press)

Meibom, S., Torres, G., Fressin, F., et al. 2013, Nature, 499, 55

Meléndez, J., Asplund, M., Gustafsson, B., & Yong, D. 2009, ApJ, 704, L66

Metcalfe, T. S., Chaplin, W. J., Appourchaux, T., et al. 2012, ApJ, 748, L10

Mugrauer, M., & Neuhäuser, R. 2009, A&A, 494, 373

Mugrauer, M., Ginski, C., & Seeliger, M. 2014, MNRAS, 439, 1063

Neveu-VanMalle, M., Queloz, D., Anderson, D. R., et al. 2014, A&A, 572, AA49

Nidever, D. L., Marcy, G. W., Butler, R. P., Fischer, D. A., & Vogt, S. S. 2002, ApJS, 141, 503

Oscoz, A., Rebolo, R., López, R., et al. 2008, in Society of Photo-Optical Instrumentation Engineers (SPIE) Conference Series, Vol. 7014, Society of Photo-Optical Instrumentation Engineers (SPIE) Conference Series

Pasquini, L., Biazzo, K., Bonifacio, P., Randich, S., & Bedin, L. R. 2008, A&A, 489, 677

Patience, J., et al. 2002, ApJ, 581, 654

Pepe, F., Mayor, M., Delabre, B., et al. 2000, in Society of Photo-Optical Instrumentation Engineers (SPIE) Conference Series, Vol. 4008, Society of Photo-Optical Instrumentation Engineers (SPIE) Conference Series, ed. M. Iye & A. F. Moorwood, 582–592

Piskunov, N. E., Kupka, F., Ryabchikova, T. A., Weiss, W. W., & Jeffery, C. S. 1995, A&AS, 112, 525

Pinsonneault, M. H., DePoy, D. L., & Coffee, M. 2001, ApJ, 556, L59

Pont, F., Hébrard, G., Irwin, J. M., et al. 2009, A&A, 502, 695

Prochaska, J. X., & McWilliam, A. 2000, ApJ, 537, L57

Queloz, D., Mayor, M., Weber, L., et al. 2000, A&A, 354, 99

Quinn, S. N., White, R. J., Latham, D. W., et al. 2012, ApJ, 756, LL33

Quinn, S. N., White, R. J., Latham, D. W., et al. 2014, ApJ, 787, 27

Raghavan, D., McAlister, H. A., Henry, T. J., et al. 2010, ApJS, 190, 1

Ramírez, I., Allende Prieto, C., & Lambert, D. L. 2007, A&A, 465, 271

Ramírez, I., Meléndez, J., & Asplund, M. 2009, A&A, 508, L17

Ramírez, I., Asplund, M., Baumann, P., Meléndez, J., & Bensby, T. 2010, A&A, 521, A33+

Ramírez, I., Meléndez, J., Cornejo, D., Roederer, I. U., & Fish, J. R. 2011, ApJ, 740, 76

Ramsey, L. W., Adams, M. T., Barnes, T. G., et al. 1998, in Society of Photo-Optical Instrumentation Engineers (SPIE) Conference Series, Vol. 3352, Society of Photo-Optical Instrumentation Engineers (SPIE) Conference Series, ed. L. M. Stepp, 34–42

Raymond, S. N., Armitage, P. J., & Gorelick, N. 2009, ApJ, 699, L88

Raymond, S. N., et al. 2011, A&A, 530, A62+

Reddy, B. E., Lambert, D. L., & Allende Prieto, C. 2006, MNRAS, 367, 1329

Sackmann, I.-J., Boothroyd, A. I., & Kraemer, K. E. 1993, ApJ, 418, 457

Santos, N. C., Israelian, G., & Mayor, M. 2004, A&A, 415, 1153

Schlegel, D. J., Finkbeiner, D. P., & Davis, M. 1998, ApJ, 500, 525

Schuler, S. C., Flateau, D., Cunha, K., King, J. R., Ghezzi, L., & Smith, V. V. 2011, ApJ, 732, 55

Schuler, S. C., Cunha, K., Smith, V. V., et al. 2011, ApJ, 737, L32

Shectman, S. A., & Johns, M. 2003, Proc. SPIE, 4837, 910

Shetrone, M., Cornell, M. E., Fowler, J. R., et al. 2007, PASP, 119, 556

Sneden, C. A. 1973, PhD thesis, THE UNIVERSITY OF TEXAS AT AUSTIN.

Sneden, C. 1973, ApJ, 184, 839

Soubiran, C., Le Campion, J.-F., Cayrel de Strobel, G., & Caillo, A. 2010, A&A, 515, A111

Sousa, S. G., Santos, N. C., Israelian, G., Mayor, M., & Monteiro, M. J. P. F. G. 2007, A&A, 469, 783

Sousa, S. G., Santos, N. C., Mayor, M., et al. 2008, A&A, 487, 373

Tabernero, H. M., Montes, D., & González Hernández, J. I. 2012, A&A, 547, A13

Takeda, G., & Rasio, F. A. 2005, ApJ, 627, 1001

Torres, G., Andersen, J., & Giménez, A. 2010, A&A Rev., 18, 67

Torres, G., Andersen, J., & Giménez, A. 2010, A&A Rev., 18, 67

Tull, R. G. 1998, in Society of Photo-Optical Instrumentation Engineers (SPIE) Conference Series, Vol. 3355, Society of Photo-Optical Instrumentation Engineers (SPIE) Conference Series, ed. S. D'Odorico, 387–398

van Eyken, J. C., Ge, J., & Mahadevan, S. 2010, ApJS, 189, 156

Veras, D., & Armitage , P. J. 2005, ApJ, 620, L111

Vogt, S. S., Allen, S. L., Bigelow, B. C., et al. 1994, Proc. SPIE, 2198, 362

Wang, J., Ge, J., Jiang, P., & Zhao, B. 2011, ApJ, 738, 132

Wang, J., Ge, J., Wan, X., De Lee, N., & Lee, B. 2012a, PASP, 124, 1159

Wang, J., Ge, J., Wan, X., Lee, B., & De Lee, N. 2012b, PASP, 124, 598

Wang, S.-i., Hildebrand, R. H., Hobbs, L. M., et al. 2003, in Society of Photo-Optical Instrumentation Engineers (SPIE) Conference Series, Vol. 4841, Society of Photo-Optical Instrumentation Engineers (SPIE) Conference Series, ed. M. Iye & A. F. M. Moorwood, 1145–1156

Wisniewski, J. P., Ge, J., Crepp, J. R., et al. 2012, AJ, 143, 107

Wolszczan, A., & Frail, D. A. 1992, Nature, 355, 145

Wright, E. L., Eisenhardt, P. R. M., Mainzer, A. K., et al. 2010, AJ, 140, 1868

Wright, J. T., Roy, A., Mahadevan, S., et al. 2013, ApJ, 770, 119

Xia, F., & Fu, Y.-N. 2010, Chinese Astron. Astrophys., 34, 277

Xia, F., Ren, S., & Fu, Y. 2008, Ap&SS, 314, 51

Young, R. E. 2003, New A Rev., 47, 1

Zucker, S. 2003, MNRAS, 342, 1291

Zucker, S., & Mazeh, T. 1994, ApJ, 420, 806